January 2023

An Investigation Into Impacts Of Microphysics Parameterization Schemes On Radiation Fog Within A Large Eddy Simulation Framework, To Small Unmanned Aircraft System Operations

Joseph Lafayette Gufford

An Investigation into Impacts of Microphysics Parameterization Schemes on Radiation Fog within a Large Eddy Simulation Framework, to small Unmanned Aircraft System operations

by

joseph lafayette gufford IV

Bachelor of Science, florida State University, 2015

A Thesis

Submitted to the Graduate Faculty

of the

University of North Dakota

in partial fulfillment of the requirements

for the degree of

Master of Science

Grand Forks, North Dakota

May

2023

This thesis, submitted by Joseph Lafayette Gufford IV in partial fulfillment of the requirements for the Degree of Master of Science from the University of North Dakota, has been read by the Faculty Advisory Committee under whom the work has been done and is hereby approved.

_____
Mark Askelson

_____
David Delene

_____
Gretchen Mullendore

This thesis is being submitted by the appointed advisory committee as having met all of the requirements of the School of Graduate Studies at the University of North Dakota and is hereby approved.

_____
Chris Nelson
Dean of the School of Graduate Studies

_____
Date

PERMISSION

Title An Investigation into Impacts of Microphysics Parameterization Schemes on Radiation Fog within a Large Eddy Simulation Framework, to small Unmanned Aircraft System operations

Department Atmospheric Sciences

Degree Master of Science

In presenting this thesis in partial fulfillment of the requirements for a graduate degree from the University of North Dakota, I agree that the library of this University shall make it freely available for inspection. I further agree that permission for extensive copying for scholarly purposes may be granted by the professor who supervised my thesis work or, in his absence, by the Chairperson of the department or the dean of the School of Graduate Studies. It is understood that any copying or publication or other use of this thesis or part thereof for financial gain shall not be allowed without my written permission. It is also understood that due recognition shall be given to me and to the University of North Dakota in any scholarly use which may be made of any material in my thesis.

Joseph Lafayette Gufford IV
March 29, 2023

ACKNOWLEDGMENTS

I would like to express my gratitude and appreciation to many people. I am thankful for my committee members for the guidance and support they have provided me during the time I have spent in graduate school. I am grateful for my advisor, Dr. Mark Askelson, for the wonderful research opportunities he has provided me. I am thankful for Dr. Mullendore for answering my many questions on modeling. I would also like to express my appreciation to Dr. Delene, with whom I had many nice conversations on instrumentation and fog. I am also very thankful for my family, who provided me with emotional support. I would like to express my appreciation to my friends and fellow graduate students who I studied and worked with along the way. Special thanks to Bethany, who listened to me talk about fog for way too many hours.

ABSTRACT

Fog is a threat to the operations of small unmanned aerial systems (sUAS). Improved fog forecasting will allow for more timely dissemination of warnings, allowing operators to maximize operational time and to minimize flight cancellations. The impacts of grid spacing and microphysical parameterization were examined to study their influences on fog formation in the Weather Research and Forecasting numerical weather prediction model. An ensemble of forecasts was produced, wherein varying grid spacings (1 km and 0.333 m) were permuted with different microphysics schemes (single and double moment) for two different fog events. It was found that sub-kilometer grid spacing improved the simulated fog formation and dissipation times for one fog event, but did not for the other event. Microphysical schemes had a varying impact across model runs, where its influence was mainly felt in the dissipation time of the fog events. Future avenues for improving fog forecasts are discussed.

LIST OF FIGURES

LIST OF TABLES

Table of Contents

Chapter 1: Introduction

The use of small Unmanned Aircraft Systems (sUAS) within the United States' National Airspace System is a focus of regulatory agencies, namely the Federal Aviation Administration; the industry currently has a great desire to fly Beyond Visual Line of Sight (BVLOS) (Askelson et al. 2017). Fog, and fog forecasting, is a key issue that, if addressed, would aid expansion of sUAS operations. In the United States, operators can operate sUAS by complying with 14 CFR Part 107. Chief among these requirements is that the operator must keep the sUAS within visual line of sight (eCFR 2022). Fog, low clouds, and other low visibility conditions (such as blowing dust) are thus key hazards to sUAS operations. Fog is optically thick in the visual spectrum of light and produces low visibility conditions, which does not allow for the safe operation of sUAS. Fog also inhibits the use of electro-optical and infrared cameras, which are crucial tools for BVLOS operations (Duthon et al. 2019; Price and Stokkereit 2020). Due to the limitations of these instruments, accurate and timely fog forecasting, both in time and space, is crucial for flight planning and safety. More accurate fog forecasting, through the reduction of false alarms, will allow operators to extend the temporal and spatial ranges of their operations. Furthermore, reducing the number of missed events in fog forecasting will allow operators to reschedule their flights earlier, which offsets the operational costs of cancelling a flight closer to the time of a fog event.

One common solution to fog forecasting is numerical weather prediction. Fog is sensitive to many different aspects of numerical weather models, including, but not limited to: horizontal and vertical resolution, nesting, initial and boundary conditions, and the physical parameterizations selected (Steeneveld et al. 2015). Forecasters are beginning to model fog at sub-kilometer grid spacing; such models include the London Model, the Delhi Model and the AROME-Airport model.

Previous research in China showed the success of using WRF and WRF-LES, utilizing a sub-kilometer domain with a grid spacing of 333.33 m (Cui et al. 2019). The increased accuracy of high resolution fog forecasting has been attributed to better representation of the impact of land surface heterogeneities and a more realistic representation of turbulent mixing (Cui et al. 2019; Li and Pu 2022; Jayakumar et al. 2018).

This study focuses on comparison of using traditional boundary layer parameterizations versus the Large Eddy Simulation (LES) option in the Weather Research and Forecasting (WRF) model V4.2 (Skamarock et al. 2019a) for two fog events in the northern plains of the United States. In this study, the non-local YSU (Hong et al. 2006) and hybrid MYNN2.5 (Nakanishi and Niino 2006, 2009, Olson et al. 2019) schemes used at a horizontal grid spacing of 1 km (mesoscale simulations) are compared to forecasts produced using a nested WRF-LES run using the 1.5 TKE closure with a grid spacing of 333 m. The impact of the choice of the microphysical parameterization scheme is also be investigated for both the LES and mesoscale simulations. The schemes used include the single moment WSM6 scheme (Hong and Lim 2006) and the double moment scheme WDM6 (Lim and Hong 2010). This study expands upon previous research by examining the effects of the microphysical schemes upon the fog forecast at the 333 m grid spacing using the WRF model and enables further understanding of the impact of boundary layer parameterization on fog.

Simulation performance is evaluated by comparing modeled fog formation/dissipation times and surface meteorological variables to Automated Surface Observing Systems/Automated Weather Observing System (AWOS/ASOS) and mesonet observations in the areas of interest. Furthermore, dichotomous/categorical metrics, such as the False Alarm Ratio (FAR) and the Threat Score (TS) are used to evaluate model performance. Through this analysis, the advantages

or disadvantages of using each model configuration for sUAS flight planning purposes are demonstrated. Furthermore, impacts of fog upon sUAS operations and, specifically BVLOS Detect and Avoid (DAA) methods, will also be discussed.

Background

Turbulence and Radiative Effects on Fog

Numerous physical factors affect the formation, lifecycle, and dissipation of fog. Fog is sensitive to many physical factors, such as: longwave and shortwave radiation, sensible and latent heat fluxes from the land surface, turbulence, and the interactions between the aforementioned factors. Radiation fog forms during clear nights, which maximizes the radiative cooling of both the lowest levels of the atmosphere and the Earth surface. Fog is optically thick in the infrared region of the electromagnetic spectrum, absorbing infrared radiation (Price 2011). Radiative flux divergence and convergence is a key controller of temperature within the nocturnal boundary layer. (Stull 2009; Arya 2001) The formula for radiative flux divergence is (Hoch et al. 2007)

$$\frac{dT}{dt} = -\frac{1}{\rho c_p} * \frac{d(LW)}{dz} \quad (1)$$

If the net infrared radiation being emitted upward by the atmosphere increases with height, then a layer will cool. Fog forms best under clear skies when radiative cooling is at a maximum. As a fog layer thickens, the level of maximum cooling moves from the Earth surface to the top of the fog layer, as the fog layer absorbs the infrared radiation emitted from the surface. Cloud top cooling promotes negative buoyancy; this negative buoyancy causes cooler air parcels from the top of the fog layer to sink into the fog layer. If the air near the top of the fog layer is dry this will cause entrainment of the drier residual layer air into the fog and drive evaporation of the fog layer, thus competing against the radiative flux divergence (Yang and Gao 2020). A further complexity involved in this situation is that a drier free atmosphere provides less downwelling longwave

radiation as compared to a layer with higher water vapor content, which affects the rate of radiative flux divergence of the fog (Wærsted et al. 2019). As the fog entrains this air, the fog layer can grow and deepen, albeit with lower liquid water content; if the air is too dry, fog can dissipate at the surface, "lifting" from the ground (Yang and Gao 2020; Izett and van de Wiel 2020). The turbulent mixing from wind shear and sinking thermals acts to homogenize the air within the fog layer, and the temperature profile becomes approximately moist adiabatic (Yang et al. 2021; Bergot 2013; Mazoyer et al. 2017). Turbulence is commonly viewed as a threshold problem, with weak turbulence associated with shallow fog, and too strong turbulence causing fog dissipation (Ju et al. 2021; Zhou and Ferrier 2008).

The lifecycle of fog often includes the transition from a shallow layer into a deeper, well mixed layer. Shallow fog layers are characterized by a temperature inversion throughout the depth of the fog. In deeper fogs mixing causes the temperature gradient to be moist-adiabatic in character, with an inversion also being found near the top of the fog (Maronga and Bosveld 2017). The fog lifecycle is governed by the profiles of moisture, temperature, and wind speed in the "clear air": in the single column modeling study by Smith et al. (2018) it was determined that small perturbations in relative humidity and wind speed can have large impacts on dissipation time and formation of stable layers.

Microphysical Effects on Fog Lifecycle

The microphysical aspects of fog, such as the liquid water content, effective radius, and droplet number concentration, have important impacts upon the radiative properties of fog and the settling of fog droplets, and thus fog lifecycle. The effective radius of fog droplets largely determines the extinction of radiation within the fog layer, and this effective radius depends upon both the number concentration of droplets and the liquid water content. Not accounting for the

number concentration of hydrometeors can lead to large errors in the prediction of visibility—as much as 50% error (Gultepe et al. 2006). One of the most substantial influences on the dissipation of fog is solar radiation. Solar radiation is both absorbed within fog and by the ground; the ground then transfers this energy to the air through sensible heat fluxes and longwave radiation (Wærsted et al. 2017, 2019). This energy causes temperatures to rise, contributing to the evaporation of the fog layer. The loss of liquid water content occurs alongside any loss of water due to effects of entrainment of the air above the fog layer or due to droplet settling. The type of aerosols within the fog layer can have a further effect on fog dissipation by preferentially absorbing or scattering solar radiation (Maalick et al. 2016; Ding et al. 2019).

Microphysical schemes are used to parameterize and model cloud processes and properties, such as those for cloud droplets, ice crystals, condensation, evaporation, and rainfall. Two broad options are available for microphysical schemes: bin and bulk. Bin schemes divide each hydrometeor type size spectrum into multiple intervals and solve for the number of particles in each interval, with predictive equations for each bin (Warner 2010). Bulk schemes differ from bin schemes in that analytic functions are used to describe the size distribution of each hydrometeor category. In this study bulk microphysics schemes are used as the computational cost of bin schemes is too high for operational use. Bulk microphysics schemes can be further divided by the number of moments that they use. Single moment schemes predict only one prognostic variable, typically the mass mixing ratio of the hydrometer class. Classes are often divided into cloud droplets, raindrops, cloud ice, snow, graupel and hail, and water vapor. Bulk double moment schemes predict the total number concentration of hydrometers (i.e. all particle diameters) within a class in addition to the mass mixing ratio within a class. The number concentration of a particular particle diameter in a bulk scheme is predicted by the analytic function of the scheme (often a

gamma distribution), which is determined by the aforementioned prognostic variables. Double moment schemes are not necessarily "fully" double moment for every hydrometeor class. In this work three schemes were evaluated. The WRF Single-Moment 6-class scheme (WSM6) and the WRF Double-Moment 6-class scheme (WDM6) were the primary schemes utilized in this study. To evaluate differences between different double moment scheme predictions of cloud water number concentration, the Milbrandt-Yau double moment scheme was also included (Milbrandt and Yau 2005a,b). The WSM6 scheme predicts cloud liquid water mixing ratio (Qc) only, with an assumed constant value for cloud droplet number concentration (Nc) of 300 cm^{-3}. In contrast, the WDM6 and Milbrand-Yau schemes predict both the number concentration and mixing ratio for cloud water. The prediction of the number concentration and the mass mixing ratio is important for interaction with radiation. One additional factor of importance is the representation of saturation in a microphysics scheme. These three schemes all assume that supersaturation does not exist at the end of the model microphysics process/subroutine in the WRF model. Furthermore, if a grid cell is unsaturated, hydrometeor species will evaporate until saturation exists. In WDM6, the nucleation of cloud droplets/activation of CCN is done using Twomey's formula (GUO et al. 2019; Lim and Hong 2010). The Milbrandt-Yau scheme uses a four-parameter activation function based on Twomey's method to calculate nucleation, with dependencies on temperature, pressure, and vertical velocity (Cohard and Pinty 2000; Milbrandt and Yau 2005b). One important difference between WDM6 and MY schemes is that WDM6 treats cloud condensation nuclei (Nccn) as a prognostic variable.

Previous numerical modeling studies of fog have shown various degrees of sensitivity to the microphysics scheme. In a case study of radiation fog by Steeneveld et al. (2015) it was determined that single moment schemes (in this instance WSM3 and WSM6) produced lower

liquid water content values than the WDM6. In their study, the WDM6 outperformed the single moment schemes. In their study it was noted that the microphysics scheme impacted the fog dissipation time. There was no discernable impact of microphysics schemes upon the formation time. The impacts of various permutations of physics schemes were further studied by Lin et al. (2017) for an advection fog case. In their study, some schemes, including WDM6, produced too high of liquid water content at the lowest model level, contributing to fog that was too persistent in the model as compared to observations.

Droplet settling and the interception of fog droplets by the underlying surface is an additional factor for fog lifecycle that must be considered, as it acts as a sink of fog liquid water content. The WRF model contains two methods to calculate droplet settling onto the surface, activated via the grav_settling namelist option. The fogdes (grav_settling=2) option (Katata 2014) is used to parameterize fog droplet settling and includes parameterizations effects of droplet impaction on vegetation canopies. Higher in the atmosphere, the fogdes option uses gravitational settling of cloud droplets dependent upon Stokes Law. (Skamarock et al. 2019b; Duynkerke 1991) The Duynkerke option for gravitational settling (Skamarock et al. 2019a; Katata 2014) depends only upon gravitational settling via Stokes Law and has no dependence upon vegetation. In a study by Katata et al. (2011), it was determined that neglecting droplet settling produced unrealistically high amounts of LWC. This result has been reproduced in other studies; in a recent study (Kutty et al. 2021) for a radiation fog over India, the inclusion of the fogdes droplet settling scheme produced more realistic results. The benefits of using a droplet settling scheme have also been confirmed in a study of sea fog (Boutle et al. 2022; Taylor et al. 2021).

Representation of Fog in Numerical Weather Prediction Models

One of the focuses of this study is the impact of the method used to represent turbulence in the atmosphere, whether it be through a Large Eddy Simulation or through the use of traditional Reynolds Averaged Navier Stokes (RANS) boundary layer schemes. Boundary layer schemes parameterize atmospheric fluxes of momentum, moisture, and heat within the model. Traditional RANS boundary layer schemes used in mesoscale models can generally be classified into local closure and nonlocal closure methods. Local schemes parameterize turbulence through local gradients of variables (adjacent grid points in the model); non-local schemes parameterize turbulence through deeper layers of the atmosphere by considering the effects of large eddies, surface fluxes, and properties of the profile of the atmosphere (Warner 2010). The hybrid scheme (with local and non-local components) in this study, MYNN2.5, and nonlocal scheme, YSU, were selected for their common usage in the WRF model. The MYNN2.5 boundary layer scheme is a 1.5 order closure model that allows for the prognostic prediction of turbulence kinetic energy (TKE) in order to determine eddy viscosity. The MYNN2.5 scheme approximates local mixing. Estimation of the turbulent fluxes are done via gradients of local variables (adjacent grid points) and considers the mass-flux for non-local effects. The standard version of MYNN is used in this study with no modifications to the standard WRF namelist (Olson et al. 2019). The YSU scheme is a K-Profile Parameterization (KPP) scheme that is both first-order and non-local. It contains a counter gradient term to account for large eddies and explicit entrainment at the PBL top. In fog and cloud-topped boundary layer situations an alternative top-down mixing approach is used, along with an additional entrainment term associated with cloud top radiational/evaporative cooling (Hong et al. 2006; Hong 2010; Wilson and Fovell 2018). Each PBL scheme has advantages

and disadvantages; YSU has been found to generate PBLs that are too deep and MYNN generates PBLs that do not account for deep mixing (Cohen et al. 2015).

In the 333 m domain of this study, the Large Eddy Simulation (LES) framework is used. In Large Eddy Simulations, the largest size eddies containing the most amount of energy are explicitly modeled, and small-scale eddies are parameterized through subfilter scale (SFS) models. In the LES framework the full equations of motion are filtered with a low pass filter. The filter can either be in wavenumber space or physical space; the effect is to remove small scale (high wavenumber) turbulent eddies from the flow field. Filters in large eddy simulations use are done through convoluting a kernel function with the velocity field of the model. In Fourier space, filters can remove wavenumbers in the velocity field higher than a pre-defined threshold with wave-cutoff filters; in physical space an example is the top-hat filter, which depends on a chosen spatial width (Wyngaard 2010). In the WRF-LES model, "implicit" filtering is used, where the numerical grid and finite difference schemes of the model is assumed to have done the filtering and no explicit filter is utilized (Simon et al. 2019; Kirkil et al. 2012). Even if explicit filtering is not used, a subfilter scale model is still used to account for the effects of smaller scale eddies and turbulence. The horizontal grid spacing of 333 m is coarser than typical LES simulations, and is within the atmospheric "grey zone". The "grey zone" is a range of resolutions where turbulence becomes partly resolved by the model (Wyngaard 2004). At coarser resolutions (>= 1 km) turbulence is traditionally fully parameterized by one dimensional planetary boundary layer schemes; at higher resolutions (< 100 m) turbulence is more realistically represented by the LES method. The subfilter scale model for momentum chosen is the nonlinear backscatter and anisotropic model (NBA1) (Mirocha et al. 2010; Kirkil et al. 2012). It was chosen for its success in conducting coarse LES simulations in the literature (Cui et al. 2019; Heath et al. 2017; Zhang et al. 2019) The SFS model

for scalars is the 1.5 TKE (Lilly 1966). The 1.5 TKE model uses prognostic TKE and a scale-aware mixing length to calculate eddy viscosity and fluxes (Mirocha et al. 2014).

As mentioned earlier, several operational mesoscale models have been designed for visibility prediction with grid spacing at the sub-kilometer level. The London Model uses a 333 m grid spacing with a 3D Smagorinsky SGS turbulence parameterization. The London Model improved fog forecasting at long lead times, with the causal factor being better representation of orographic effects. The Delhi Model, which uses a similar configuration as the London Model but is designed for the city of Delhi, also showed success in forecasting fog. An improved version with chemistry and aerosol effects, DM-CHEM, was released in 2021 (Jayakumar et al. 2021).

The land surface model scheme used in the study is the Noah Land Surface scheme (sf_surface_physics = 2) (Tewari et al. 2004). The Noah-LSM controls the fluxes of sensible heat, latent heat, and radiation at the Earth's surface and predicts soil moisture and temperature. The Noah-LSM has 4 soil layers and represents snow with a single layer. Noah-LSM is capable of representing the effects of different land use types (e.g. urban, cropland, etc.). The Noah LSM is also capable of representing simplistic canopy effects of vegetative canopies. The scheme represents snow covered ground with a single layer and temperature.

Further Complexities in the Numerical Modeling of Fog

With numerical modeling of fog, the many differing physical processes that must be parameterized all have impacts upon its formation, growth, and dissipation. This situation is further complicated by the fact that errors and discrepancies in one physical scheme or model choice can hide errors within another, due to the nonlinear interactions involved within fog dynamics (Steeneveld and de Bode 2018). Despite this complication, Steeneveld and de Bode (2018) discovered that two of the strongest influences on the fog lifecycle were turbulent mixing and soil conductivity. Fog is also sensitive to domain size and the choice of nesting. In Steeneveld et. al

(2015), nested simulations produced worse results than non-nested domains, with insignificant differences between one-way and two-way nesting. They also reported that fog was sensitive to domain size, with larger domains producing fog with a more scattered appearance. Numerical models also show a dependence on vertical resolution; WRF-3D simulations of fog improved with increasing vertical resolution below 1 kilometer in a fog case study over India (Pithani et al. 2019). The dependencies of model performance on initial and boundary conditions are also demonstrated in that work. Low level moisture was better represented using ECMWF boundary conditions than boundary conditions from the Unified Model; using ECMWF boundary conditions resulted in a better fog forecast in their case study. ECMWF may not necessarily be the best choice for all initial and boundary conditions; however, this sensitivity demonstrates the influence of these factors on the ability of limited area models to simulate fog remains prominent. Different case studies of fog events have reported success with different combinations of boundary layer, microphysical, radiative, and land surface schemes. The best performing WRF setup for one event does not necessarily translate to other events, illustrating the complex interactions occurring in the lower troposphere required to form, sustain, and dissipate fog (Steeneveld et al. 2015; Pithani et al. 2019; Lin et al. 2017; Velde et al. 2010; Kutty et al. 2021). While not a concern in this study, complex terrain also impacts fog prediction.

While single column models are a great tool and can successfully model many properties of fog, they are not always appropriate. They do not represent the horizontal inhomogeneities in terrain or atmospheric variables, as they assume these properties are homogeneous (Velde et al. 2010). They do remain advantageous as they allow for a very high vertical resolution for a much cheaper computational cost than a full three-dimensional model. The limitations of the ability of one-dimensional models to properly account for horizontal inhomogeneities can be remedied by

coupling a one-dimensional model to a three-dimensional model. In addition to coupling the one-dimensional PAFOG model to the WRF model, Kim et al. (2020) prescribed the initial soil moisture state using observations; this setup showed improvement relative to a 2 km WRF simulation.

Among three dimensional models, differences in performance are apparent. In a comparison of WRF and the HARMONIE model, Steeneveld et al. (2015) reported that the HARMONIE model failed to properly represent fog formation in their case studies of two events. In a comparison of multiple fog events for WRF and HARMONIE (Román-Cascón et al. 2019), their 4th event had WRF failing to predict any fog, whereas HARMONIE predicted the incorrect fog mechanism (HARMONIE had predicted cloud base lowering fog instead of a radiation fog).

Chapter 2: Data and Methods

Simulations were completed using WRF ARW V4.2. To investigate the effects of model performance, two fog cases were examined. The first case, focused on the Red River Valley on the North Dakota/Minnesota border, occurred on 30 March 2020. The second case, occurring in the Minneapolis, MN, metropolitan area, occurred on 10 September 2020. Grand Forks was chosen for its importance to the Unmanned Aircraft Industry; it is home to the Northern Plains UAS Test Site and numerous other initiatives and operations involving UAS. Minnesota was chosen as it is host to an important airport in the region, KMSP. The specific fog events were chosen as they produced low visibility (below 0.25 miles/400 m) and light winds during the time of fog (below 5 m s^{-1}).

The surface observations used in this study were provided by the MesoWest service from the University of Utah (Horel et al. 2002). These observations include Automated Surface/Weather Observing System (ASOS/AWOS) stations, and mesonet stations from Minnesota, North Dakota, and Hennepin county (MN). The measurements available in each location domain vary due to this variety of agencies. Common parameters include: 2 m temperature, 2 m dew point, 2 m relative humidity, 2 m visibility observations, and 10 m wind speed and direction. Data were collected from all available networks for the individual cases in North Dakota and Minnesota. The locations and names of the stations are described in the tables below. The locations of the observation stations, the elevation of the terrain in the areas of interest, and the land use type are provided along with the station location data later in this chapter.

Weather Research and Forecasting Model

WRF is an eulerian, non-hydrostatic model that can be used to simulate phenomena from the scales on the order meters to global. WRF has two dynamical cores—the Advanced Research WRF (ARW) and the nonhydrostatic mesoscale model (NMM). The former of the two, ARW, is utilized in this study. As fog is a small-scale phenomenon, occurring on the order of some tens of meters to kilometers in areal extent, WRF was configured as a limited area model. This requires the specification of boundary conditions, in addition to initial conditions. WRF also has multiple choices of physics packages for shortwave and longwave radiation, boundary layer physics and turbulence, land surface physics, and microphysics. The simulations were executed as "real data" simulations, as opposed to idealized simulations. It is noted that WRF does have the capability of running in a Single Column Model (SCM) mode, but that capability was not utilized here.

WRF simulations were provided with initial conditions and boundary conditions from the National Oceanographic and Atmospheric Administration's (NOAA) High Resolution Rapid Refresh model (HRRR). The HRRR model was chosen for its fine spatial grid spacing (3 km) and its frequent temporal output (1 hr). NOAA provides an 18 hr HRRR forecast every hour and a 48 hr HRRR forecast every 6 hours. HRRR transitioned to version 4.0 in late 2020; the cases in this study used HRRR version 3.0. HRRR data were obtained from the University of Utah's archive (Blaylock et al. 2017). The Vtable for this HRRR data, which is required for using ungrib.exe and identifies the variables encoded within the HRRR grib files to be extracted for use within the WRF system, was taken from the aforementioned archive. Use of HRRR data as initial and boundary conditions was also chosen for computational efficiency. Through the use of a 3:1 nesting ratio, only one mesoscale nest, with horizontal grid spacing of 1 km, is necessary. This is contrasted with NCEP FNL 0.25° data, whose approximately 27 km grid spacing would require nests of 9 km and 3 km in addition to the 1 km nest. The lack of these extra nests allows the simulations to be

completed more quickly, and with less computational expense, which is important for short term flight planning purposes for sUAS operators.

Because the goal of this study is to examine the utility of using a nested WRF-LES domain for fog forecasting compared to using traditional boundary layer parameterizations at mesoscale domains, WRF-LES (Weather Research and Forecasting – Large Eddy Simulation) was chosen to be run with a grid spacing of 333.33 m and the mesoscale nest is run with a grid spacing of 1 km. To best examine model performance, two boundary layer schemes, YSU and MYNN2, and two microphysics schemes, WSM6 and WDM6, were permuted for a total of 4 mesoscale simulations. To limit the amount of simulations needed, only two LES domains were simulated, one for each microphysics scheme. The configuration of the domains is summarized in Tables 1 and 2.

In the YSU simulations, the option for top-down mixing (ysu_topdown_pblmix) is activated explicitly in the namelist.input file. As discussed in Wilson and Fovell (2018) this modification to the original YSU scheme is a parameterization for the mixing caused by cloud/fog top radiational cooling. The surface scheme selected for the simulations was the Revised MM5 scheme (Jiménez et al. 2012). It is compatible with both the YSU and MYNN boundary layer schemes, as well as in the LES simulation. This allows a more direct comparison of the results, as the impacts of differing surface layer schemes are removed. The RRTMG shortwave and longwave radiation schemes were selected since RRTMG is coupled to the WDM6 and WSM6 microphysics schemes (Bae et al. 2016). Since the scattering of solar radiation by the fog layer is an important factor in its lifecycle, this scheme allows for more realistic impacts of solar-induced sensible and radiative heating during the dissipation phase.

Table 1: WRF Namelist parameters. The namelist number to be used is provided in parentheses.

WRF Parameter	**WRF Namelist choice**
Microphysics	WSM6 (6), WDM6 (16)
Planetary Boundary Layer	YSU (1), MYNN2 (5)
Surface Layer	Revised MM5 (1)
Shortwave Radiation	RRTMG (4)
Longwave Radiation	RRTMG (4)
diff_opt (Diffusion Option)	1
km_opt (K Option)	4
radt (radiation timestep)	5
Horizontal Domain (1 km grid spacing)	Minneapolis: 214 pts x 214 pts Grand Forks 380 pts x 200 pts
Vertical Levels	53
Land Surface Model	Unified Noah (2)
Cumulus Parameterization	0 (not utilized)

Table 2: Large Eddy Simulation Domain. The namelist number to be used is provided in parentheses.

WRF Parameter	**WRF Namelist Choice**
Microphysics Option	WSM6 (6), WDM6 (16)
Horizontal Domain	Minneapolis: 163 pts x 163 pts Grand Forks: 151 pts, 100 pts
Horizontal Grid Spacing	333.33 m
diff_opt	2
km_opt	2
sfs_opt	1
mix_full_fields	.true.

After the mesoscale domain simulations were completed, the LES simulations were initialized using the ndown.exe program available within the WRF framework. The WRF documentation guide (Skamarock et al. 2019) recommends that the ratio of the parent data source to the next be an odd integer. As with the mesoscale domain, the traditional option of 3:1 was used (1 km to 333 m). Higher ratios, such as 5:1 and 9:1, are possible but were not investigated herein. The ndown.exe program allows one to generate initial conditions and boundary conditions from a previous WRF run. This allowed the LES simulations to be started after completion of the mesoscale simulations. The LES was initialized 6 hours into the mesoscale simulations for the Grand Forks case. For the Minneapolis case, the LES was initialized 13 hours after mesoscale

domain initialization. Effectively, these are one-way nested simulations for the 333 m domain. The 333 m domain is forced by the output frequency of the parent mesoscale dataset (every 5 or 10 minutes). The 6 and 13 hr spin-up times for the LES domain are also treated as the spin-up time for the mesoscale domain. The spin-up times between the two fog cases are different due to the domain sizes and thus computational costs involved. The domain size for the mesoscale domain in the Minneapolis case is smaller, and thus a larger spin-up time could be utilized. While longer spin-up times are suggested for modeling fog formation, a shorter spin-up time was selected for timely completion of the simulations. The turbulence closure used within the LES domain is the 1.5 TKE closure to improve the simulations. The Nonlinear Backscattering and Anisotropy (NBA) option is utilized to parameterize subgrid scale (SGS) turbulent motions.

As fog is a boundary-layer phenomena, the model top was lowered from the more commonly used 50 hPa to 100 hPa, and the resolution of the boundary layer is increased following a similar setup to Pinto et al. (2021). Use of a lower model top results in use of fewer vertical levels, offsetting the cost of raising resolution in the boundary layer. Both the mesoscale and LES domains used the same options for the number of vertical levels and vertical resolution; the vertical grid refinement option was not used. Furthermore, roughly 19 of the vertical levels are below 1000 m, with the lowest mass model level located at roughly 10 m above ground level (AGL). The time steps chosen were 3 s for the mesoscale domain and 1 s for the LES domain. This is shorter than the recommended $6*\Delta X$, where ΔX is the horizontal grid spacing in km. Due to the increase in vertical resolution in the lowest kilometer, the recommended time step was halved to avoid issues with model stability.

It should be noted that the vertical and horizontal resolutions used in this study are quite coarse; a true LES of the stable boundary layer would require vertical and horizontal resolutions

on the decameter scale or smaller due to the small sizes of eddies in that regime Cuxart (2015). The computational cost of this would be prohibitive for use in a forecasting environment, so the behavior of the 3D turbulence closure schemes at the larger gray zone resolutions are investigated instead for their utility in forecasting the behavior and life cycle of fog. This situation was met with a compromise—use of the specially-designed grey zone boundary layer parameterization schemes available within the WRF framework. The SMS-3DTKE scheme (a turbulence parameterization scheme), first available with WRFV4.2, is also tested in this study. This scheme is designed to be self-adaptive to model resolution, and can be used with mesoscale, gray-zone, and LES resolutions (Zhang et al. 2018).

The land use classification for the mesoscale Minneapolis domain is shown in Figure 1. The map projection used by the WRF and the WRF Preprocessing System (WPS) is Lambert Conformal Conic. The land use utilizes the MODIS-IGBD 20 class land use dataset. The resolution of the dataset is 30 arcseconds, which is roughly 900 m in length. The land use categories within the domain are largely croplands (12), Urban/Built-Up (13), and Cropland/Vegetation Mosaic (14). While not the primary focus of this study, land use classification can have large impacts upon the lifecycle of fog, as this controls fluxes of heat and moisture at the land surface. The terrain height is provided in Figure 2, and locations of the observations are provided in Table 3.

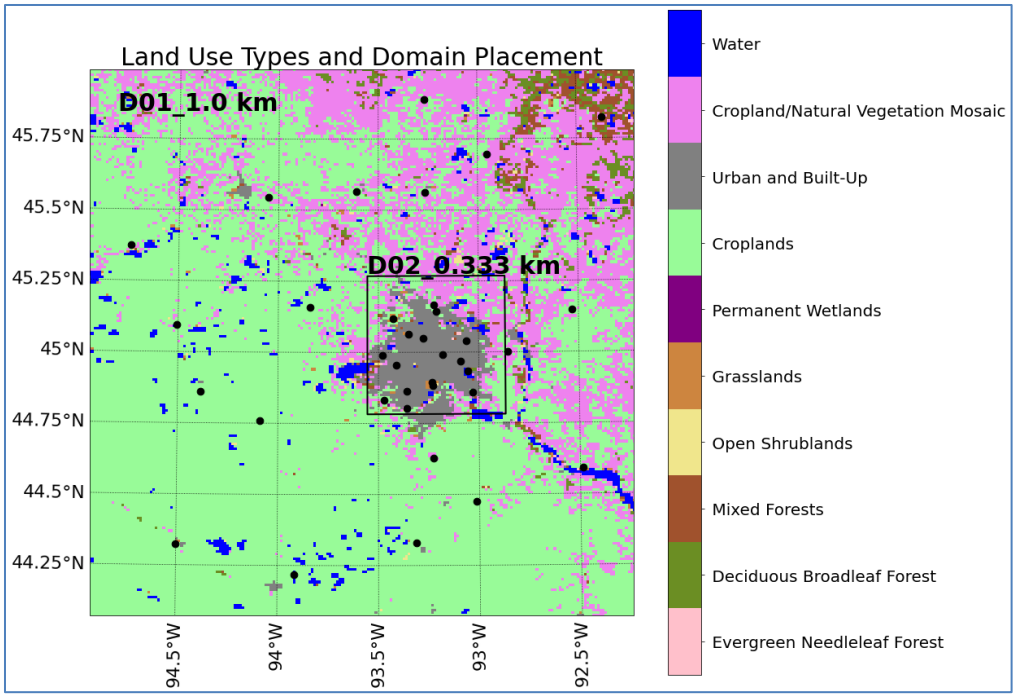

Figure 1: Land Use Classification of the Minneapolis event domain.
The black box shows the LES domain

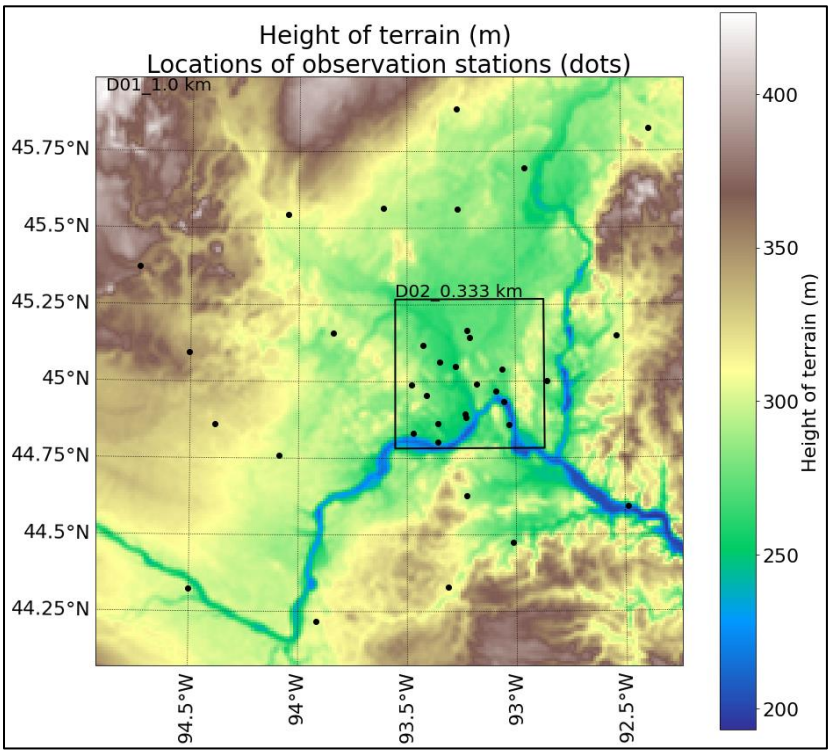

Figure 2: Terrain Height in the Minneapolis area domain.
The boundaries of the inner LES domain are shown with the black box.

Table 3: Station locations for the Minneapolis fog event.

Station	**Latitude**	**Longitude**		Station	**Latitude**	**Longitude**		Station	**Latitude**	**Longitude**
HPN02	45.1182	-93.4283		KFBL	44.32983	-93.3119		KRGK	44.5926	-92.4844
HPN07	44.89519	-93.2317		KFCM	44.83217	-93.4705		KRNH	45.14762	-92.5335
HPN09	44.98992	-93.4791		KGYL	44.7588	-94.0905		KROS	45.69628	-92.9542
HPN20	44.95556	-93.4114		KHCD	44.85961	-94.3855		KRZN	45.82278	-92.3725
HPN21	45.04889	-93.2761		KJMR	45.88863	-93.269		KSGS	44.86006	-93.032
HPN24	44.86346	-93.3567		KLJF	45.09485	-94.5084		KSTC	45.54415	-94.0517
HPN26	44.80384	-93.3589		KLVN	44.62778	-93.2281		KSTP	44.93237	-93.0559
HPN30	44.99026	-93.1799		KMIC	45.0625	-93.3508		KSYN	44.47362	-93.0145
HPN31	45.16541	-93.2246		KMKT	44.21667	-93.9167		KULM	44.32274	-94.5024
K21D	45.0002	-92.8549		KMSP	44.88306	-93.2289		MN088	45.03843	-93.0625
KANE	45.14258	-93.2127		KPEX	45.37247	-94.7388		MN089	44.96796	-93.0907
KCBG	45.56275	-93.2644		KPNM	45.56425	-93.608		KCFE	45.15889	-93.8431

The land use for the Grand Forks mesoscale domain is illustrated in Figure 3. As with the Minneapolis domain, the land use dataset is the 30 arcseconds MODIS IGBD 20 class land use dataset. The land use categories in the mesoscale domain are primarily Croplands (12), Croplands/Natural Vegetation Mosaic (14), and Urban/Built-Up (13) land classes. The height of the terrain above MSL is also provided in Figure 3. The variation and gradients in the terrain height small across the domain, and the Red River valley is captured in the center of the domain. The locations of the stations are provided in Figure 3 and Table 4.

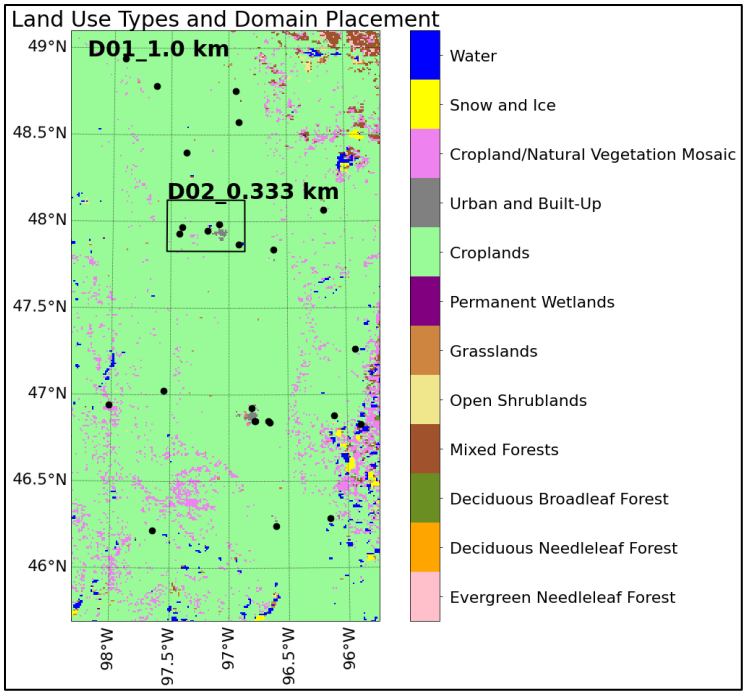

Figure 3: Land Use types within the North Dakota domain.
The boundary of the innermost LES domain, located over Grand Forks at 48° N, is indicated by the black box.

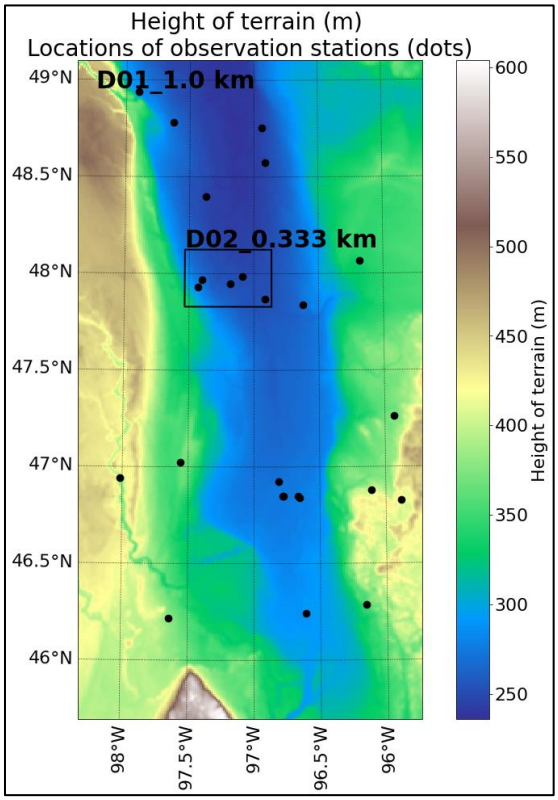

Figure 4: Height of the terrain within the North Dakota domain
The boundary of the innermost LES domain, located over Grand Forks at 48° N, is indicated by the black box.

Table 4: Station Locations within the Red River Valley region

Station	Latitude	Longitude		Station	Latitude	Longitude
K2C8	97.56754	-195.259		KHCO	97.5049	-193.875
K3N8	94.521	-191.856		KJKJ	93.6808	-193.309
K96D	97.88034	-195.811		KRDR	95.93334	-194.8
KBAC	93.8824	-196.036		KTVF	96.13334	-192.367
KBWP	92.48778	-193.214		MN013	93.69358	-193.336
KCKN	95.68084	-193.24		MN024	97.14472	-193.83
KDTL	93.65708	-191.771		MN060	95.73662	-193.834
KFAR	93.85056	-193.622		MN062	93.7549	-192.223
KFFM	92.5731	-192.307		MN098	93.6942	-193.555
KGAF	96.8	-194.74		ND010	95.86516	-194.858
KGFK	95.89612	-194.365		ND013	93.69566	-193.566
KGWR	92.4374	-195.287		ND014	94.0446	-195.115
				ND019	95.9694	-194.171

Contingency Tables and Error Metrics

Model performance is analyzed using contingency tables (Menut et al. 2014; Cui et al. 2019; Wilks 2011). These contingency tables allow for a dichotomous yes/no interpretation of the verification of fog occurrence (Table 5 and Table 6). In this study, the model output fields were compared to the nearest observation. For the Grand Forks simulations, model output was saved every 10 minutes due to concerns regarding computational and storage costs. Later it was discovered that this cost was not prohibitive and model output was saved every 5 minutes. For model output written every 10 minutes, the nearest observation in time within a ± 5 minute period was used for comparison. For model output is written every 5 minutes, the nearest observation within a ± 2 minute period was used instead.

Table 5: Example Contingency Table

Modeled Event(s)	Observed = Yes	Observed = No
Forecasted = Yes	a = Hit	b = False Alarm
Forecasted = No	c = Miss	d = Correct Rejection

Multiple performance metrics can be generated from these contingency tables. These performance metrics and contingency metrics were generated for each station for each model run.

To have a more holistic interpretation of model performance, all stations were amalgamated into contingency tables for each individual model run. The metrics used include the Probability of Detection (POD), False Alarm Ratio (FAR), Bias (BIAS), Threat Score (TS), and Accuracy (ACC), and Heidke Skill Score (HSS).

Table 6: Table of Equations for contingency table metrics.
Variables are as defined in Table 5.

Name	**Equation**	**No.**
Probability of Detection (POD)	$a \,/\, (a + c)$	2
False Alarm Ratio (FAR)	$b \,/\, (a + b)$	3
Bias (BIAS)	$(a + b) \,/\, (a + c)$	4
Accuracy (ACC)	$(a + d) \,/\, (a + b + c + d)$	5
Threat Score (TS)	$a \,/\, (a + b + c)$	6
Heidke Skill Score (HSS)	$\dfrac{[2 * (ad - bc)]}{(a+c)(c+d) + (a+b)(b+d)]}$	7

The POD represents the proportion of observed events that the model is able to forecast correctly. It ranges between 0 and 1, with 1 being a perfect score. The FAR represents the percentage of false alarms to the total forecasted events. The score ranges between 0 and 1, with a perfect score being 0. The BIAS represents the ratio of the forecasted event count to the actual event count. In this case it represents the ratio of events forecasted as fog to events where fog actually occurred. This allows one to determine if an event was over-forecasted or under-forecasted (Wilkes 2011). An ideal BIAS is 1. A score of below 1 represents an under-forecasted event; a score larger than 1 represents an over-forecasted event.

As in Wilkes (2011), the TS is useful when “yes” events are rarer than “no” events in the observations. The ACC may be misleading if the observed “yes” events are rare; the accuracy score would be dominated by “correct rejections”. The TS ranges between 0 and 1, with 1 being the ideal score. It is useful for stations that have few observations/model output times where fog is observed. The ACC represents the proportion of events that the model forecasted correctly.

Contrasted with POD, this includes Correct Rejections and Missed events. The HSS ranges between 1 and -∞ , with 1 being a perfect forecast, and negative numbers representing poor forecasts. A score of 0 represents a forecast with no skill.

The accuracy of scalar variables are represented through the BIAS, Mean Absolute Error (MAE), Mean Squared Error (MSE), Root Mean Square Error (RMSE), and the correlation coefficient (*r*). As with Cui et al. (2019), the results on the innermost 333.33 m grid domain are compared to the results of the 1 km domain. Their formulations follow from (Wilks 2011):

$$MAE = (1/n)\sum_{i=1}^{n}|m_i - o_i|, \tag{8}$$

$$MSE = (1/n)\sum_{i=1}^{n}(m_i - o_i)^2, \tag{9}$$

$$BIAS = (1/n)\sum_{i=1}^{n}(m_i - o_i), \tag{10}$$

$$RMSE = \sqrt{MSE}, \tag{11}$$

and

$$r = \frac{\sum_{i=1}^{n}(m_i - \underline{m})(o_i - \underline{o})}{\sqrt{\sum_{i=1}^{n}(m_i - \underline{m})}\left(\sqrt{\sum_{i=1}^{n}(o_i - \underline{o})}\right)}, \tag{12}$$

where forecasts are represented by ***m*,** observations by *o*, and *i* represents an individual time where the forecasts and observations are paired.

Model output times do not always align perfectly with the times of observations. Forecasts were matched to the nearest observation within +/- 5 or 2 minutes, depending on model output frequency. Observations were matched to the nearest model grid point through the nearest neighbor approach. Domain wide metrics of MAE, MSE, and BIAS, RMSE, and correlation coefficient were also calculated through taking the mean of the relevant score across all stations.

Visibility

As the reduction in visibility due to hydrometeors is not explicitly predicted in WRF, visibility must be parameterized. Visibility is parameterized through the cloud liquid water content (QCLOUD) at the first mass model level (roughly at z = 10 m). One common measure of visibility is that of Stoelinga and Warner (1999), hereafter SW1999. While there are many methods to calculate visibility in fog, only a few are selected here. The SW1999 method assumes that extinction of light is due to the liquid water content (or ice water content) of hydrometeors. This method has a drawback in that it does not consider the number concentration of fog droplets (Gultepe et al. 2006). In WRF, the droplet number concentration is a prognostic variable in the WDM6 scheme, while it is held constant in the WSM6 scheme. This presents a possible benefit for using a double moment scheme.

$$\beta = 144.7 * (LWC)^{0.88}, \tag{13}$$

$$Visibility\ (km) = -ln(0.05) / \beta, \tag{14}$$

An alternative equation is used in the RUC model that depends on relative humidity (Gultepe and Milbrandt 2010; Kutty et al. 2021). This allows forecasting reduced visibility in cases where liquid hydrometers do not exist, and is given by

$$Visibility\ (km) = 60 * exp(-2.5 * (RH_w - 15)/80), \tag{15}$$

One additional set of metrics used when analyzing fog are the times of fog formation, the time of fog dissipation, and the number of fog hours. Similar to the previous performance parameters, observations are compared to the first model level at the nearest model grid point. The offset of the modeled time formation/dissipation, in minutes, is provided for multiple observation stations.

Satellite Data

Satellite data for the fog events were collected with the Moderate Resolution Imaging Spectroradiometer (MODIS) (MODIS Science Team 2017a,b). As the sensor provides top-of-atmosphere reflectance of visible and near infrared light, the data must be used to examine total cloud coverage, rather than just fog. The MODIS data are provided at a resolution of 1.0 km and are provided by Level-1 and Atmosphere Archive & Distribution System (LAADS) Distributed Active Archive Center (LAADS DAAC). The MODIS data are not continuously available during the events; two overpasses are available for both the Minneapolis event and the Grand Forks event. Additionally, data from the Advanced Baseline Imager (ABI) aboard GOES-16 were used; this has continuous availability throughout both events. The GOES imagery were accessed through the goes2go python package, a proxy for the Amazon S3 website Blaylock (2022). During the nocturnal phases of the fog events, the brightness temperature difference (BTD) method was used to determine spatial coverage of fog (Cermak and Bendix 2008). This compares the 10.3 um and 3.9 um brightness temperatures. Fog and stratus are more emissive in the region of 10.3 um of the electromagnetic spectrum than in the region of 3.9 um. If satellites have direct line of sight to the fog, this difference in emissivity will produce a positive (> 0 K) difference. Higher clouds will produce a negative brightness temperature difference (< 0 K.) Additional products used were the RGB products from GOES, including the Nighttime Microphysics RGB, Day Cloud Phase, Day/Snow/Fog, and True Color products. As the fog BTD method is mainly for use at nighttime, these products help to discern fog and other clouds during the daytime and to discern fog from snow (Cooperative Institute for Mesoscale Meteorological Studies 2022; Cooperative Institute for Research in the Atmosphere 2022a,b,c). An appendix is provided with the legends for the interpretation of the RGB imagery.

Post Processing and Computations

Post processing of the output files produced with the WRF model was largely done in the Python programming language. Various versions of the languages were used—mainly version 3.6 and onwards. Packages crucial to post processing were wrf-python, xarray, cartopy, numpy, pandas, and matplotlib (Ladwig 2017; Hoyer and Hamman 2017; Elson et al. 2021; Harris et al. 2020; Reback et al. 2021; Caswell et al. 2021). These packages are publicly available free of charge. The many intersecting package dependencies were managed using the Anaconda software environment (Anaconda, Inc. 2022). High-performance computing support from Cheyenne (doi:10.5065/D6RX99HX) was provided by NCAR's Computational and Information Systems Laboratory, sponsored by the National Science Foundation.

Chapter 3 – Fog Event in Minneapolis on 10 September 2020

Formation and Dissipation Times

Formation and dissipation times are provided for the stations of the innermost domain in Table 7. Fog formed after a rain event over the domain ended near the end of the model spin-up period. The area in question is in the CST time zone with a UTC offset of -5:00 hours. Across the whole domain the fog in the area began to be observed at 1:53 UTC at KMIC an hour after sunset and dissipated around sunrise for most locations (12 UTC local time). The formation of fog coincided with a partial clearing of skies after the rainfall on 9 September 2020.

Table 7: Formation and dissipation times (UTC) of observed fog in the innermost Minneapolis domain

	Formation	Dissipation
KANE	03:35:00	13:45:00
KFCM	05:50:00	13:53:00
KMIC	01:53:00	14:53:00
KMSP	06:30:00	13:25:00
KSGS	04:55:00	13:15:00
KSTP	06:10:00	13:15:00
MN088	05:15:00	12:50:00

Formation and dissipation times are provided in Table 8(a,b) for each model run using the SW1999 parameterization (traditional visibility formulation). The formation and dissipation times given for the multi-rule framework similar to that of Zhou and Du (2010) are provided at the end of this section. Furthermore, to examine the impact of droplet number concentration on visibility, the formation/dissipation times using the parameterization of Gultepe et al. (2006) is provided later in this document. The inability to achieve saturation in the lowest model layer is apparent in the

formation offset times in Figure 5 and Figure 6. The formation offset is large, occurring hours later, as seen with the WSM6_YSU results in Figure 5.

One of the strongest influences in the differences between the formation times between the mesoscale simulation is the near-surface moisture field. The rain event that occurred on 9 September 2021 provided moisture to the surface. As the model was unable to properly simulate the rainfall (notably at KMSP), it took longer for the air to cool to saturation at some stations, thus presenting a delay in fog formation. For example, 3.56 mm of rain was recorded at KMSP (from ASOS reports), while the model simulations ranged from 0.56 mm to 1.50 mm (Figure 22, Table 16). While it is not a focus of the study, further simulations could be performed to study the impact of domain size and spin-up time on the precipitation placement and subsequent fog formation.

Warm biases were noted in the mesoscale simulations at KSTP, KANE, KFCM, KMSP, and KSGS, and especially at the Hennepin County mesonet stations (prefix HPN). The LES models for many stations have a cold bias, sometimes prior to fog onset. Furthermore, many stations also have a dry bias, notably at KFCM and KMSP. KSTP, while having a dry bias, has a less significant dry bias across model runs compared to other stations. Here, the precipitation was more realistically represented in the model—the ASOS station recorded 4.06 mm while model estimates ranged from 2.75 mm to 4.19 mm. Across all stations there was a positive bias in wind speed. Part of this bias is likely due to the way that ASOS reports wind speeds. The lowest reportable wind speed is 2 kts (approximately 1.02 m s^{-1}) Despite this fact, modeled wind speeds remain above 1.02 m s^{-1} at the time calm winds (0 m s^{-1}) are reported, thus a positive bias in wind speed remains in place. Regarding formation and dissipation times, results are mixed. For some stations the sub-kilometer domain improves the formation and dissipation times, while for others it is worse than the mesoscale domain. YSU_WDM6 was used to initialize the sub-kilometer

domains. The forecast for fog at KMSP improves from no formation at all in the mesoscale YSU_WDM6 simulation to having fog formation within the sub-kilometer LES_WDM6. Similarly, the forecast improves at MN088 and KSTP. Yet, this comes at a cost for the formation time at KFCM. LES_WSM6 does show a marked improvement over MYNN_WSM6, with improvements at KANE, MN088 and KMIC. While formation times are generally late, this sub-kilometer run improved upon the times from the mesoscale run. Fog at many stations forms late and dissipates well before sunrise.

Table 8(a,b): Formation and dissipation times using SW1999.
Dissipation times with None indicate that the fog never formed in the model, or that the fog failed to dissipate by the end of the simulation.

	MYNN_WSM6	YSU_WDM6	LES_WDM6
KANE	Formation: 10:55 'Dissipation: 12:45	Formation: 09:50 Dissipation: 11:55	Formation: 04:35 'Dissipation: None
KFCM	Formation: 08:00 'Dissipation: 13:55	Formation: 06:10 Dissipation: 13:55	Formation: 07:45 'Dissipation: 15:55
KMIC	Formation: None Dissipation: None	Formation: 10:15 'Dissipation: 10:35	Formation: 07:55 Dissipation: None
KMSP	Formation: 11:30 Dissipation: 11:40	Formation: None Dissipation: None	Formation: 08:35 Dissipation: 13:40
KSGS	Formation: 08:10 Dissipation: 12:40	Formation: 06:20 'Dissipation: 08:35	Formation: 05:45 'Dissipation: 11:55
KSTP	Formation: 08:25 Dissipation: 12:30	Formation: 07:15 Dissipation: 09:45	Formation: 05:40 Dissipation: 11:10
MN088	Formation: None Dissipation: None	Formation: 08:20 Dissipation: 09:10	Formation: 05:00 Dissipation: 14:05

	WDM6_MYNN	LES_WSM6	YSU_WSM6	3dtke_WSM6
KANE	Formation: 07:00 Dissipation: 13:35	Formation: 05:30 'Dissipation: 13:50	Formation: 11:30 'Dissipation: 13:00	Formation: 10:45 Dissipation: 13:10
KFCM	Formation: 06:20 Dissipation: 13:50	Formation: 08:05 Dissipation: 14:00	Formation: 07:05 'Dissipation: 14:05	Formation: 07:45 'Dissipation: 13:20
KMIC	Formation: 11:25 'Dissipation: 13:15	Formation: 08:40 Dissipation: 08:55	Formation: None, Dissipation: None	Formation: None Dissipation: None
KMSP	Formation: None Dissipation: None	Formation: 09:50 'Dissipation: 13:30	Formation: 10:20 'Dissipation: 12:05	Formation: 10:40 'Dissipation: 12:35
KSGS	Formation: 06:55 'Dissipation: 08:40	Formation: 08:10 Dissipation: 12:25	Formation: 08:10 Dissipation: 12:35	Formation: 07:35 'Dissipation: 12:00
KSTP	Formation: 07:35 'Dissipation: 10:05	Formation: 08:35 'Dissipation: 13:00	Formation: 08:25 Dissipation: 13:05	Formation: 07:45 Dissipation: 11:55
MN088	Formation: 08:25 'Dissipation: 09:15	Formation: 05:45 Dissipation: 13:40	Formation: 12:20 Dissipation: 12:25	Formation: 08:10 Dissipation: 12:45

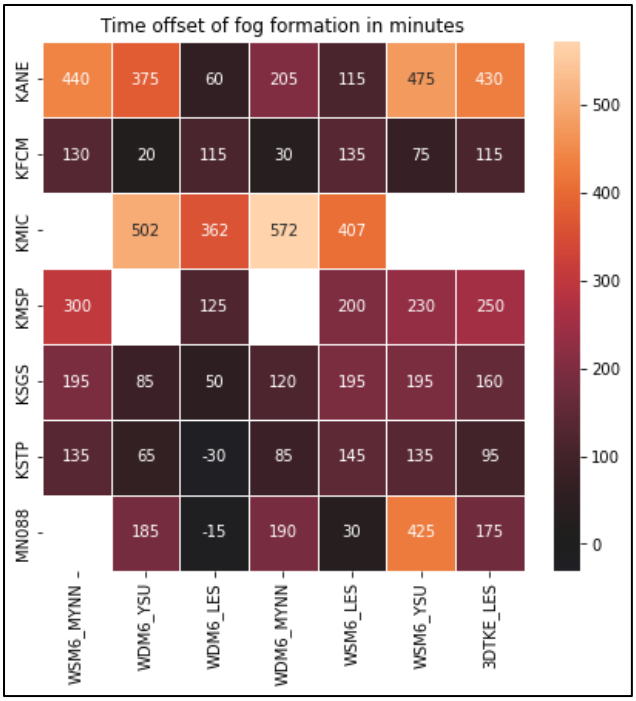

Figure 5: Time offsets of fog formation in models as compared to observations.

White boxes indicate that no modeled fog had formed.

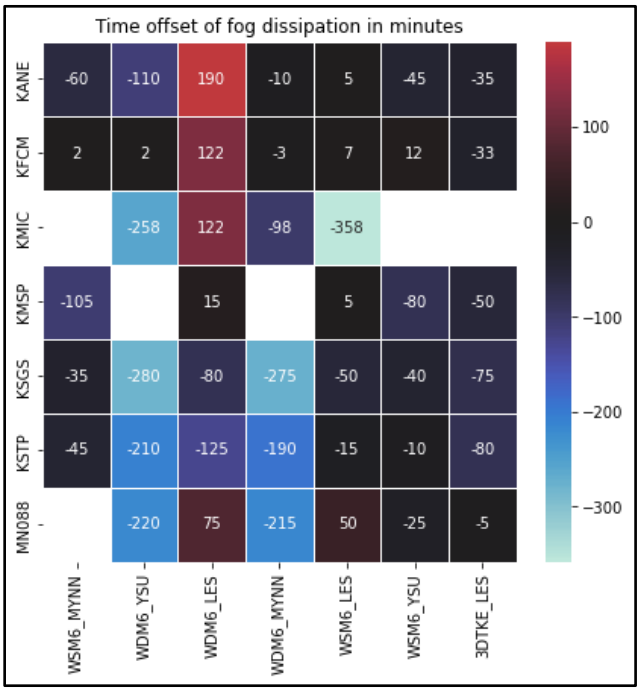

Figure 6: Time offsets of fog dissipation in models as compared to observations. White boxes indicate that no modeled fog had formed, or had failed to dissipate by the end of the model run.

Contingency Tables and Model Performance

Table 9(a,b) provides performance metrics averaged across the entire LES domain for each station within the Minneapolis metropolitan area. The false alarms remain relatively low with the exception of LES_WDM6. Biases are also below 1, meaning that the models predicted less fog than actually occurred for all model runs. The LES_WSM6 and LES_WDM6 model runs had improved performance compared to all mesoscale domains in terms of Threat Score and Probability of Detection; 3DTKE_WSM6 had similar performance to YSU_WSM6, but improved performance compared to the three other mesoscale domains. Too persistent fog that failed to dissipate at some stations in LES_WDM6 contributed to its higher False Alarm Ratios. This can be seen in the individual station plots (Figure 23-29). KANE, KFCM, and KMIC shows persistent low visibility in the model well after dissipation time for LES_WMD6.

As many stations were located outside the innermost domain, but still within the outermost domain, a second set of statistics is provided in Tables 9b and 10a to provide for additional comparisons for the coarse mesoscale model performance. Bias and FAR dramatically increase. The model had simulated the fog at the stations surrounding the Minneapolis area with marginally better skill, with an associated increase in False Alarms. There is a domain wide drop in average 2 m temperature bias when considering the non-metro observations. This demonstrates the impact of land use and surface heat fluxes upon fog formation and dissipation. Both KANE and KMIC are classified as the “Urban and Built-Up” land use classification in WRF, while KMSP is classified in the “Grassland” land use category. These categories have different albedos, heat capacities, etc. The fog at KMSP formed late, but had a mean temperature bias closer to zero, especially in the pre-fog period. As the sensible heat fluxes/latent heat fluxes and soil temperature are important for fog forecasting (Smith et al. 2021), the representation of land use is an important

factor that must be considered when using models. Figure 7 illustrates the strong warm bias that occurred at KANE/KMIC. Across all WRF simulations, the 10 m wind speed bias/MAE was roughly 1 m/s at most stations (Figure 8). The wind speeds were calm at most stations (Figures 19-25) throughout the event. The dew point MAE remains below 2 K for most stations and the bias is ± 1 K for many of the stations. While positive biases exist in dew point, there are often simultaneous positive biases in temperature at these stations, leading to the reported late fog formation times seen at the stations (Figure 7,8).

Table 9a: Performance metrics for WRF fog prediction

	POD	Accuracy	FAR	Bias	Threat Score	HSS
WSM6_MYNN	0.25	0.63	0.02	0.26	0.25	0.25
WDM6_YSU	0.28	0.64	0.07	0.30	0.28	0.27
WDM6_LES	0.69	0.76	0.21	0.86	0.58	0.52
WDM6_MYNN	0.31	0.65	0.09	0.34	0.30	0.28
WSM6_LES	0.46	0.72	0.08	0.51	0.45	0.43
WSM6_YSU	0.34	0.67	0.04	0.35	0.34	0.34
WSM6_3dtke	0.34	0.67	0.08	0.37	0.33	0.32

Table 9b: Performance of the Mesoscale domains considering all points in the outer domain.

	POD	Accuracy	FAR	Bias	Threat Score	Heidke Skill Score
WSM6_MYNN	0.47	0.69	0.30	0.67	0.39	0.33
WDM6_YSU	0.53	0.68	0.36	0.82	0.41	0.32
WDM6_MYNN	0.51	0.68	0.34	0.77	0.40	0.33
WSM6_YSU	0.52	0.71	0.29	0.73	0.43	0.38

Table 10a: Performance of the Mesoscale domains considering all points in the outer domain.

	WSM6_MYNN	WDM6_YSU	WDM6_MYNN	WSM6_YSU
T2 Bias (K)	1.03	0.78	0.84	1.04
T2 MAE (K)	1.73	1.88	1.84	1.71
Td2 Bias (K)	-0.10	0.22	0.14	-0.06
Td2 MAE (K)	1.35	1.46	1.48	1.27
WS Bias (m s^{-1})	1.06	1.06	1.02	1.10
WS MAE (m s^{-1})	1.23	1.18	1.15	1.26
RH Bias (%)	-6.37	-3.03	-3.85	-6.11
RH MAE (%)	8.86	6.98	7.31	8.57

Table 4b: Performance of the models against the stations within the innermost LES domain

Domain scores	WSM6 MYNN	WDM6 YSU	WDM6 LES	WDM6 MYNN	WSM6 LES	WSM6 YSU	WSM6 3DTKE
T2 Bias (K)	2.10	1.90	-0.08	1.79	0.49	2.25	0.92
T2 MAE (K)	2.37	2.34	1.66	2.24	1.42	2.42	1.45
Td2 Bias (K)	-0.08	0.53	-0.43	0.26	-0.67	0.16	-0.46
Td2 MAE (K)	1.31	1.41	1.45	1.38	1.49	1.30	1.38
WS Bias (m s^{-1})	0.83	0.82	0.86	0.77	0.93	0.89	0.87
WS MAE (m s^{-1})	0.98	0.93	0.97	0.90	1.05	1.01	1.02
RH Bias (%)	-12.84	-8.23	-2.28	-9.15	-7.42	-12.28	-8.72
RH MAE (%)	13.39	9.61	5.28	10.32	7.87	12.85	9.06

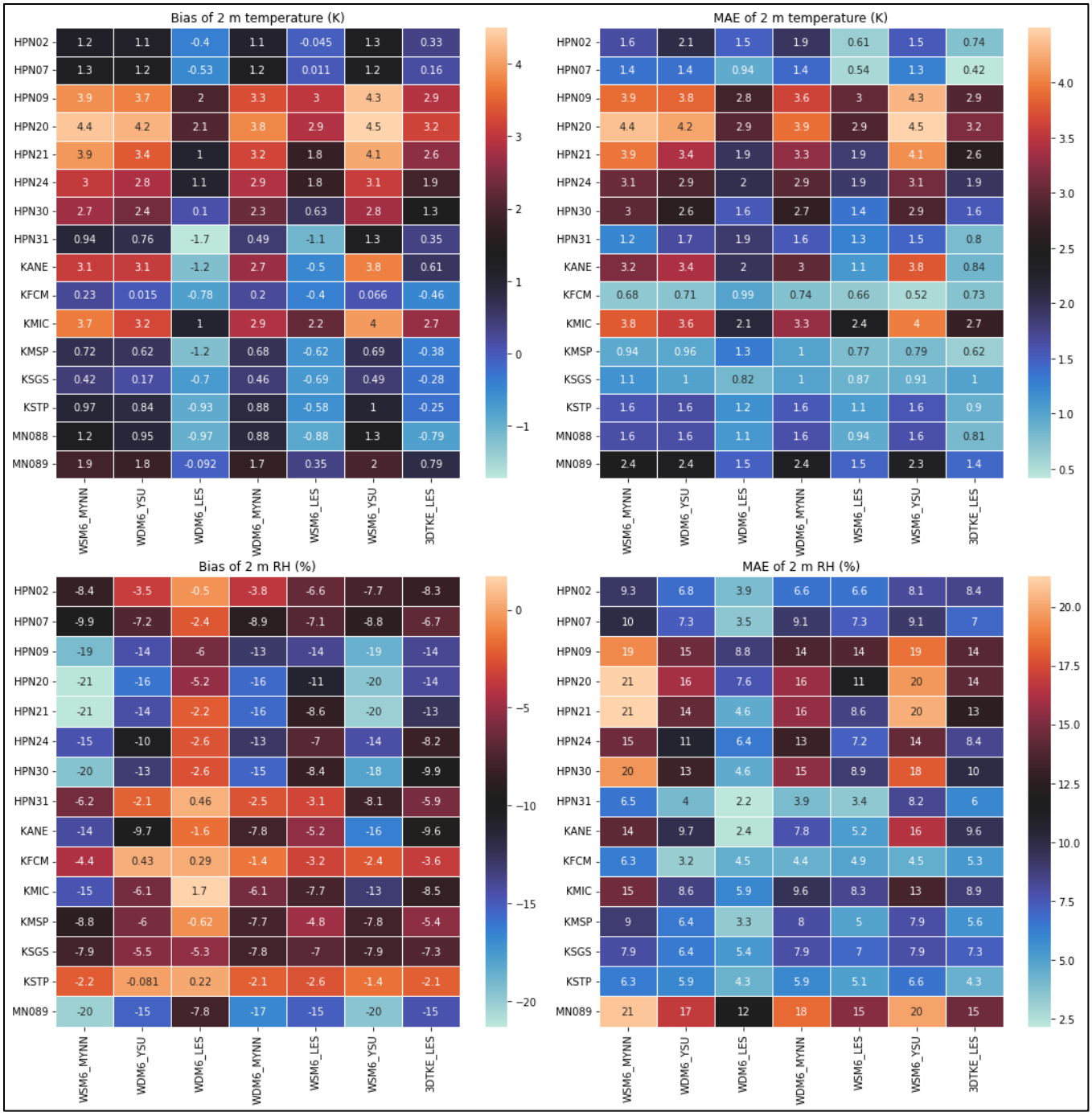

Figure 7: Performance metrics of individual stations for 2 m temperature and 2 m RH. The metrics are the bias and mean absolute error (MAE) of 2 m temperature and relative humidity.

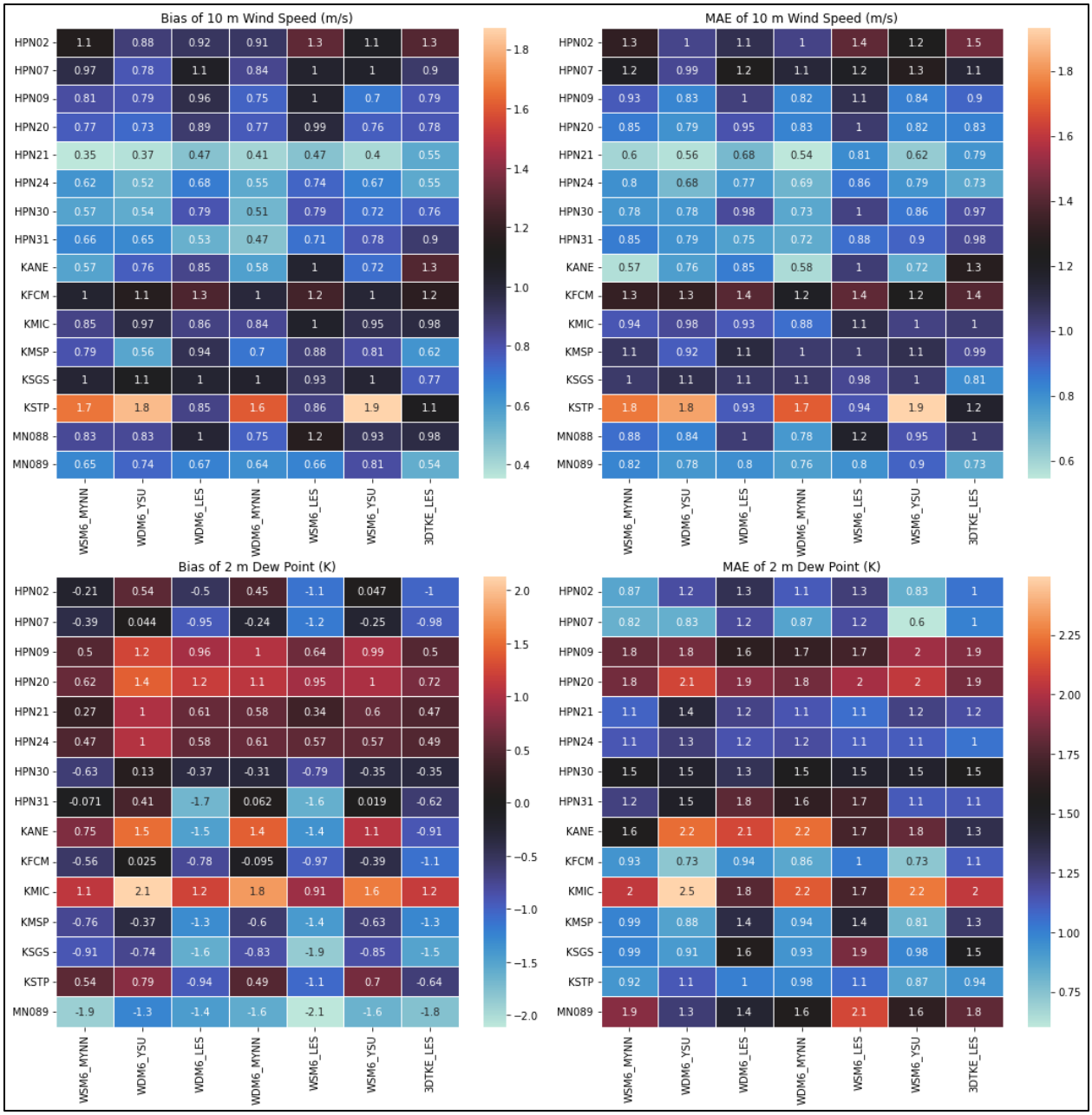

Figure 8: Performance metrics of individual stations for 10 m wind speed and 2 m dew point. The metrics are the mean absolute error (MAE) and bias in 2 m dew point and 10 m wind speed.

Taylor Diagram Discussion

Taylor Diagrams are a useful tool for model comparison as they present correlation coefficient, standard deviation, and root mean square difference in one diagram. In such a diagram, the angle represents correlation coefficient between a modeled parameter and an observed parameter. The distance from the origin represents the standard deviation of observations/model data, while the root mean square difference (a measure of model error) is represented by the radial distance from the red dot on these diagrams. Points closest to the observed points represent more accurate forecasts, and points further away represent less accurate forecasts. At KMSP, the WDM6-LES has a low correlation coefficient of 2 m temperature due to the persistence of the fog (Figure 9a). While the models are most accurate during the night and early morning in terms of 2 m temperature at KMSP, the overly persistent fog keeps the temperatures too cool. This leads to the overall large RMSD in observations. The RMSD for dew point is small (below 1 K). There is a scatter in the correlation coefficient in the model runs, which can partially be attributed to inter-model differences in fog formation and dissipation times.

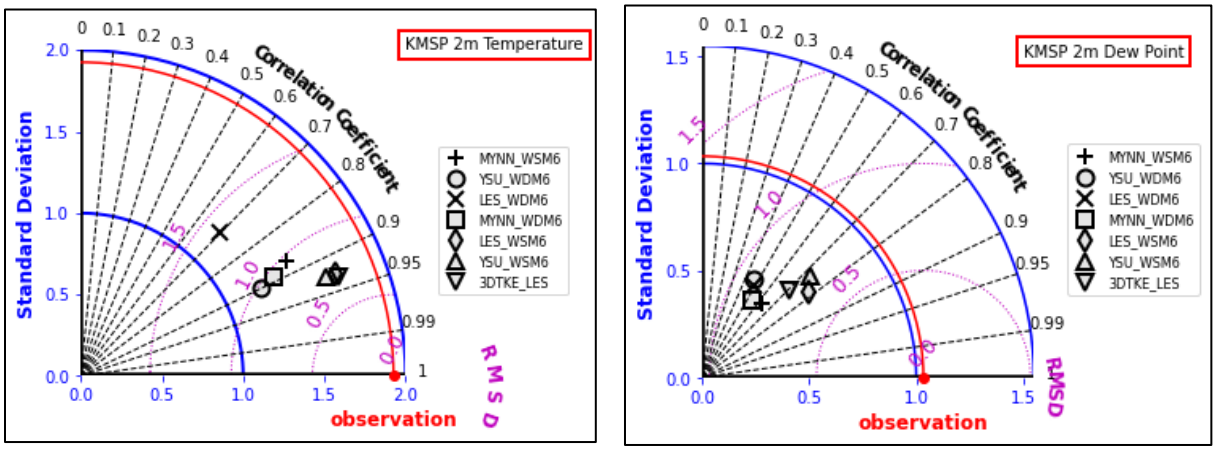

Figure 9(a,b): Taylor Diagrams of model performance for 2 m temperature and dew point.

HRRR Comparison

To fully examine the benefit of using a sub-kilometer forecast, it is useful to evaluate formation/dissipation times for a HRRR model simulation. It is noted that the HRRR forecast/analysis fields are only available in hourly increments. The nearest 15 minute observation to the hour was used to validate the HRRR model. The surface meteorological parameter biases are also examined for this instance. Instead of the analysis time fields (F00), HRRR forecast files are examined. While the WRF model was initialized at 11 UTC 9 September 2020, the 12 UTC 9 September 2020 initialized HRRR forecast was examined as it contained a longer forecast period and is still relatively close to the 11 UTC initialization time. The 12 UTC initialized HRRR forecast fails to capture the onset of fog at all observation stations in the region (Table 11). Later initialization times produce better fog onset/dissipation times, but still have timing offsets or missed fog at KSGS, KSTP, and KMSP. The model struggled at KSGS and KSTP.

HRRR model domain wide biases of 2 m temperature, relative humidity, and dewpoint are presented in Table 12. As is to be expected, model biases improved with initialization times closer to the start of the fog event. A small warm bias in 2 m temperature and dry bias in relative humidity is also present in the F00 forecast hours (analyses), which serve as boundary and initial conditions for the WRF simulations.

Table 11: Fog formation and dissipation for various HRRR initialization times.

	Initialized: 09SEP12 UTC	Initialized: 09SEP18 UTC	Initialized: 09SEP22 UTC
KANE	None	Formation: 09:00 Dissipation: 12:00:00	Formation: 06:00 Dissipation: 12:00:00
KFCM	None	None	Formation: 07:00 Dissipation: 13:00:00
KMIC	None	Formation: 10:00 Dissipation: 12:00:00	Formation: 06:00 Dissipation: 12:00:00
KMSP	None	Formation: 10:00 Dissipation: 12:00:00	Formation: 09:00 Dissipation: 13:00:00
KSGS	None	None	None
KSTP	None	None	None
MN088	None	Formation: 07:00 Dissipation: 12:00	Formation: 06:00 Dissipation: 12:00

Table 12: Error Metrics for various HRRR initializations.

	HRRR-Analyses	HRRR - 12Z	HRRR - 18Z	HRRR - 22Z
T2-Bias (K)	0.110	2.962805	1.746	0.385
T2-MAE (K)	0.752	2.962996	1.810	0.945
T2-RMSE (K)	0.891	3.104582	1.971	1.137
Dew point-Bias (K)	0.234	1.423434	1.233	0.213
Dew Point-MAE (K)	0.789	1.679905	1.411	0.860
Dew Point-RMSE (K)	0.955	1.885885	1.568	1.026
RH-Bias (%)	-0.573	-13.9045	-7.667	-5.627
RH-MAE (%)	4.458	13.91274	7.990	6.497
RH-RMSE (%)	5.887	14.93877	9.215	7.646

Time-Height Cross Sections of Fog for mesoscale domains

No vertical observations of this event are available, so only model forecast comparisons are possible. An important factor in the life-cycle of fog is its depth and variation of liquid water content with height over a single location (grid point). KMSP was selected for its importance within the region. At KMSP, both YSU-WDM6 and MYNN-WDM6 fail to produce fog at the surface (Figure 10). Instead, liquid water content (LWC) forms as low stratus in the middle of the boundary layer. The WSM6 mesoscale schemes do form fog at the surface, but it is short lived (both last for only a short time compared to the actual length of the fog event). The sub-kilometer

domains (LES) have fog forming at the surface and building upwards. Eventually, the fog dissipates and forms a low stratus cloud. Between formation and dissipation times at the surface, the top of the LWC layer gradually rises as the fog deepens. As the fog weakens in the early morning hours, the visibility gradually increases. In WDM6-LES and WSM6-LES the fog weakens and reforms at the surface. The WDM6 has persistent LWC throughout the daylight periods of the simulation period above KMSP. The highest liquid water exists near the fog top during many time periods in these simulations.

Within the state of Minneapolis lie micrometeorological stations at which surface fluxes are measured. While these lie outside of the LES domain, they are still valuable for understanding model performance as the mesoscale domain drives the performance of the simulation domain. The data are provided through the Ameriflux network (Baker and Griffis 2018). While visibility is not recorded at these sites relative humidity recorded at the station is still valuable as it is an indicator of fog. The site is located over a grassland type landcover. Observation data are averaged over 30 minute periods in the dataset. As the WRF variables are instantaneous model outputs, WRF variables were also averaged into 30 minute groups. Sensible and latent heat flux data were missing throughout a large duration of the fog period, and thus are not reported here.

In the simulations, fog generally formed between 4:00 and 6:00 UTC (Figure 11), where fog began at 04:55 UTC. The decrease in net longwave radiation (i.e. less cooling) is evident at 7:00 UTC in observations (Figure 12). As reviewed earlier, fog can become optically thick in the infrared. When it becomes mature the infrared cooling at the surface can become negligible, or even warming can occur (Price 2011). For example, fog in MYNN_WDM6 formed roughly at 4:00 UTC, which coincided with the decrease in surface radiative cooling. The modeled fog is a radiation fog, building upwards from the ground at formation time. The fog also dissipates from

the ground upwards as shortwave radiation heating occurs after sunrise. While late compared to observations, the model achieves saturation relatively early compared to at other stations in the area.

During the fog period, the WSM6 produces a stronger cold bias than the WDM6 schemes (Figure 12). Prior to fog formation, all model runs have a positive temperature bias and a dry relative humidity. The 30-minute averaged friction velocity remains comparable to observations throughout most of the event. The warm bias in the models preceding the fog event led to a dry bias in relative humidity, delaying saturation and thus fog at the surface. As with the time-height cross section over KMSP, the model runs using the WDM6 scheme produced fog with higher liquid water content than the model runs utilizing the WSM6 scheme. After dissipation, the WDM6 model runs had a stronger cold bias than WSM6 runs, alongside having a lower (in magnitude) dry bias in relative humidity. The fog and clouds in the WDM6 schemes were more optically thick; the incoming shortwave radiation at the surface for WDM6 model runs was less than the radiation received with WSM6 model runs.

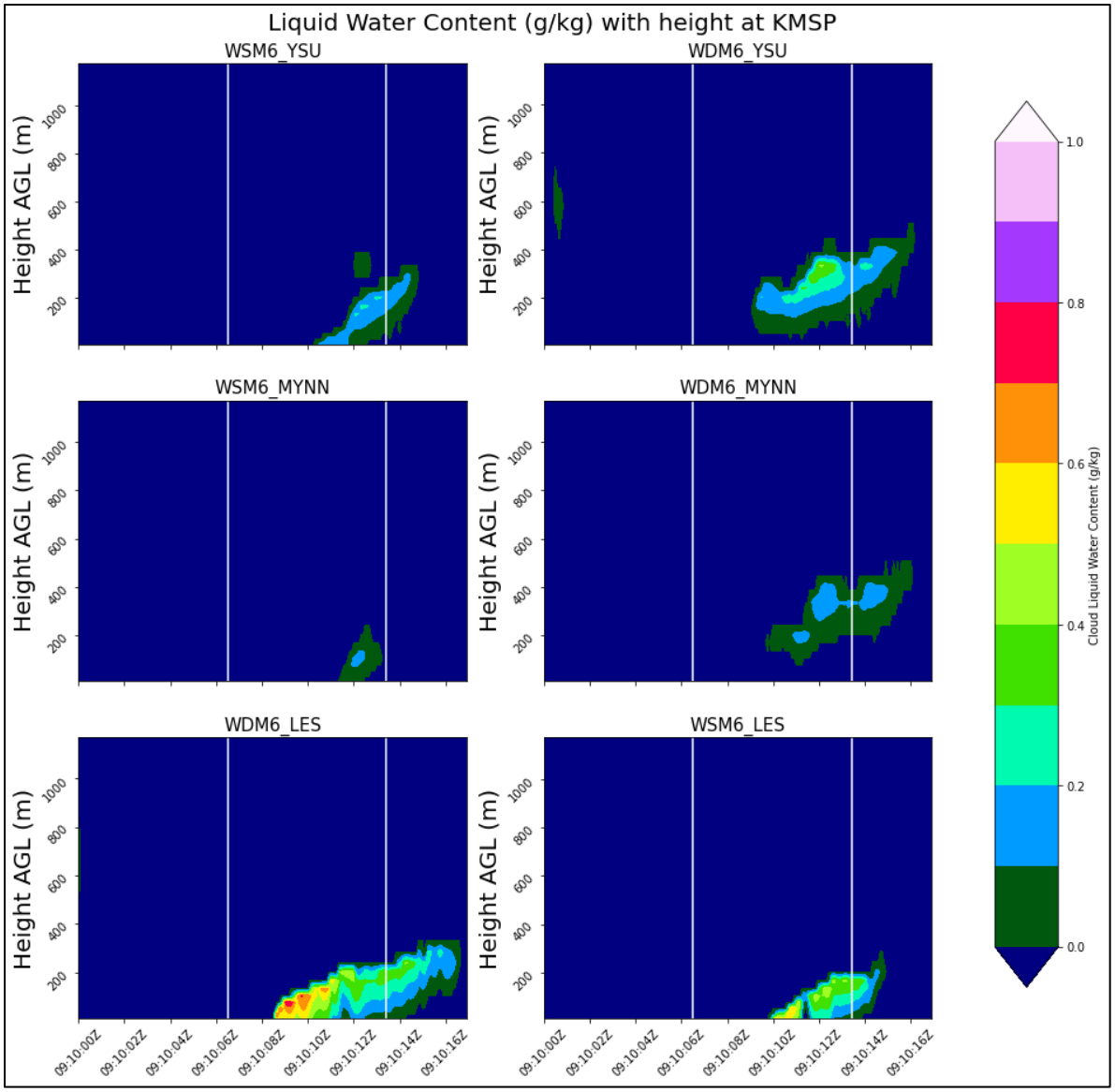

Figure 10: Time height cross sections of cloud water mixing ratio from the WRF model.

White bars represent formation and dissipation time of the fog as observed at KMSP

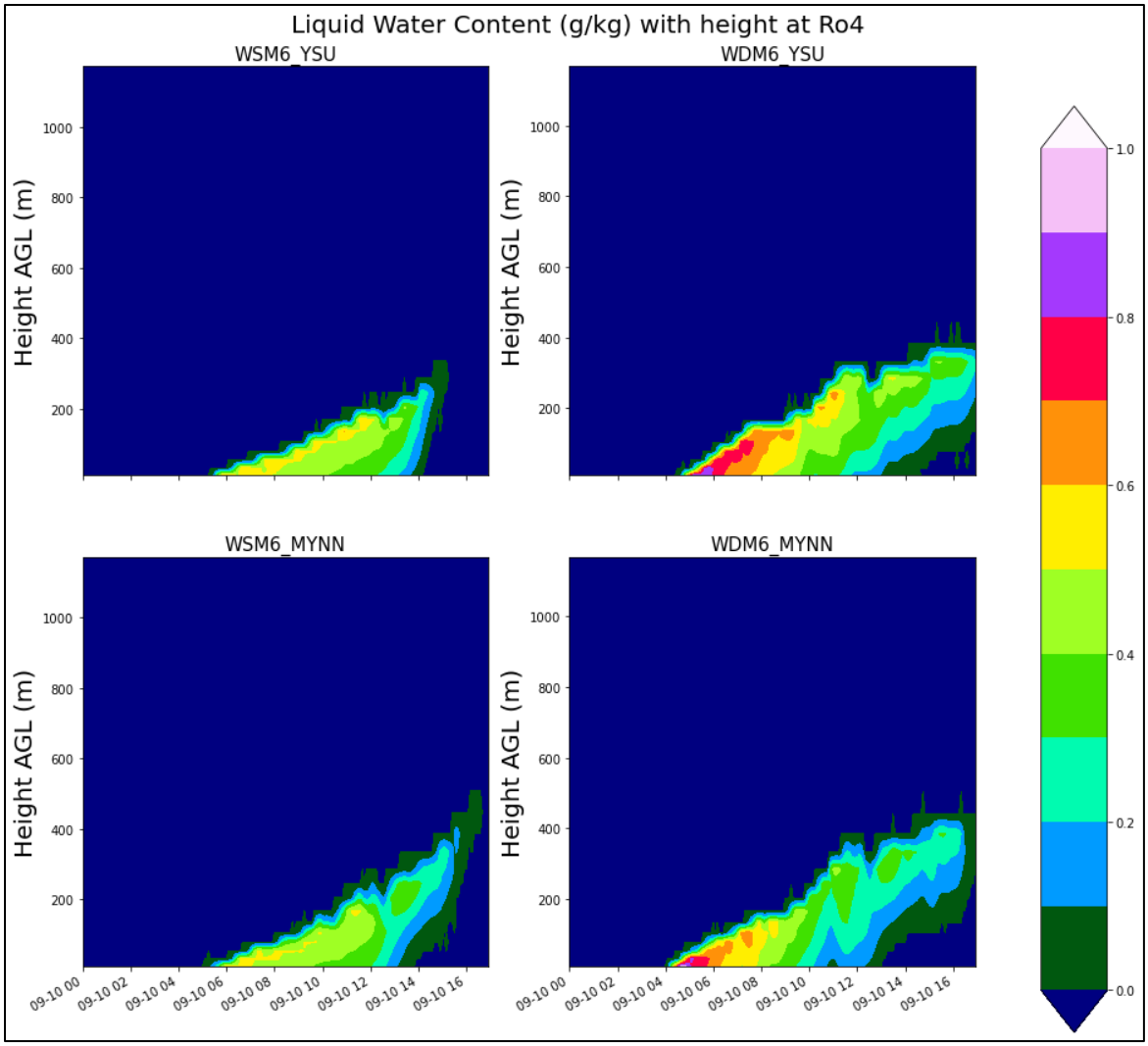

Figure 11: Cloud Liquid Water Content time-height cross sections at Ro4 from the WRF model.

No visibility measurements were made at this location, so no formation and dissipation times are available for this location

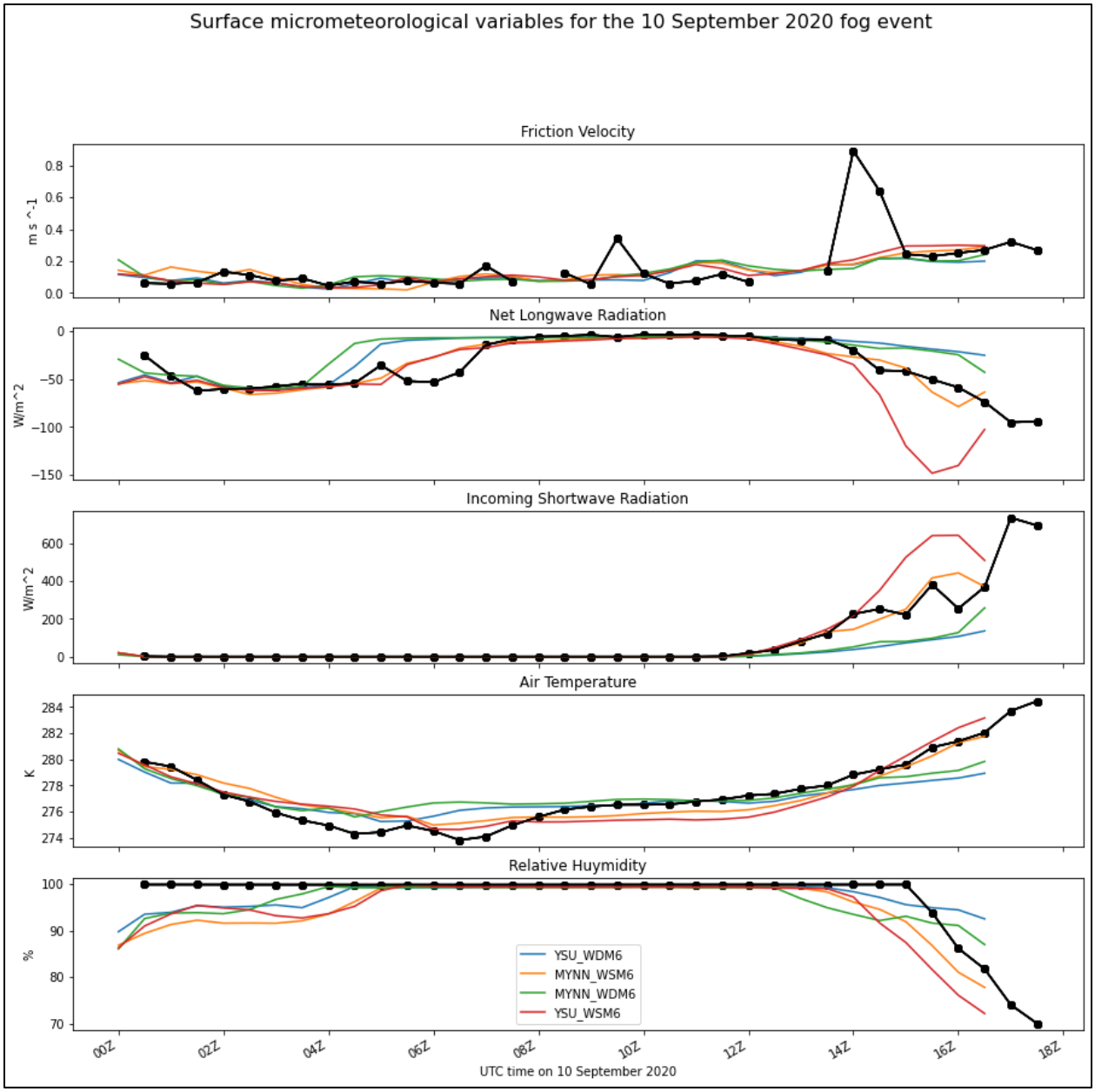

Figure 12: Surface Meteorological Parameters at Ro-4. Black dots are observations.

Role of Droplet Settling

The impact of droplet settling was examined for the WDM6_MYNN model run. The parameterization utilized grav_settling = 1 in the WRF namelist, which assumes that droplets settle due to gravity with a velocity described by Stokes' (Skamarock et al. 2019; Duynkerke 1991). Cloud droplet settling schemes are a sink of cloud water, which can become unrealistically large

otherwise. In the case of WDM6-MYNN, the cloud droplet settling scheme worsens the performance of the visibility forecasts for every station, as demonstrated through comparison with fog formation and dissipation times (Table 13). The impact of the droplet settling on cloud water content is illustrated in Figure 13 where cloud water content is significantly reduced. The observed fog formation and dissipation times are provided in Table 7.

Table 13: Formation and Dissipation time with droplet settling activated.

Station	Modeled Form/Diss Time	Station	Modeled Form/Diss Time
KANE	Formation: 08:20 Dissipation: 12:05	KSGS	Formation: 07:55 Dissipation: 08:25
KFCM	Formation: 07:35 Dissipation: 13:05	KSTP	Formation: None Dissipation: None
KMIC	Formation: None Dissipation: None	MN088	Formation: None Dissipation: None
KMSP	Formation: None Dissipation: None		

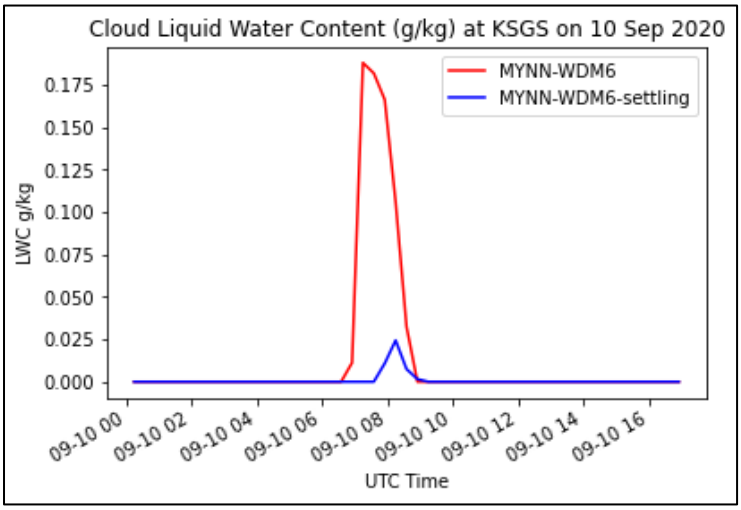

Figure 13: Liquid water content at KSGS with droplet settling, using the SW1999 scheme.

Visibility Metrics for Double Moment Schemes and the Multi-Rule Diagnostic

As an alternative method of calculating visibility, the method of Gultepe et al. (2006) is used. This method considers both droplet number concentration and mass mixing ratio of hydrometeor species. Formation and dissipation times using this method are shown in the Table 14. The values provided for the droplet number concentration for the WDM6 schemes are unphysical. The maximum values for cloud water droplet number concentration on the first model level exceeds 30,000 cm^{-3}. Contrasted with the WDM6 scheme, the highest droplet number concentration predicted by the Milbrandt-Yau scheme (mp_physics = 9) in the domain is approximately 500 cm^{3}. The formation and dissipation times are largely the same, but at times are slightly offset by 5-10 minutes. Due to WRF's tendency to predict LWC values that are too large, the SW1999 and Gultepe et al. (2006) parameterizations are used to diagnose fog in this study, rather than to determine fog intensity.

As an alternative, the multi-rule framework of Zhou and Du (2010) is applied. Here, the presence of fog is diagnosed through the 2 m relative humidity, 10 m wind speed, and cloud liquid water content fields. In this study, the visibility threshold produced by SW1999 is used instead of using the cloud liquid water content directly. To highlight the impacts of the surface meteorological fields, the rules for cloud bases/heights are not used. Fog is diagnosed with this scheme if (visibility at the lowest model level from SW1999) < 1 km OR (2 m RH > 90% AND 10 m Wind Speed < 2 m s^{-1}). The formation and dissipation times (Table 15) produced by this scheme are overall earlier and later, respectively, than those produced using visibility alone. While this multi-rule method ameliorates the early dissipation that occurs when using visibility alone, it also has many false alarms since the model relative humidity remains higher than observed relative humidity at many stations later in the day. Also, the formation time is still delayed due to the warm

biases in the model. The strongest warm biases are at KANE and KMIC, which explains their late fog formation times for both methods.

Table 14: Formation and Dissipation times of fog using the Gultepe (2006) visibility parameterization. Dissipation times with None indicate that the fog never formed in the model, or that the fog failed to dissipate by the end of the simulation.

	WDM6_YSU	**WDM6_LES**	**WDM6_MYNN**	**Milbrandt_MYNN**
KANE	Formation: 09:50 Dissipation: 12:05	Formation: 04:35 Dissipation: 16:55	Formation: 06:55 Dissipation: 13:40	Formation: 11:10 Dissipation: 12:45
KFCM	Formation: 06:05 Dissipation: 13:55	Formation: 07:45 Dissipation: 16:00	Formation: 06:20 Dissipation: 13:50	Formation: 09:45 Dissipation: 14:50
KMIC	Formation: 10:15 Dissipation: 10:35	Formation: 07:55 Dissipation: 16:55	Formation: 11:20 Dissipation: 13:20	Formation: None Dissipation: None
KMSP	Formation: None, Dissipation: None	Formation: 08:35 Dissipation: 13:45	Formation: None, Dissipation: None	Formation: 10:40 Dissipation: 12:00
KSGS	Formation: 06:15 Dissipation: 11:55	Formation: 05:45 Dissipation: 11:55	Formation: 06:55 Dissipation: 08:40	Formation: 07:40 Dissipation: 10:10
KSTP	Formation: 07:15 Dissipation: 09:50	Formation: 05:40 Dissipation: 11:15	Formation: 07:35 Dissipation: 10:05	Formation: 07:40 Dissipation: 09:55
MN088	Formation: 08:20 Dissipation: 09:10	Formation: 05:00 Dissipation: 4:05	Formation: 08:25 Dissipation: 9:20	Formation: None, Dissipation: None

Table 15: Formation and Dissipation times for a multi-rule fog method.

	WSM6 MYNN	**WDM6 YSU**	**WDM6 LES**	**WDM6 MYNN**	**WSM6 LES**	**WSM6 YSU**	**WSM6 3dtke**
KANE	Form:9:10 Diss: 13:50	Form:9:30 Diss: 15:55	Form:02:20 Diss: 16:55	Form: 06:00 Diss: 15:10	Form: 04:35 Diss: 15:00	Form: 10:55 Diss: 13:45	Form: 07:35 Diss 14:25
KFCM	Form:05:15 Diss:15:00	Form:2:50 Diss:15:05	Form: 03:35 Diss: 16:50	Form: 04:10 Diss: 15:00	Form: 06:55 Diss: 14:45	Form: 04:15 Diss: 15:05	Form: 06:05 Diss: 15:05
KMIC	Form:11:30 Diss: 12:05	Form:09:25 Diss:15:00	Form: 03:15 Diss: 16:55	Form: 09:00 Diss: 14:40	Form: 05:25 Diss: 10:35	Form: 11:25 Diss: 13:50	Form: 08:40 Diss: 13:10
KMSP	Form:09:55 Diss: 13:55	Form:06:25 Diss:14:20	Form: 02:45 Diss: 16:20	Form: 09:25 Diss: 13:30	Form: 03:25 Diss: 14:30	Form: 09:45 Diss: 14:30	Form: 05:15 Diss: 14:30
KSGS	Form:07:25 Diss:14:25	Form 05:40 Diss: 15:15	Form: 05:25 Diss: 14:05	Form: 06:30 Diss: 13:50	Form: 06:00 Diss: 14:00	Form: 06:10 Diss: 14:15	Form: 05:40 Diss: 13:30
KSTP	Form:08:25 Diss:14:25	Form:07:15 Diss:15:20	Form: 05:20 Diss: 14:35	Form: 07:35 Diss: 13:45	Form: 08:00 Diss: 14:05	Form: 08:25 Diss: 15:20	Form: 06:25 Diss: 13:30
MN088	Form:08:40 Diss: 13:45	Form:08:20 Diss: 14:05	Form: 01:05 Diss: 15:30	Form: 07:45 Diss: 13:55	Form: 04:15 Diss: 14:55	Form: 08:45 Diss: 14:00	Form: 04:15 Diss: 14:20

Spatial Analysis

GOES and MODIS data are used to determine the spatial distribution of the fog. As the fog mainly occurred during the night, the Nighttime Microphysics RGB product and the traditional 10.3 μm - 3.9 μm brightness temperature difference (BTD) methods are used. While more advanced metrics are available (Cermak and Bendix 2008), they are not a focus of this study. A GOES daytime image is also presented; this image is shortly after fog had dissipated at every station in the innermost domain. Satellite imagery are compared with liquid water content at the lowest model level (Figure 14,15,16). A positive brightness temperature difference is produced by the presence of fog and low clouds. Negative values in brightness temperature are clipped to zero, and often are produced by high cirrus clouds. In the nighttime microphysics product, the cyan to yellow colors represent the presence of low clouds. In the Nighttime Microphysics RGB product, ice clouds and cirrus are represented by deep red hues and deep red hues speckled with yellow pixels. The BTD method struggles during the daytime owing to more 3.9 μm radiation from the sun during the daytime. The Nighttime Microphysics RGB method uses the BTD for its green channel.

The spatial distribution of clouds in the Minneapolis case is complex. There is a mix of high, mid, and low-level clouds (Figure 14). At 4:35Z on 10 September, the MODIS-Terra nighttime microphysics and BTD products do not show the presence of a strong fog signature (Figure 17). Positive BTD values signify the presence of low-level clouds (including the possibility of fog) during the nighttime hours (Figure 14b, 15c, 18a). Cirrus and high clouds are also present during the event, especially over the southern periphery of the mesoscale domain (Figure 14b) and over almost the entirety of the innermost domain. In daytime imagery high/cirrus clouds are apparent via the red hues in the Daytime Microphysics RGB product (Figure 15a, 19a). Low clouds are also present over the Minneapolis Metropolitan area in the daytime satellite images. At the time of the daytime imagery fog had already dissipated at every visibility recording station in the

innermost domain. As stated previously fog appeared late in the model at every station in the innermost domain. The modeled fog started along the periphery of the Minneapolis metro and eventually propagated inward towards the center of the city. The WDM6 runs had much higher LWC than the WSM6 runs (Figure 16, 20, 21). The LES_WDM6 run had a much higher liquid water content distributed over a larger area of the innermost domain as compared to the other model solutions. While all models did produce fog on the east side of the innermost domain of interest at 05:55 UTC, they struggled to produce fog elsewhere. The modeled precipitation field is underestimated for the southern half of the domain for all model run and overestimated in the northern half of the domain (Figure 22, Table 16). Despite KANE receiving higher than observed precipitation in the model runs, the model was still not able to form fog due to the higher than observed temperature bias, as it had a dry bias in relative humidity. The HRRR assimilates radar data every 15 minutes (Dowell et al. 2022) during the model spin-up period. As the HRRR was used for the initial and boundary conditions in this study, it is possible that initializing the model later would have improved the placement/amount of precipitation and thus the fog formation periods.

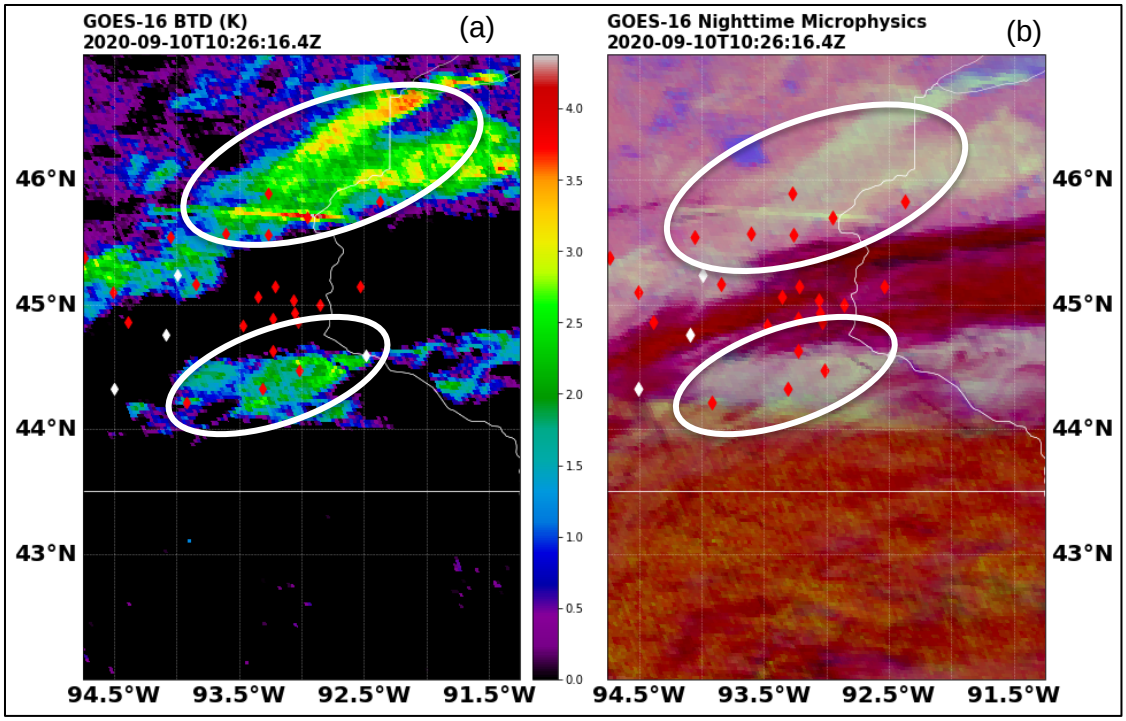

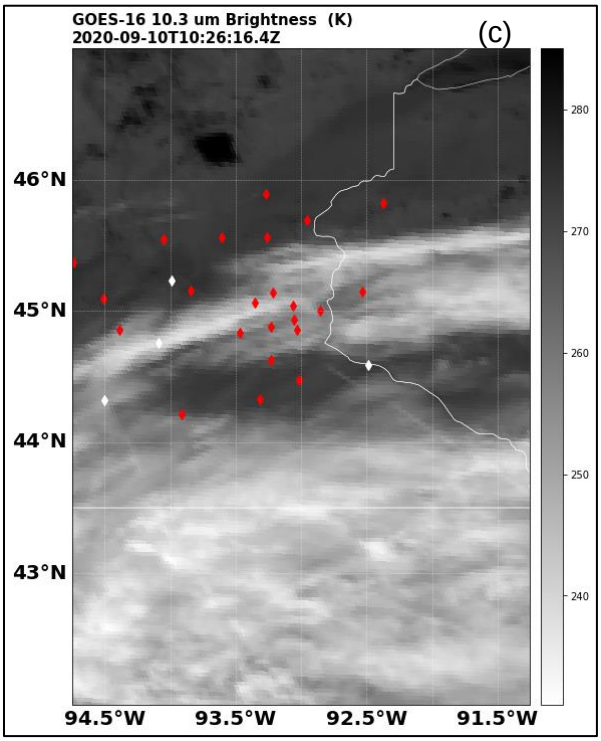

Figure 14(a-c): GOES-16 imagery at 10:27 UTC. Red dots indicate that fog was observed at the surface at the closest observation time to the satellite image for that location. White dots indicate that no fog was observed at the surface. Areas within the ellipse indicate the possible presence of low clouds and fog.

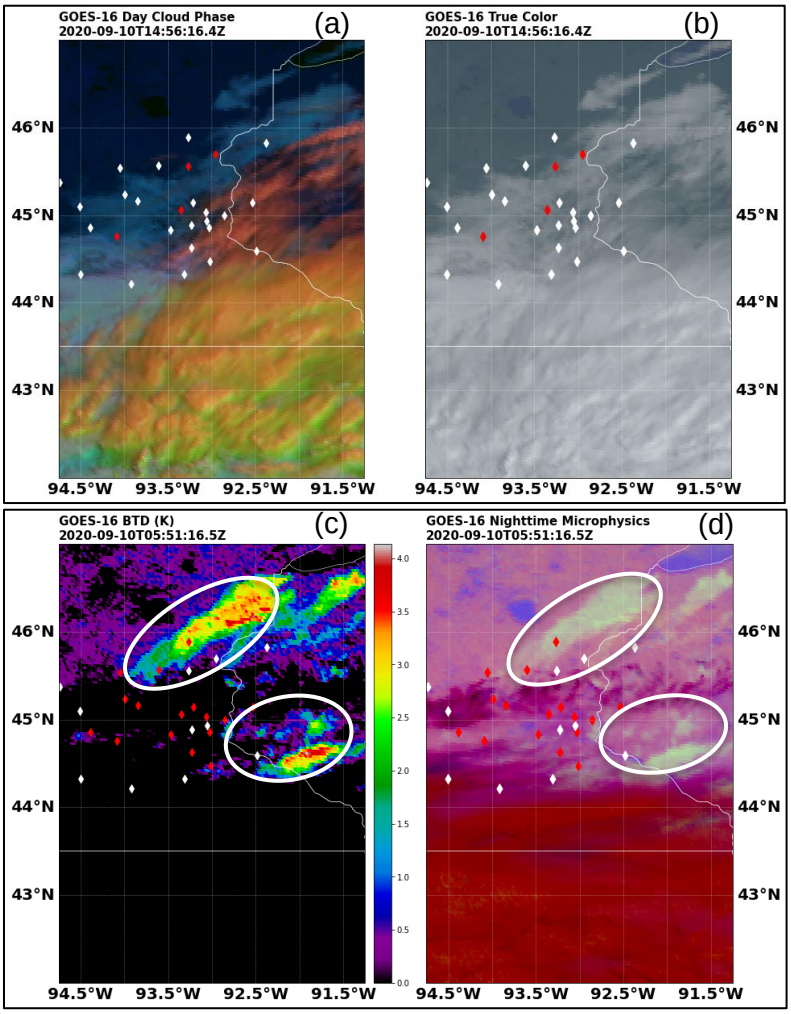

Figure 15(a-d): GOES-16 imagery at 14:56 UTC and 5:51 UTC. Dots represent stations within the mesoscale domain. Red dots indicate that fog was observed at the surface at the closest observation time to the satellite image for that location. White dots indicate that no fog was observed at the surface. Areas within the ellipse indicate the possible presence of low clouds and fog.

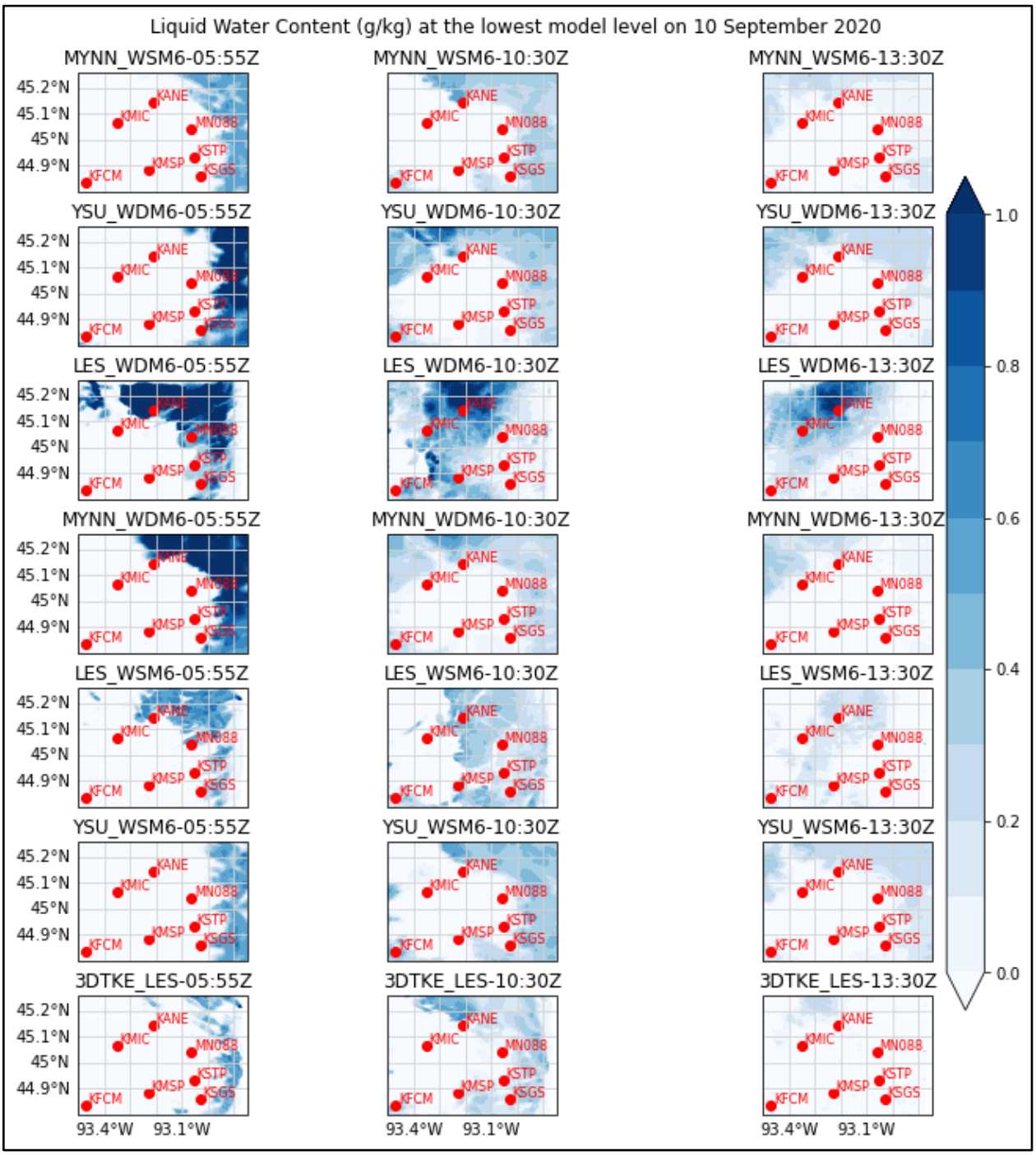

Figure 16: Modeled Cloud Liquid water content at the first mass model level around the Minneapolis Metro area for various model configurations. Three different time periods of the fog event are included. Thicker fog presence is indicated through darker blue pixels. No liquid water content at the lowest model level is represented with white pixels.

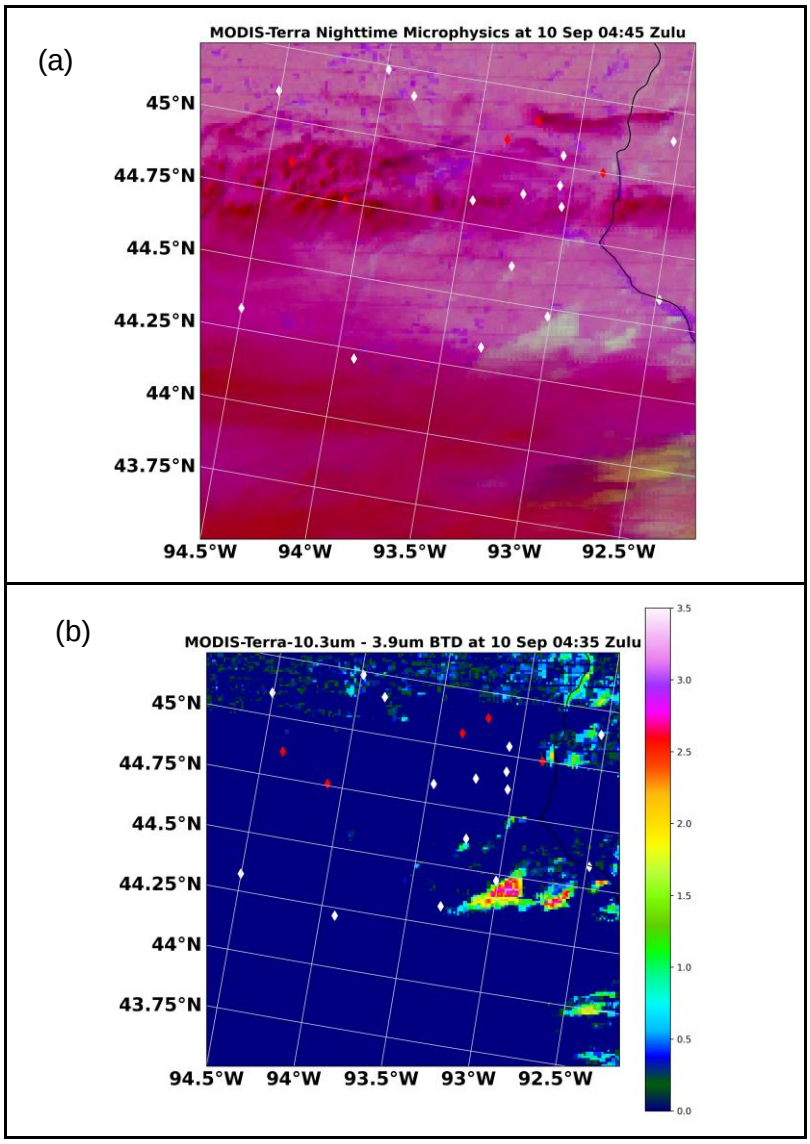

Figure 17: MODIS-TERRA nighttime microphysics and BTD products. Red dots indicate that fog was observed at the surface at the closest observation time to the satellite image for that location. White dots indicate that no fog was observed at the surface.

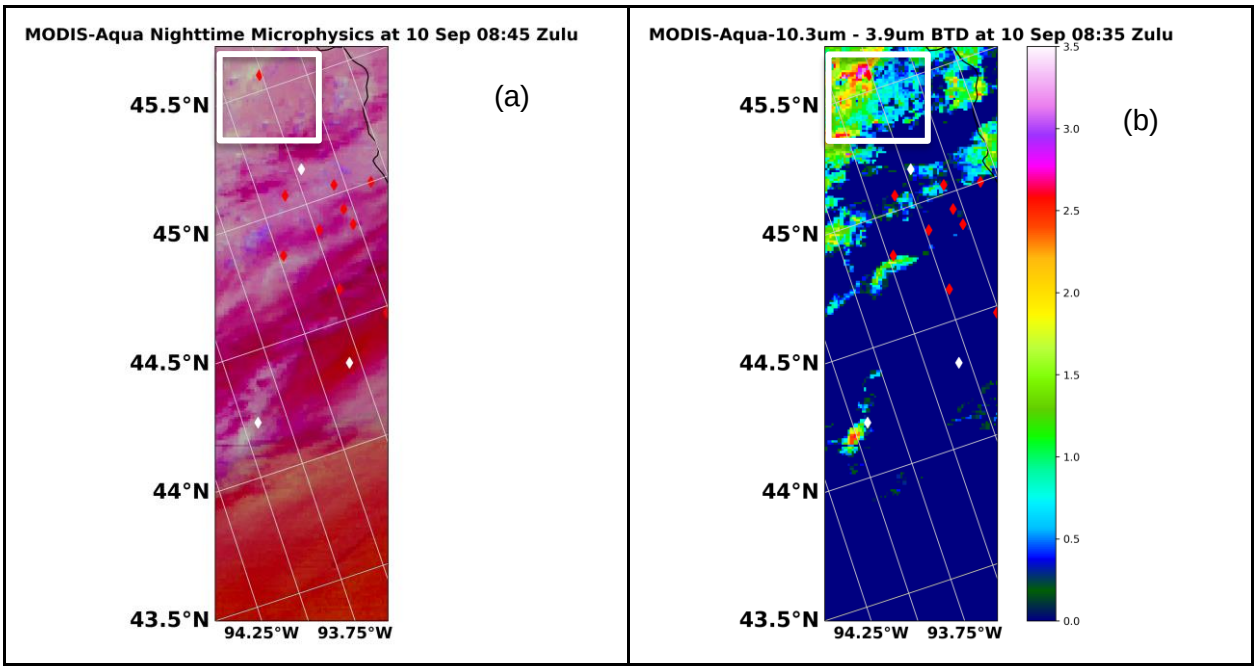

Figure 18: MODIS nighttime microphysics and BTD products from Aqua. White boxes outline areas of possible fog and low clouds.

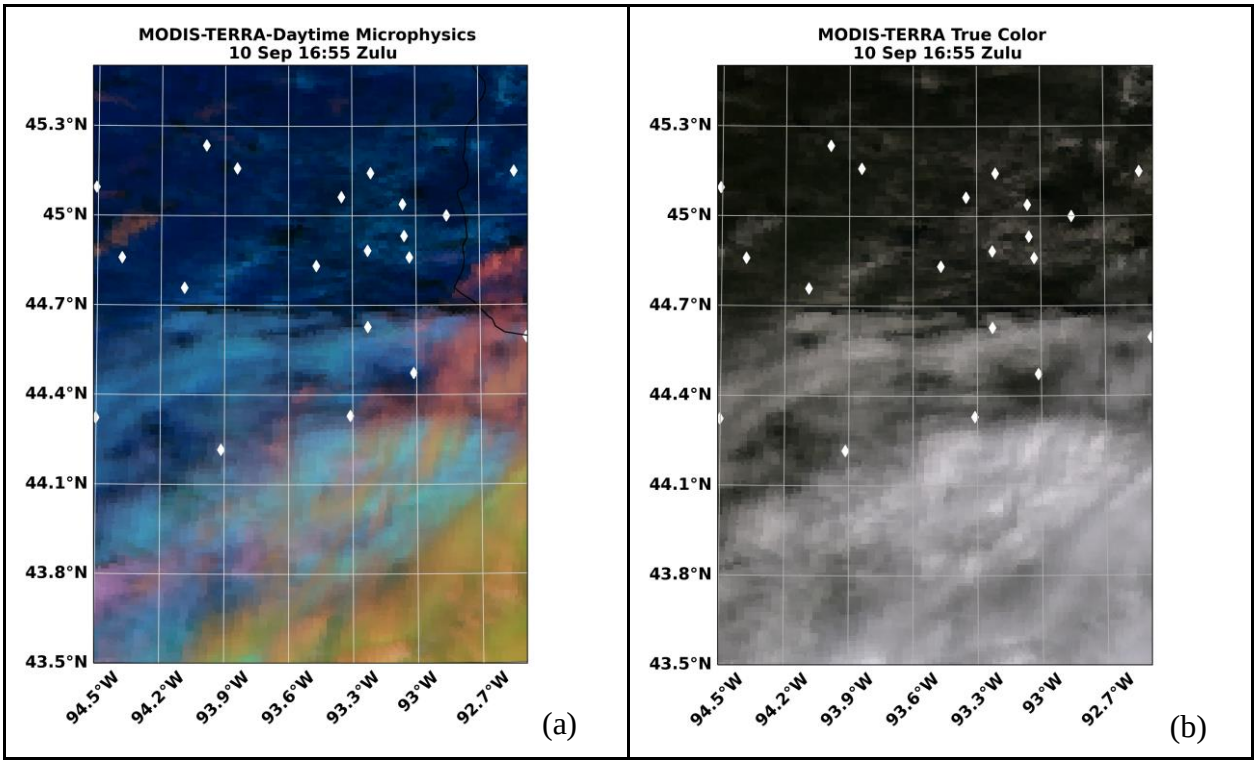

Figure 19 (a-b): MODIS Daytime Microphysics and MODIS True Color. An example of an area of low clouds is outlined in the white box White dots indicate that no fog was observed at the surface.

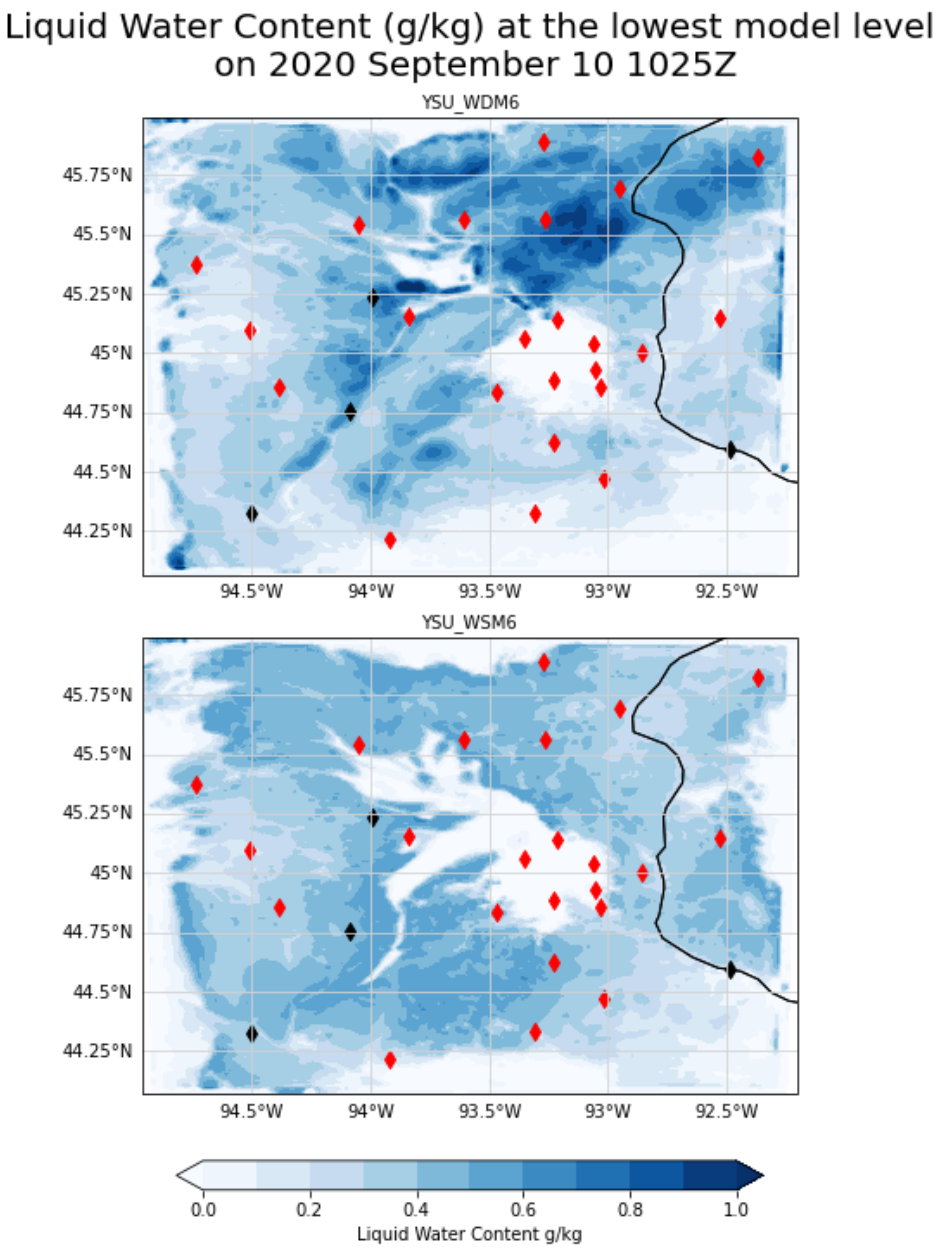

Figure 20: Cloud liquid water content at the lowest model level for YSU-WDM6 and YSU-WSM6 model runs, for the entire mesoscale domain. Red dots indicate that fog was observed at the surface at the closest observation time for that location. Black dots indicate that no fog was observed at the surface.

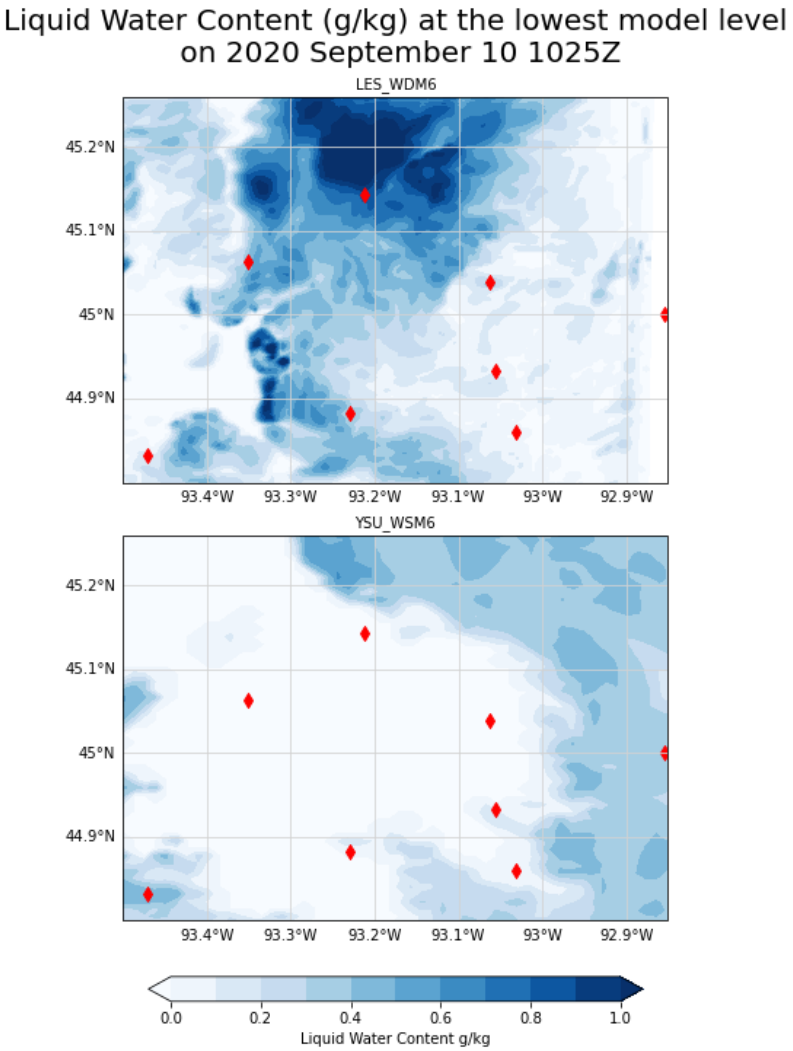

Figure 21: Cloud liquid water content at the lowest model level for YSU-WSM6 and LES-WDM6 model runs, for the entire mesoscale domain. Red dots indicate that fog was observed at the surface at the closest observation time for that location. Black dots indicate that no fog was observed at the surface.

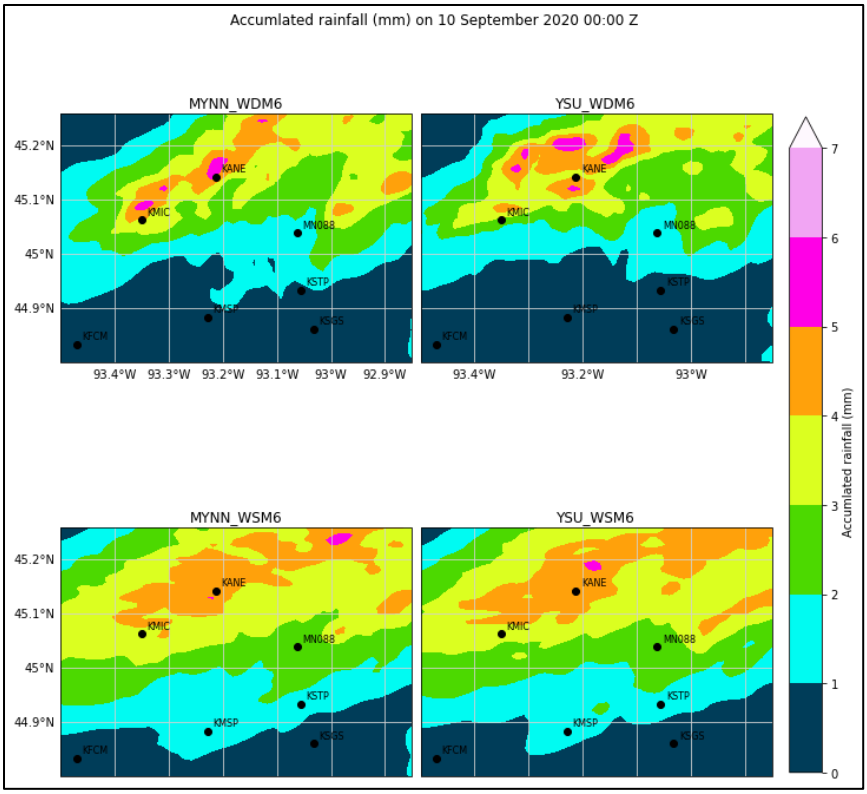

Figure 22:Accumulated Rainfall by 10 September 00:00 UTC for mesoscale domains.

Table 16: Observed 24 hr accumulated rainfall ending 00 UTC 10 September 2020.

Station	Accumulated rainfall (mm)
KFCM	3.56
KMIC	4.06
KMSP	3.56
KSGS	3.30
KSTP	3.81
KANE	Trace
MN088	Not available

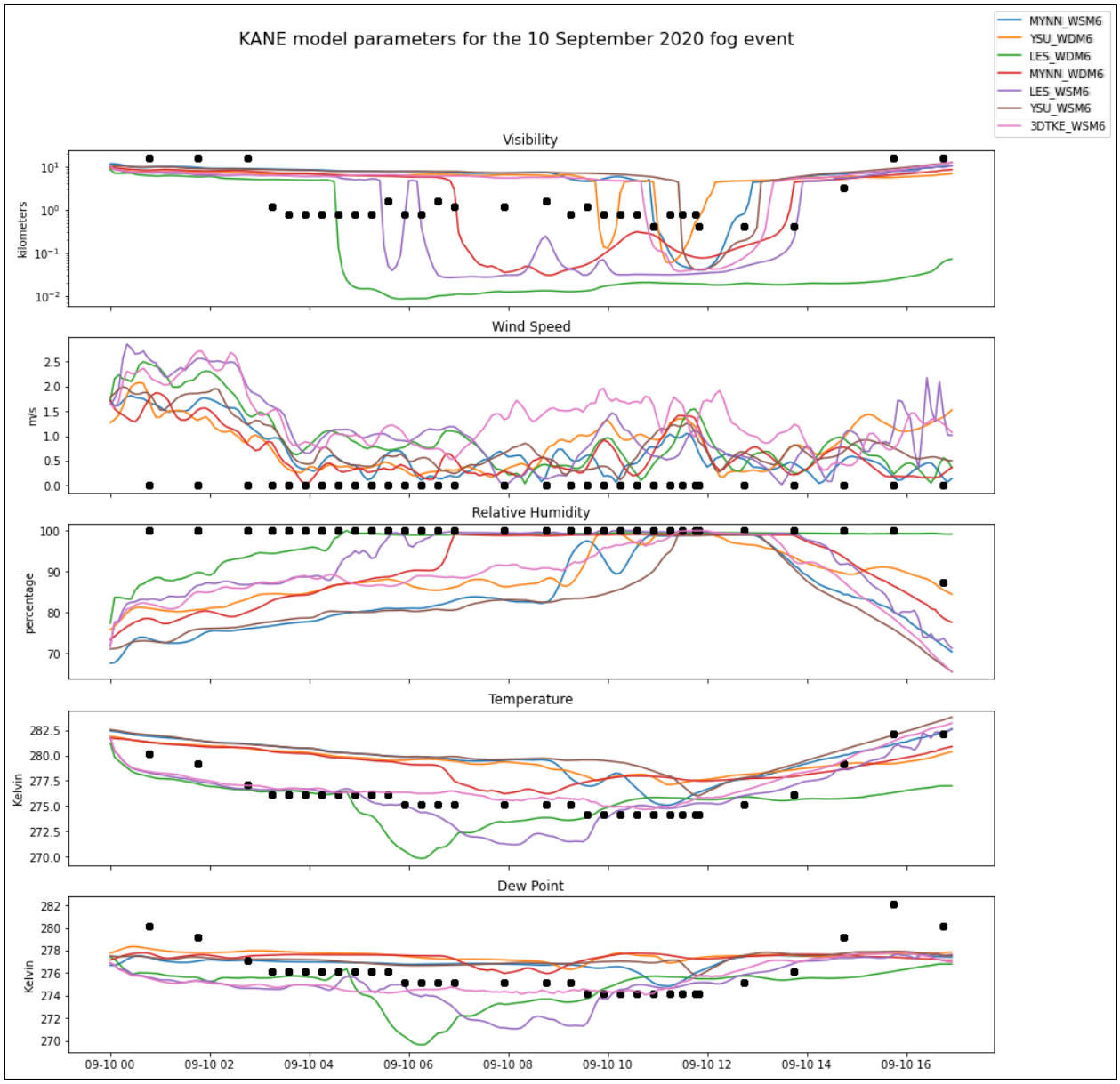

Figure 23:Surface Meteorological parameters at KANE. Black dots are observations.

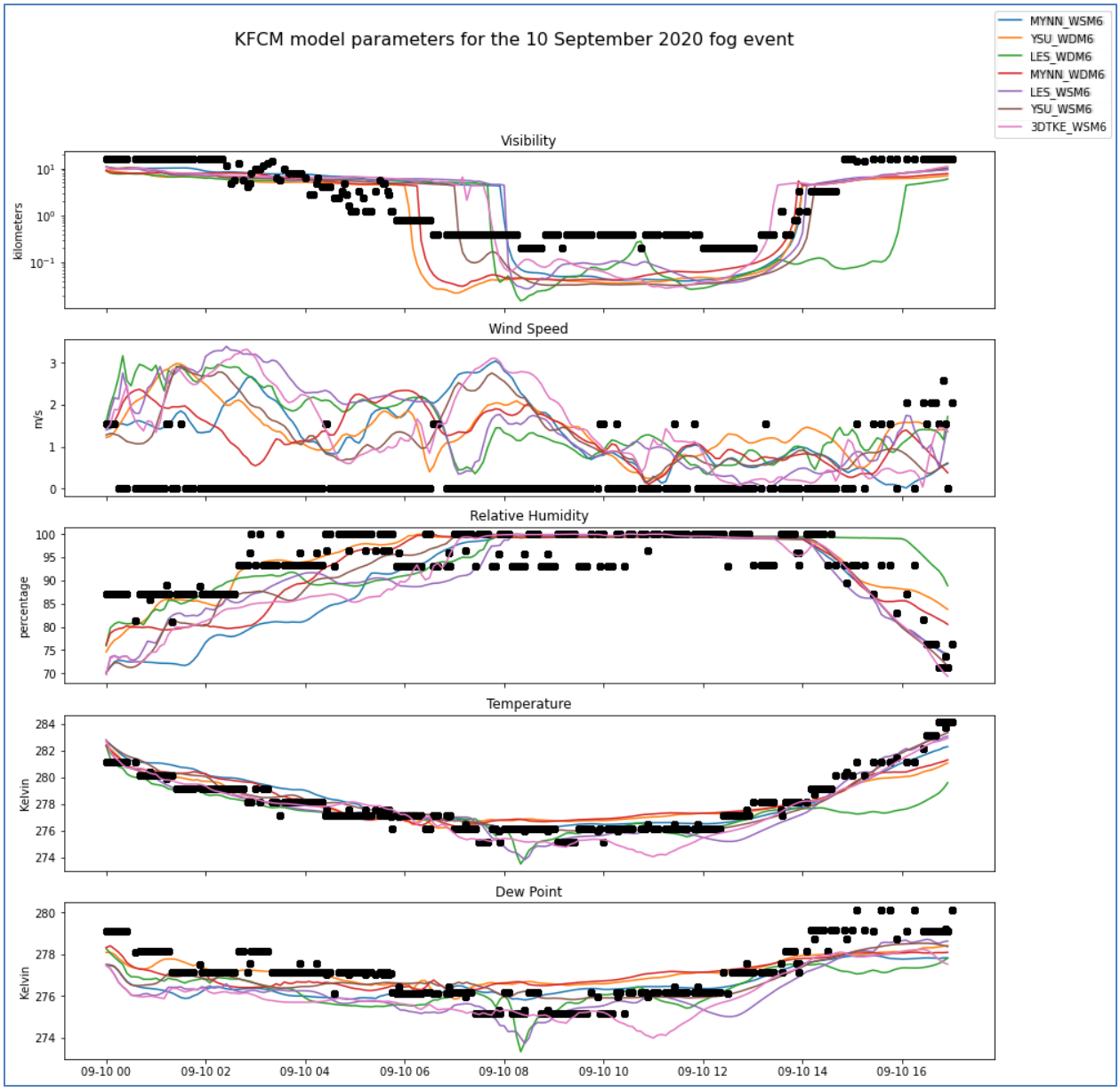

Figure 24:Surface Meteorological parameters at KFCM. Black dots are observations.

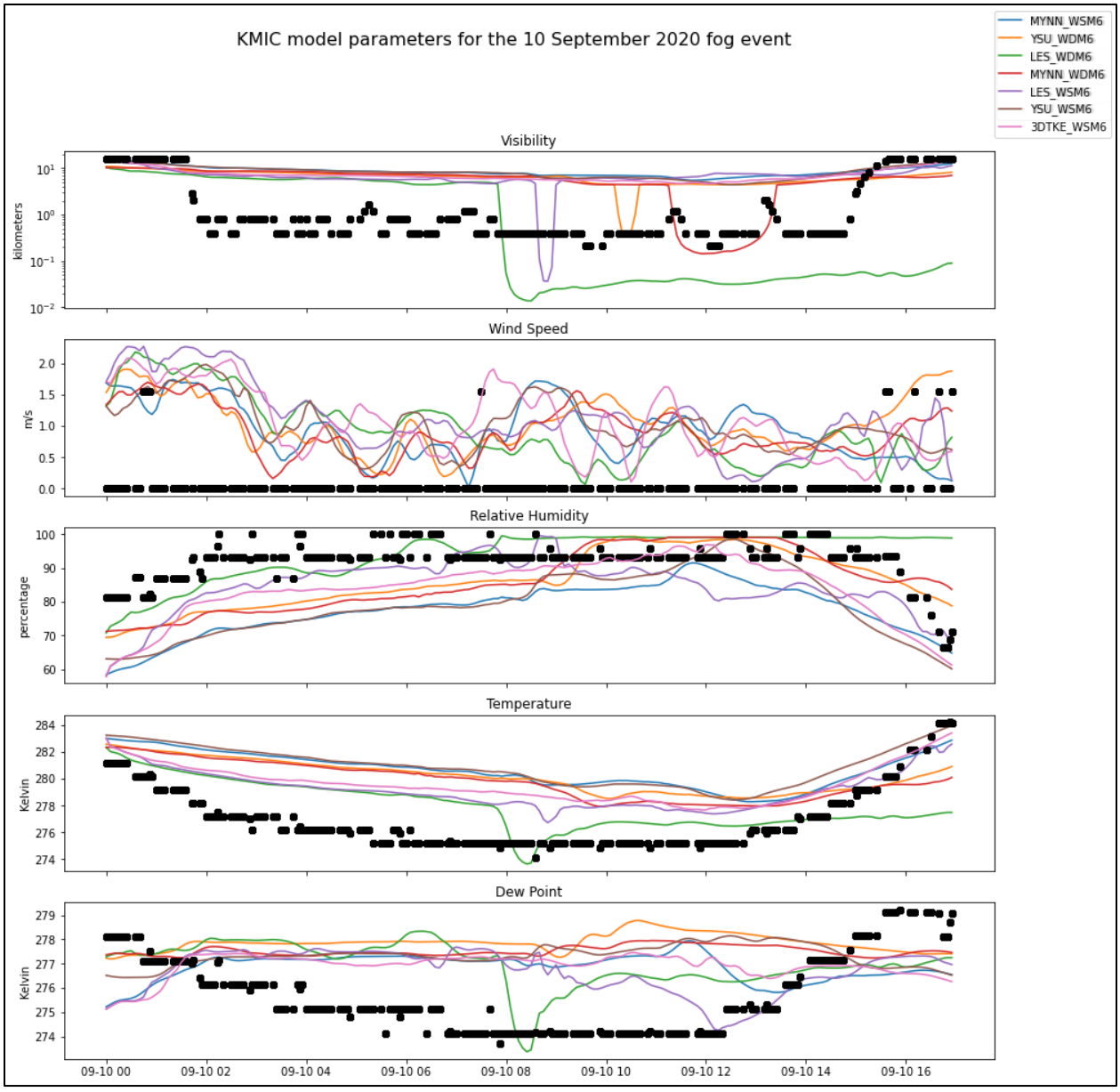

Figure 25:Surface Meteorological parameters at KMIC. Black dots are observations.

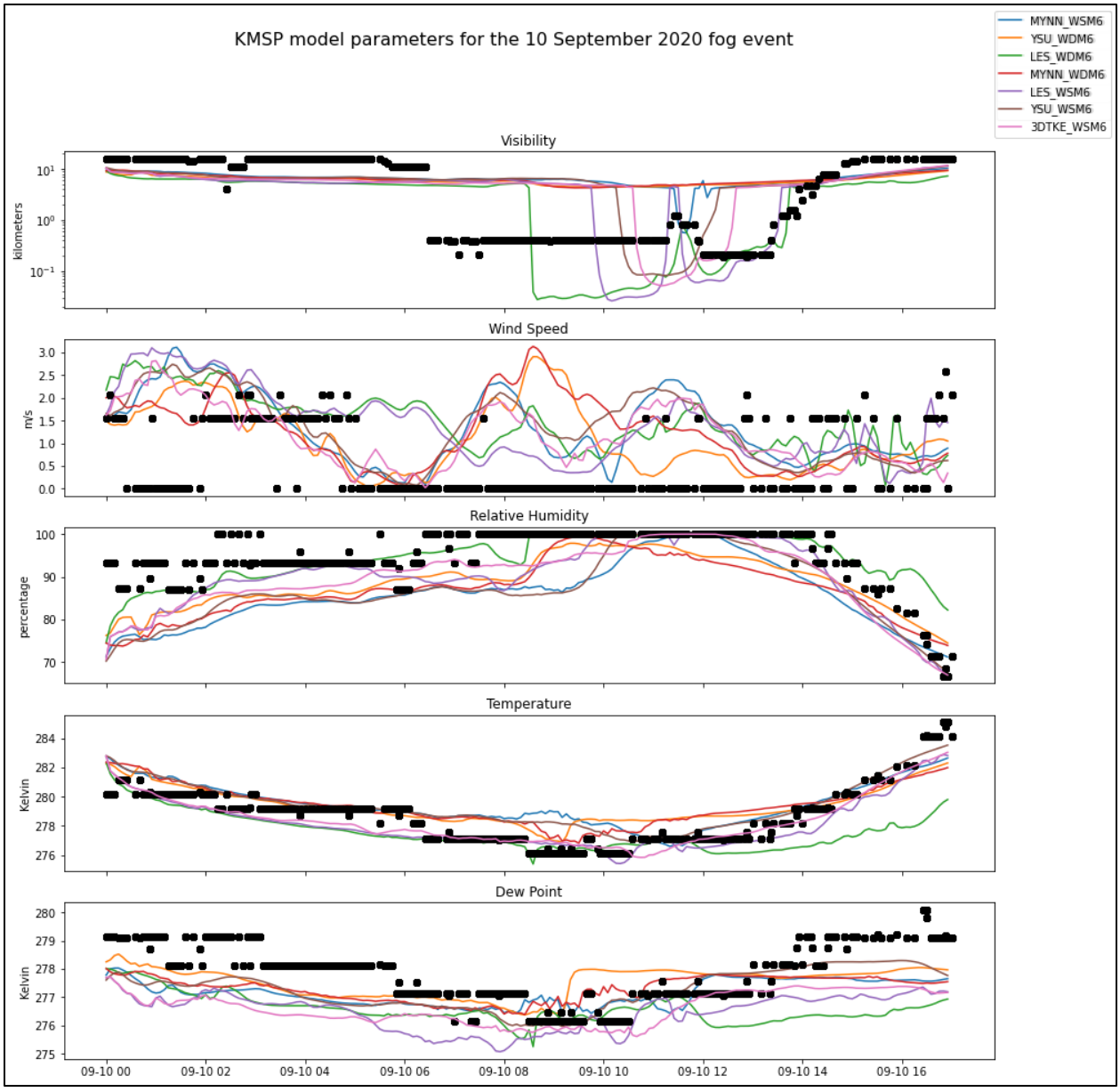

Figure 26:Surface Meteorological parameters at KMSP. Black dots are observations.

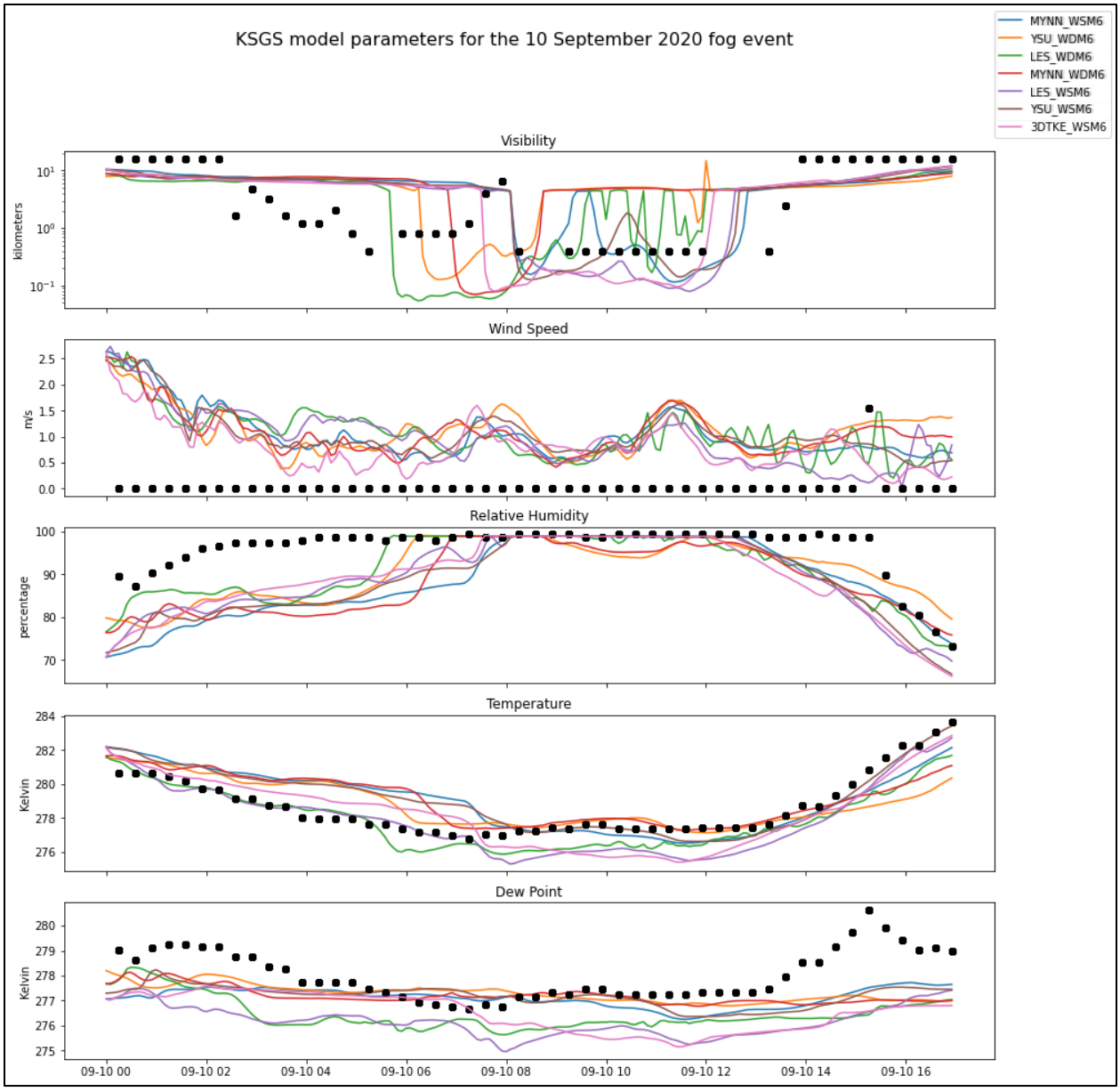

Figure 27: Surface Meteorological parameters at KSGS. Black dots are observations.

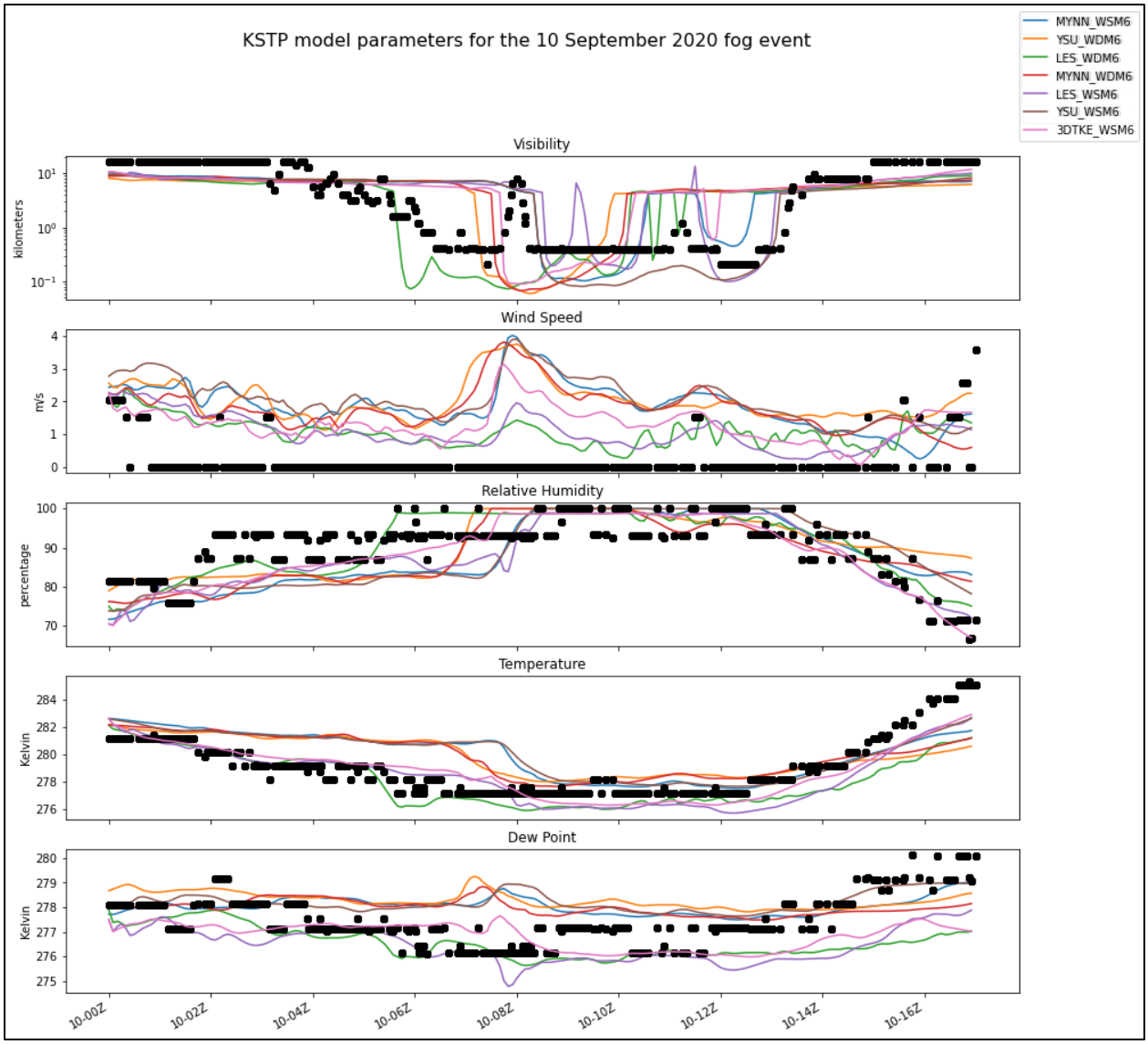

Figure 28: Surface Meteorological parameters at KSTP. Black dots are observations.

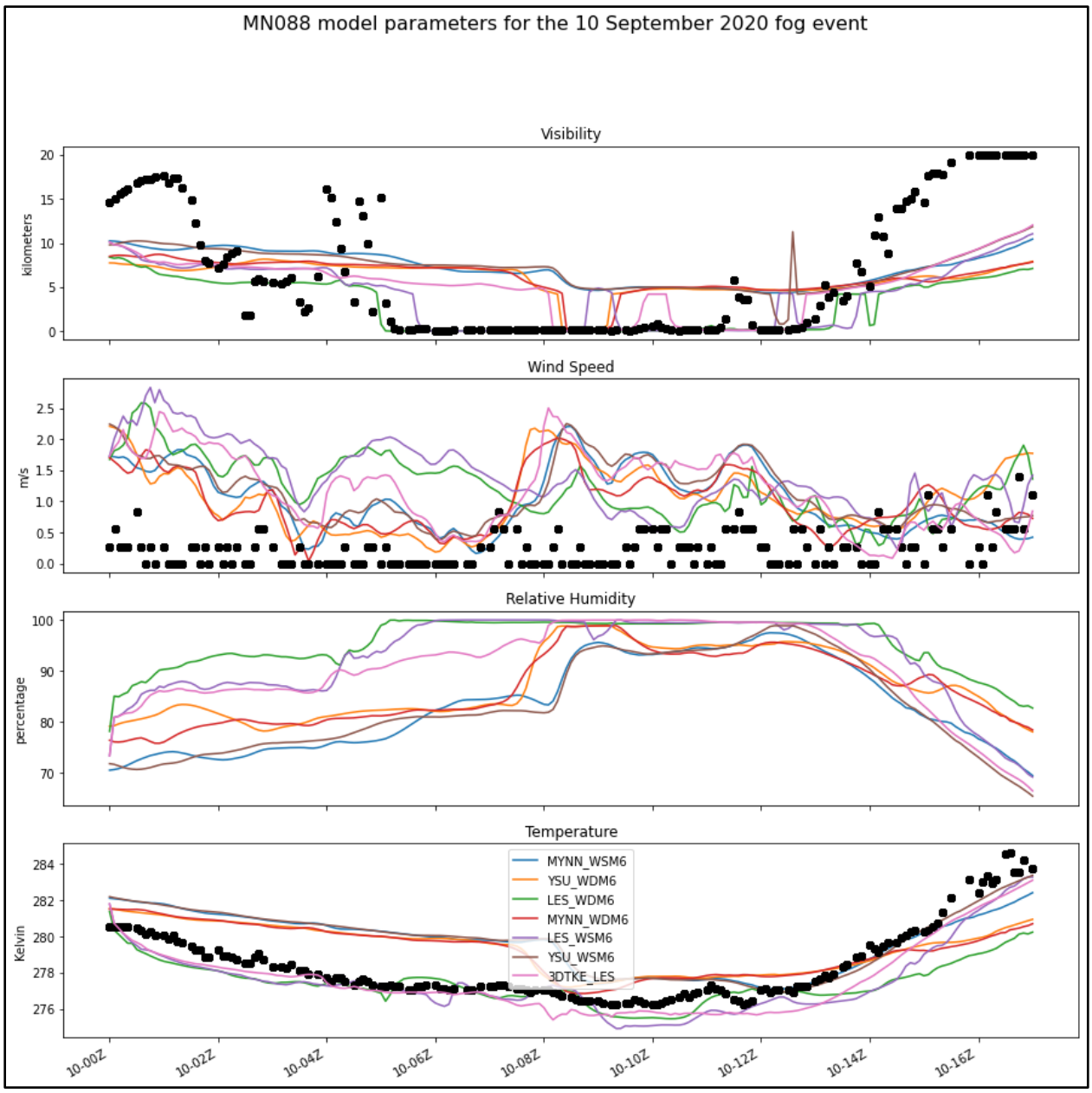

Figure 29: Surface Meteorological Parameters at MN-088. Relative humidity and pressure are not recorded at this station. RH was included for inter-model comparison. Black dots are observations.

Chapter 4 – Fog Event in North Dakota on 30 March 2020

The formation and dissipation times for the stations within the innermost domain of the Grand Forks fog case are provided in Table 17. The number of visibility sensors in this domain is limited compared to the Minneapolis case. The formation and dissipation times of the model runs are provided in Table 18. The visibility parameterization is from (Stoelinga and Warner 1999). Across all model runs the formation times are late at KGFK. Based on the 10-minute model output, fog formed between 5:30 UTC and 5:50 UTC for most model runs, except for WSM6_MYNN and WDM6_YSU, for which it formed later into the night at 6:20-6:30 UTC. The YSU_WDM6 runs formed overly persistent fog; in some model runs it failed to dissipate by the end of the simulation period. In the LES the fog had an overall tendency to dissipate early, while in the mesoscale domains the fog tended to dissipate late. If the fog failed to dissipate by the end of the simulations (23:00 UTC), the dissipation time is listed as N/A.

Performance metric values are provided in Table 19. To compare mesoscale and sub-kilometer domains, only the stations within the innermost domain were used here. As the mesoscale nests were much larger than the innermost domain, a second set of statistics is provided in Table 20; this table considers stations not falling within the bounds of the innermost domain. Among the statistics in Table 19, the LES has a lower POD and Threat Score than the parent domains. The WSM6-LES model run performed very poorly, with a near 0 Heidke Skill Score. Furthermore, the WDM6-LES performed better than its single moment counterpart. The WSM6-LES run also has a large False Alarm Ratio. The Bias score was close to 1.0 for the mesoscale domains; in the WDM6-LES and WSM6-LES domains, the Bias score was lower due to the underprediction of fog. As seen in a station meteogram (Figure 36), the LES-WSM6 model predicted fog at the wrong time—after fog had already dissipated in observations. The formation and dissipation time offsets are provided in Figures 39 and 40. When considering all stations within

the outermost domain, the POD drops and there is an increase in the number of false alarms. This is also indicated by the higher bias scores, where fog was globally overpredicted by WDM6_YSU and WDM6_MYNN.

Table 17: Observed Formation and Dissipation times (UTC) for the Grand Forks 30 March 2020 case

Station	Formation	Dissipation
KGFK	04:25:00	17:35:00
KRDR	06:01:00	16:37:00
MN060	05:05:00	16:21:00

Table 18: Modeled formation and Dissipation times (UTC) of fog at the stations in the innermost domain.

	WDM6_YSU	WDM6_LES	WDM6_MYNN	WSM6_LES	WSM6_YSU	WSM6_MYNN	LargeLES
KGFK	Form: 06:30 Diss: N/A	Form: 05:40 Diss: 14:40	Form: 05:50 Diss: 19:00	Form: 05:40 Diss: N/A	Form: 05:50 Diss: 19:00	Form: 06:20 Diss: 19:40	Form: 5:20 Diss: None
KRDR	Form: 07:50 Diss: N/A	Form: 05:20 Diss: 14:00	Form: 08:40 Diss: 20:00	Form: 05:20 Diss: 09:00	Form: 08:40 Diss: 17:30	Form: 07:50 Diss: 17:10	Form: 4:50 Diss: 15:00
MN060	Form: 08:10 Diss: N/A	Form: 08:30 Diss: 13:10	Form: 07:20 Diss: 18:20	Form: 08:30 Diss: 13:00	Form: 07:20 Diss: 16:50	Form: 08:10 Diss: 17:20	Form: 7:00 Diss: N/A

Table 19: Performance Metrics for fog detection for stations only within the innermost domain.

	POD	**Accuracy**	**FAR**	**Bias**	**Threat Score**	**HSS**
WDM6-YSU	0.84	0.62	0.42	1.45	0.52	0.24
WDM6-LES	0.53	0.72	0.15	0.62	0.48	0.44
WDM6-MYNN	0.87	0.80	0.24	1.15	0.68	0.59
WSM6-LES	0.25	0.51	0.49	0.50	0.20	0.01
WSM6-MYNN	0.87	0.84	0.18	1.06	0.73	0.67
WSM6-YSU	0.78	0.77	0.24	1.02	0.63	0.55
WSM6-LES-Large-Domain	0.69	0.71	0.28	0.95	0.54	0.43

Table 20: Performance Metrics for fog detection for stations within the outermost domain.

	POD	**Accuracy**	**FAR**	**Bias**	**Threat Score**	**HSS**
WDM6-YSU	0.55	0.80	0.47	1.04	0.37	0.41
WDM6-MYNN	0.59	0.80	0.47	1.11	0.39	0.43
WSM6-MYNN	0.55	0.84	0.36	0.86	0.42	0.48
WSM6-YSU	0.45	0.83	0.37	0.71	0.35	0.42

Table 21: Error metrics for all stations within the outmost domains.

	WDM6-YSU	**WDM6-MYNN**	**WSM6-MYNN**	**WSM6-YSU**
T2-Bias	-0.63	-0.41	0.13	0.19
T2-MAE	2.32	2.13	1.91	2.04
Td-Bias	-0.23	-0.09	0.06	0.23
Td-MAE	1.97	1.81	1.83	2.00
WS_Bias	0.33	0.42	0.53	0.52
WS_MAE	1.22	1.21	1.19	1.18
RH-Bias	3.41	2.49	-0.38	-0.26
RH-MAE	10.87	10.26	10.60	10.89

Table 22: Performance Metrics for stations within the innermost domain.

	WDM6-YSU	**WDM6-LES**	**WDM6-MYNN**	**WSM6-LES**	**WSM6-MYNN**	**WSM6-YSU**	**WSM6-LES-Large**
T2-Bias	-2.53	-2.21	-1.77	-1.38	-1.32	-1.39	-1.71
T2-MAE	2.99	2.57	2.40	2.09	1.90	1.88	2.29
Td-Bias	-2.13	-1.55	-1.13	0.35	-0.03	0.42	0.15
Td-MAE	2.49	1.94	1.99	2.40	2.03	2.56	2.39
WS_Bias	0.24	1.07	1.07	1.31	0.43	0.28	1.16
WS_MAE	1.10	1.19	1.17	1.38	1.14	1.09	1.27
RH-Bias	13.14	10.41	10.99	9.29	9.38	10.93	10.02
RH-MAE	15.28	13.24	13.84	12.51	12.67	13.25	13.13

Within the innermost domain, a cold bias and moist bias (in relative humidity) are present across all model runs, as shown in Table 22 Similarly, this cold/moist bias exists for the WDM6-YSU/WDM6-MYNN model runs for the outermost domain (Table 21). Across the three WDM6 model runs dew point temperatures were too low. As with the Minneapolis case, wind speeds were biased high, with the LES domains having the most prominent biases. The three WSM6 runs have smaller 2 m temperature biases (in magnitude) than the WDM6 runs and substantially smaller dew point biases (in magnitude). Within the innermost domain, relative humidity has a strong positive bias, where the fog remained overly persistent and often failed to dissipate by the end of the model run. These moist and cool biases drastically diminish when considering all stations in the outermost domain.

Vertical Profiles of Cloud Liquid Water Content

The time-height cross section of cloud liquid water content over KGFK illustrates the vertical structure of fog development (Figure 30). No vertical measurements of conditions were available, so only inter-simulation comparisons are possible. Like with the Minneapolis case, the WDM6 model runs produce a higher cloud water content than the WSM6 runs. For the mesoscale runs the fog is limited to the first model level for the first few hours of the fog lifetime (i.e., a shallow fog) before developing into a deeper fog that spans many tens of meters. The LES domains produced a shallow fog that was limited to the first few model grid cells for a longer amount of time than the mesoscale domains. Typical liquid water mixing ratios of observed fog range from 0.01 g kg^{-1} to 0.3 g kg^{-1} (Gultepe et al. 2006, 2007).

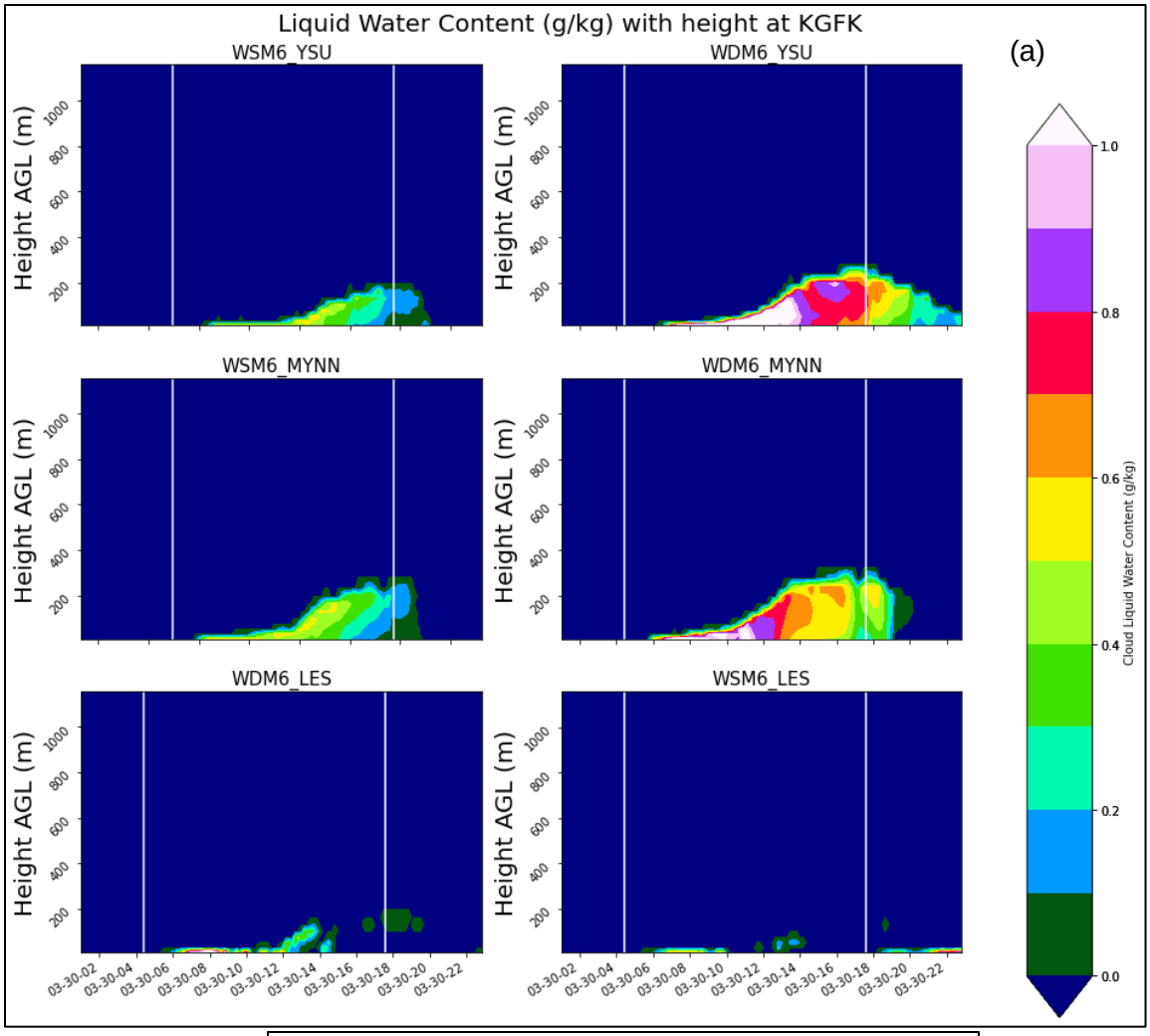

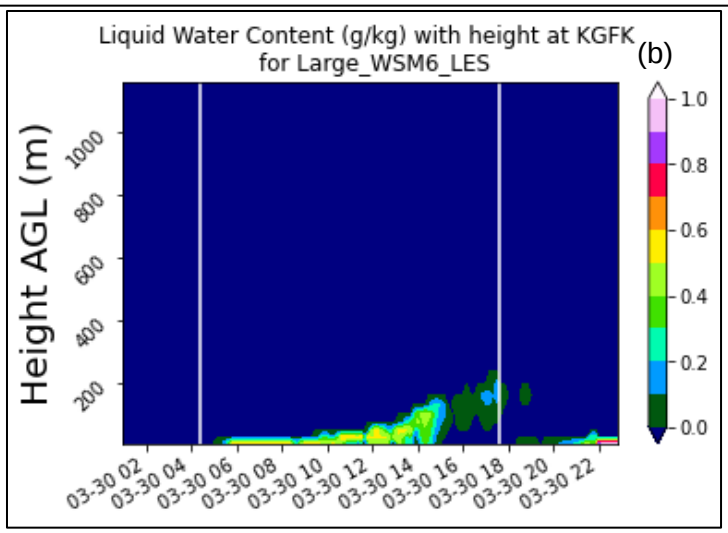

Figure 30(a,b): Vertical profiles of liquid water content (g/kg) above KGFK for different model configurations.

Horizontal Distribution of Cloud Water

The horizontal distribution of cloud liquid water content at the lowest scalar model level is used as a proxy for fog. The times selected in Figure 31 were selected to be close to the formation time of fog within the domain, during the middle of the fog event, and near the end of the fog event, and is limited to the area of the innermost domain. Figure 32 shows that the WDM6 scheme predicted a larger fog area and larger LWC values than WSM6. The model, at the time selected, shows false alarms in the southern half the domain. The fog in the LES domain, while it had appeared early compared to YSU runs, still appeared late. During the middle of the fog event the fog in the LES runs appears much more scattered than in its mesoscale counterparts. The LES-WDM6 model run has substantially higher liquid water content than the LES-WSM6 run. At the last selected time period, no fog appears in the domain for the LES runs. In the mesoscale domains the WSM6 produces substantially smaller fog liquid water than the WDM6 runs.

Satellite observations from GOES and MODIS are available for comparison with model solutions. During the daytime, the Day-Fog-Snow and Daytime Microphysics RGB products are used to determine the extent of cloud cover. While these products can neither indicate visibility at the surface nor fully distinguish low level status from fog, their combination enables separation of liquid water clouds from upper-level clouds and snow-cover from liquid water clouds. Over the domain the surface snow cover is indicated the red hues in the Day-Snow-Fog product and the green hues in the Daytime Microphysics product (Figure 34). High level cirrus is indicated in the Daytime Microphysics Product by the red colors. A low-level cloud is indicated by the white colors on both products. High level clouds can also be seen overlying lower-level clouds by gradients in Nighttime Microphysics product (Figure 33). While clouds are indicated in the domain in the True Color Imagery, it is difficult to separate the clouds from snow cover. MODIS imagery is provided in Figure 35. At this time high clouds are present over the domain. As in the GOES imagery, the

snow in the middle portion of the Red River Valley and the high ice clouds can be discerned. During the nighttime, the BTD method can be used to determine fog. A region of positive BTD, which is an indicator of possible fog, is aligned along the Minnesota/North Dakota border.

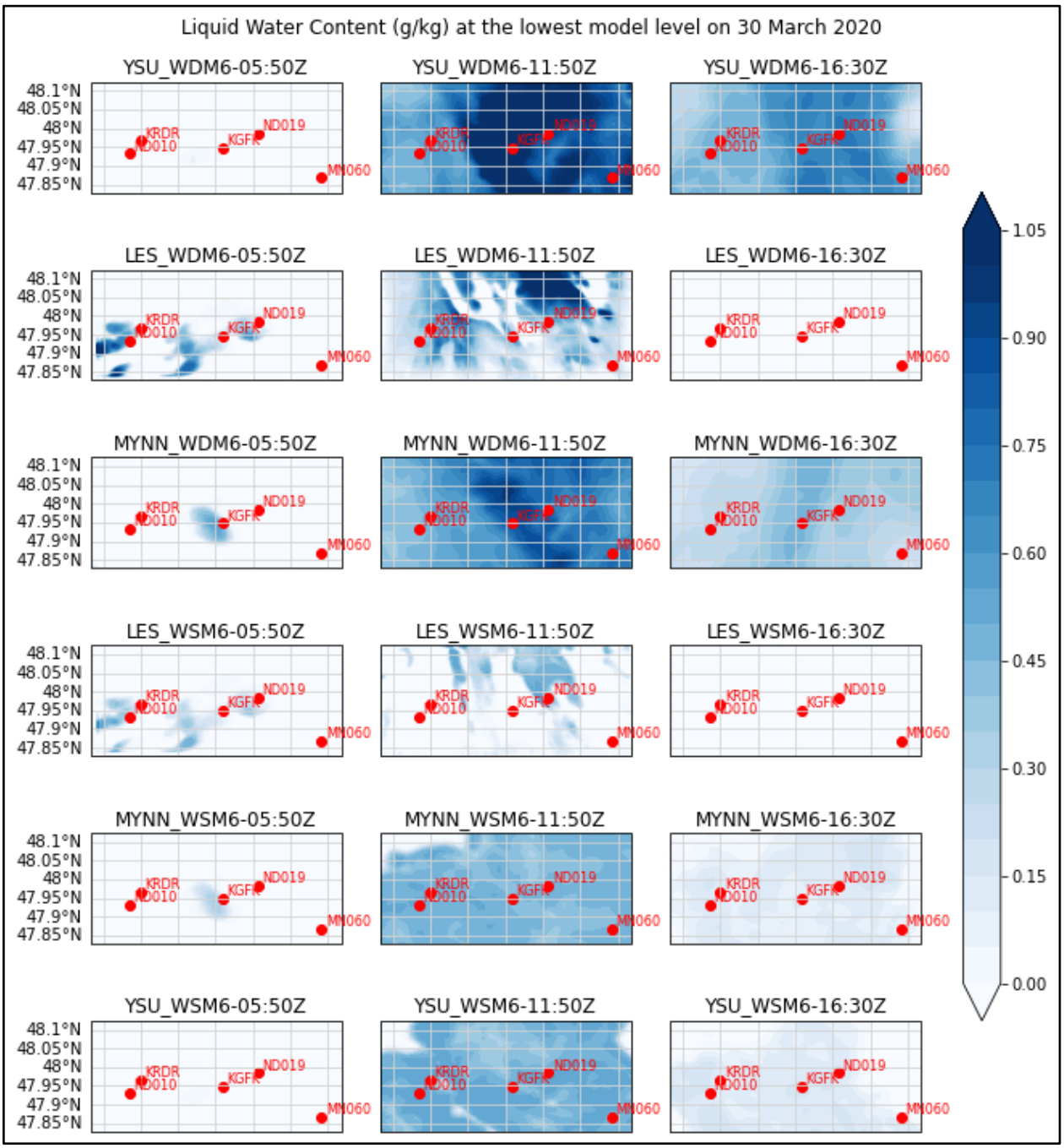

Figure 31: Cloud liquid water content at the lowest model level for WRF model runs. Red dots indicate the location of the station in the domain.

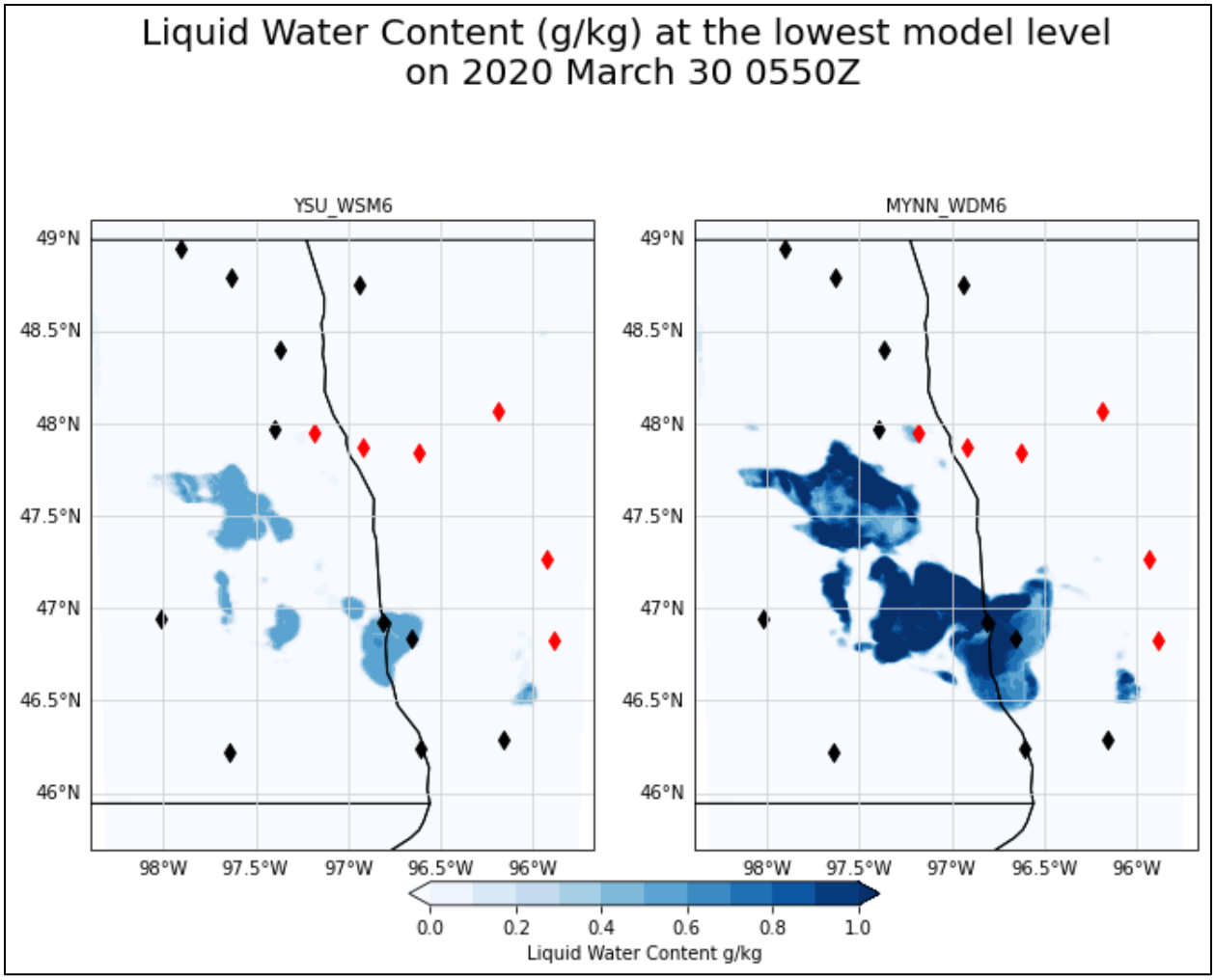

Figure 32: Cloud liquid water content at the lowest model level for YSU_WSM6 and MYNN_WDM6 model runs. Red dots indicate that fog was observed at the closest observation time; black indicates that no fog was observed.

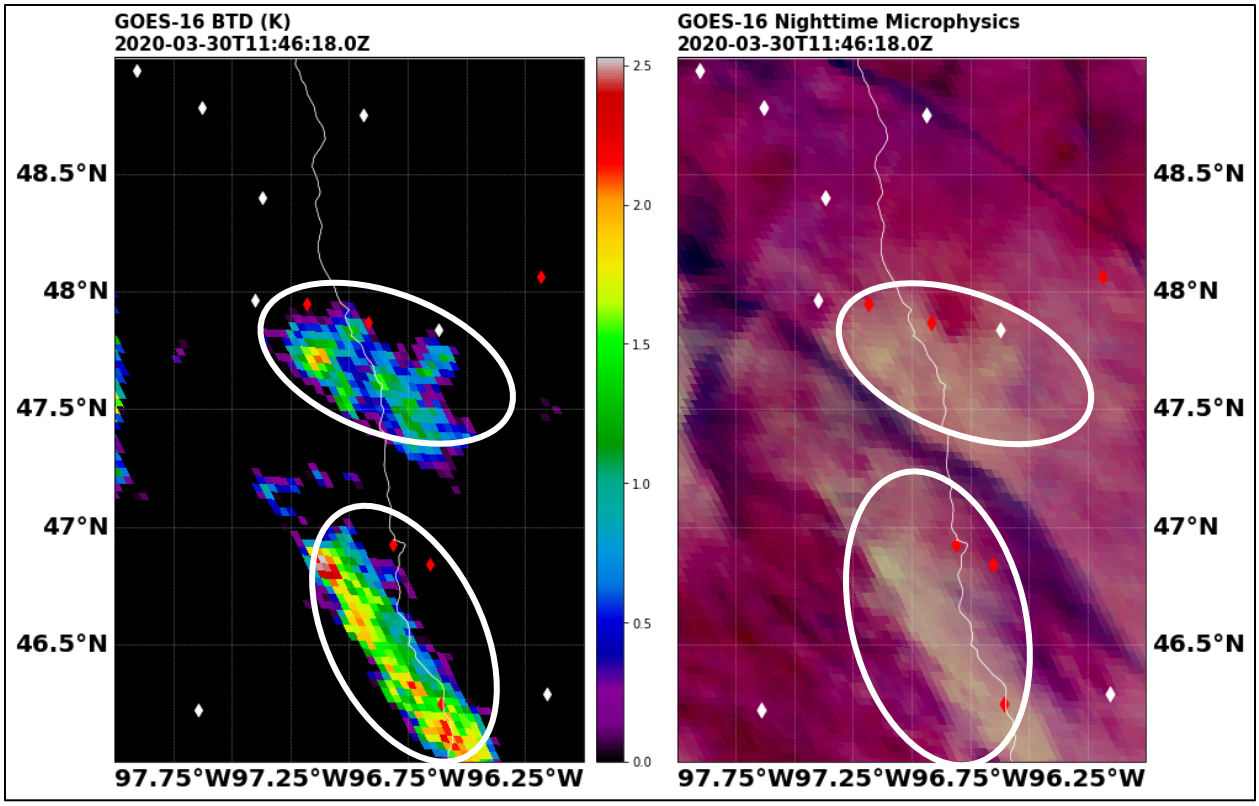

Figure 33: GOES-16 Nighttime imagery of the fog event. Negative values for the BTD product are clipped to 0 ΔK. In the BTD imagery and in the Nighttime Microphysics imagery, a white ellipse outlines possible areas of low-level clouds/fog. Red dots indicate that fog was observed at the closest observation time; white indicates that no fog was observed.

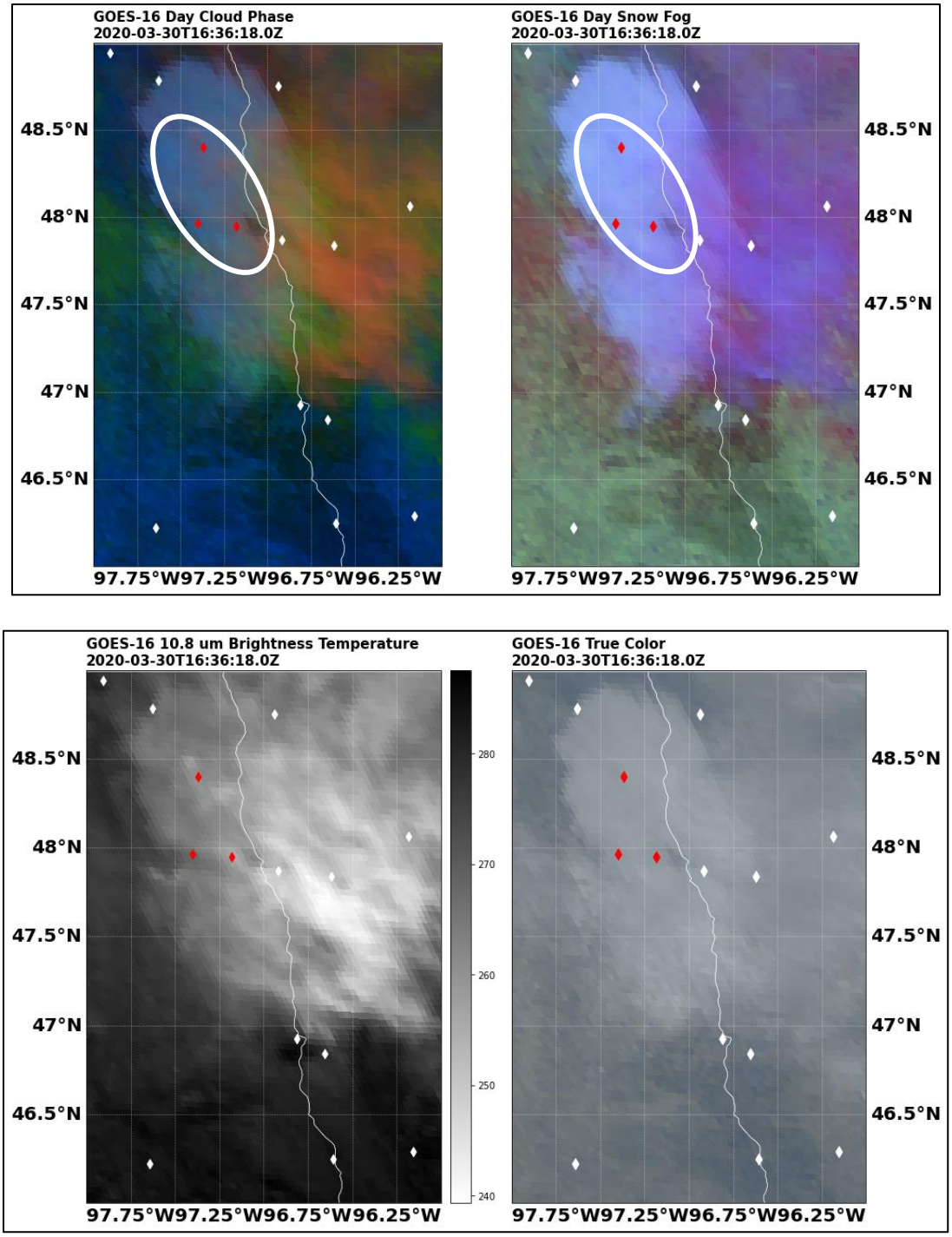

Figure 34: GOES-16 Daytime Microphysics, Day Snow Fog, 10.8 um Brightness Temperature, and True Color imagery over the Grand Forks Doman. A white ellipse outlines an area of suspected fog/low clouds. Red dots indicate that fog was observed at the closest observation time; white indicates that no fog was observed.

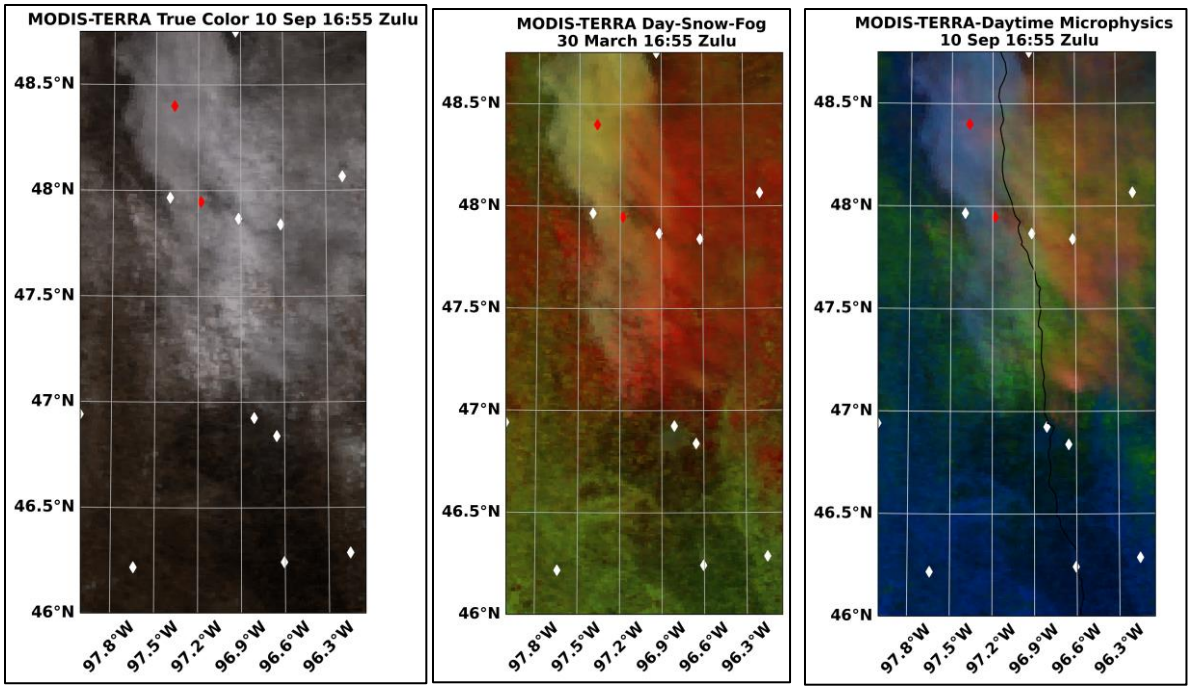

Figure 35: MODIS-Terra Imagery. Products for True Color, Day-Snow-Fog, and Daytime Microphysics are included.

Station Meteograms

Modeled conditions at relevant stations—KGFK, KRDR, and MN060—are presented via meteograms (Figures 31-33). During the fog event a large cold bias is present during the modeled fog period. A portion of the bias in the relative humidity may have been due to sensor performance, as the relative humidity sensor reported relative humidity values of around 90% during periods of low visibility at KGFK. After the fog dissipates at KGFK in the model, the relative humidity remains high for all model runs, with fog failing to dissipate at all for YSU-WDM6 (Figure 40). Wind speed is consistent biased high throughout the simulation period for the LES model runs. Both KRDR and MN060 have positive biases in wind speed for substantial portions of the event for all model runs. The biases in surface variables vary between "fog" and "non-fog" periods. Performance also varies between each of these selected stations/grid-cells, despite their relatively close spatial proximity. At KGFK, the models fail to capture the sharp drop in relative humidity

after fog dissipation, keeping the relative humidity and greater than 90%. In these model runs, the fog dissipated too late in most cases, allowing for more reflection (and thus less heating) of the surface during the daytime. The cold bias during the fog period across all model runs is less prominent at KRDR and MN060 than it is at KGFK. The fog in the simulations often formed early, dissipated, and then reformed after the first observation of fog at a station. This also applies to the dissipation phase, especially for the LES runs. This simulation behavior apparent at KRDR. While there was some variability in observed visibility at KGFK, the modeled fog was much more sporadic at KGFK.

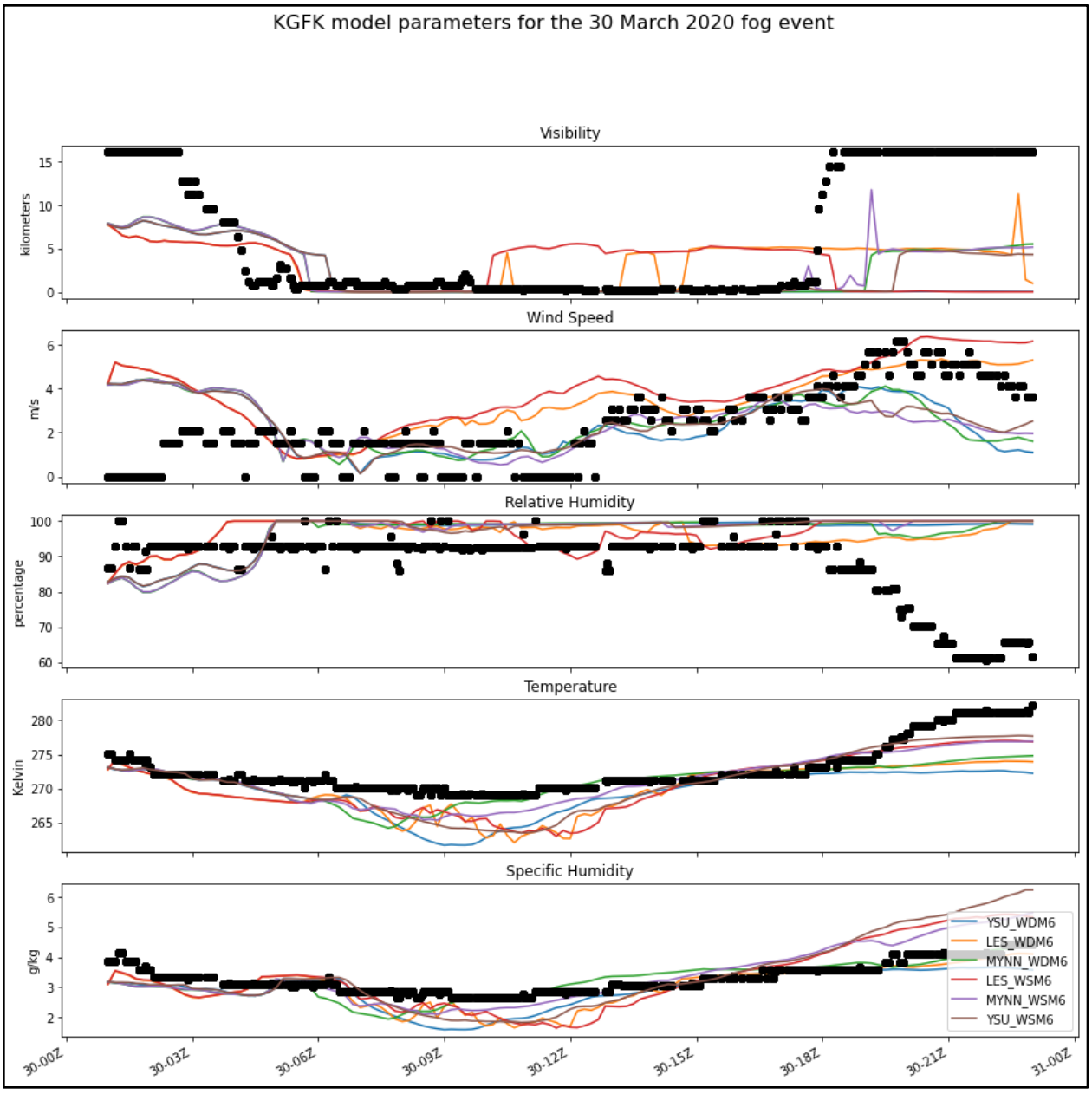

Figure 36: Surface Observations at KGFK. Black dots represent observations.

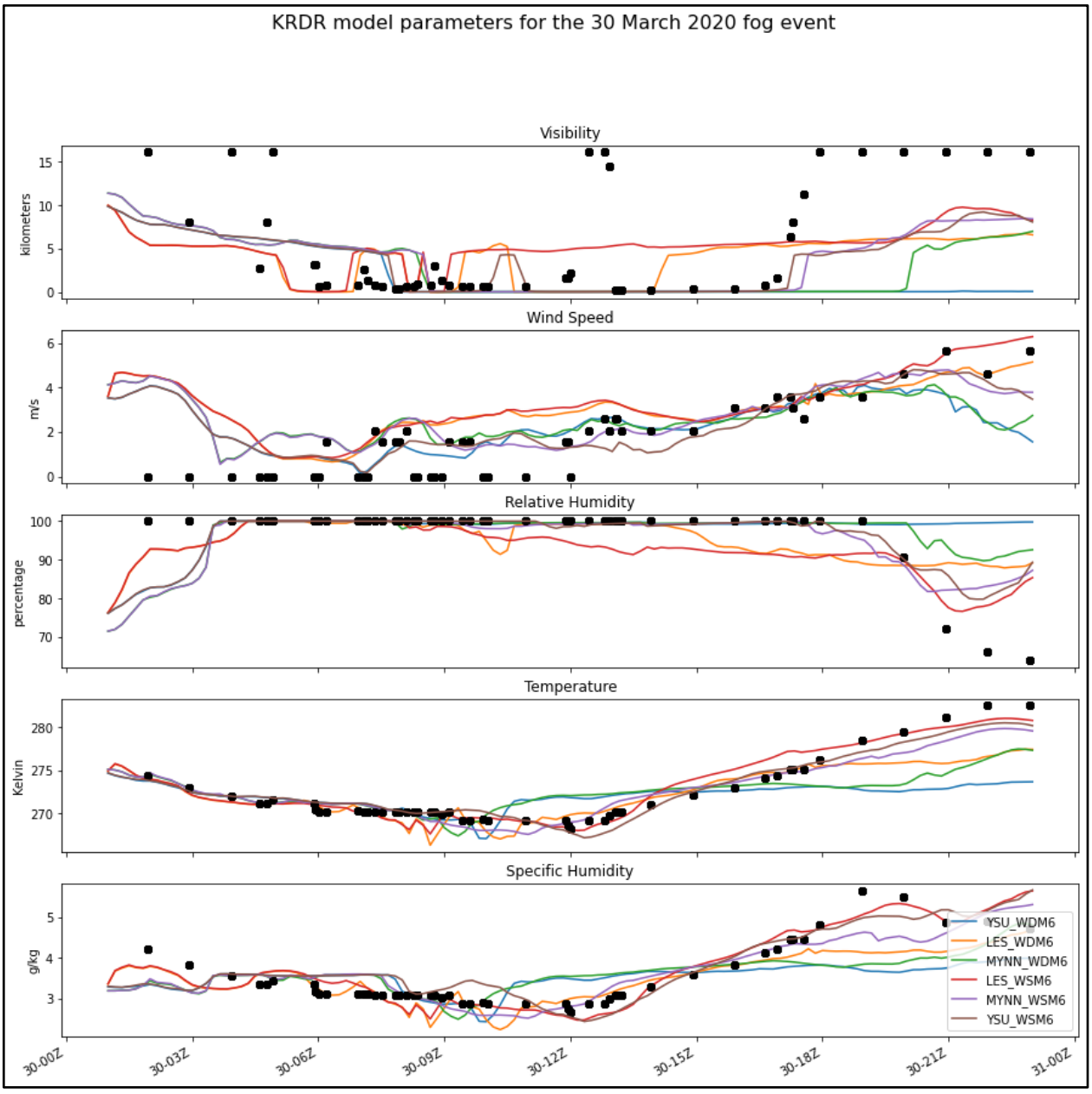

Figure 37: Surface Observations at KRDR. Black dots represent observations.

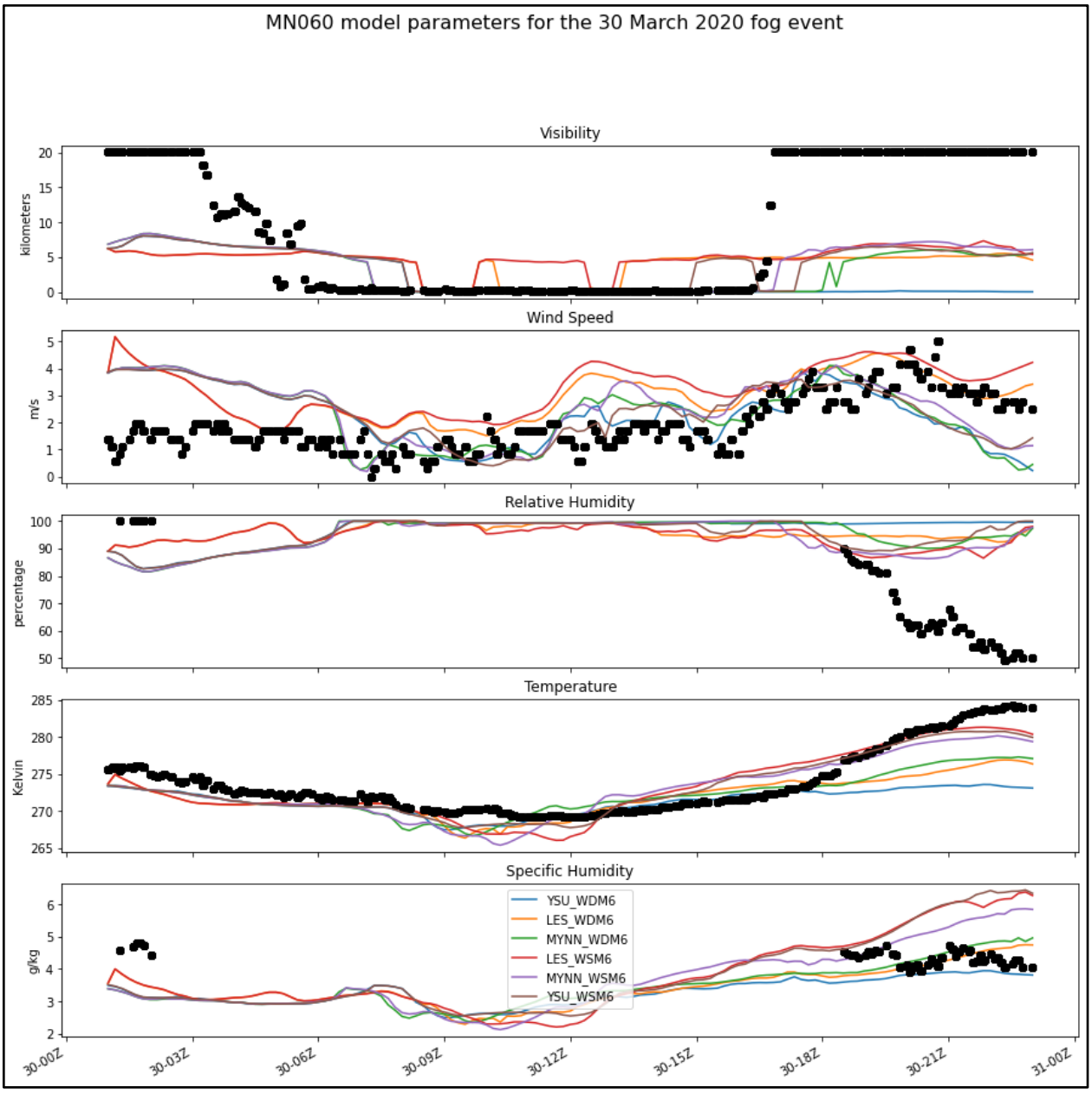

Figure 38: Surface Observations at MN060. Black dots represent observations

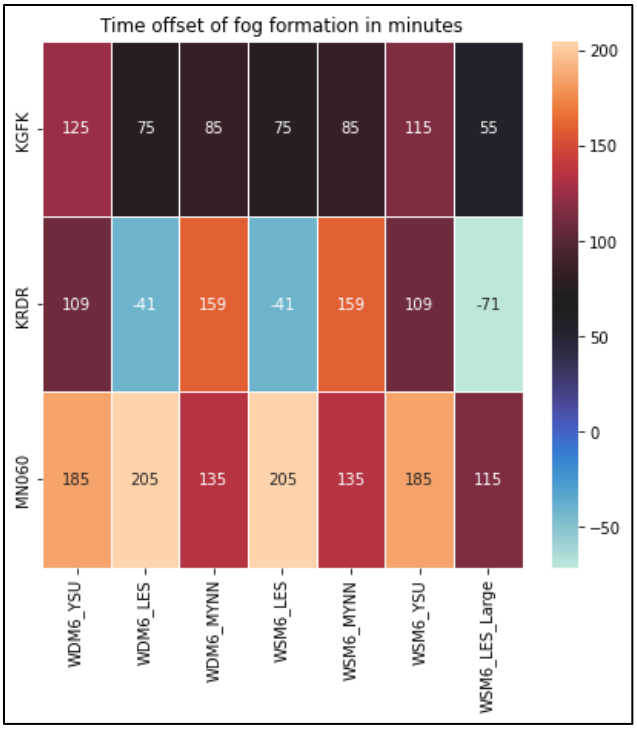

Figure 39: The difference in minutes between the observed formation time and the time fog first formed in the model at the closest grid cell to the location.

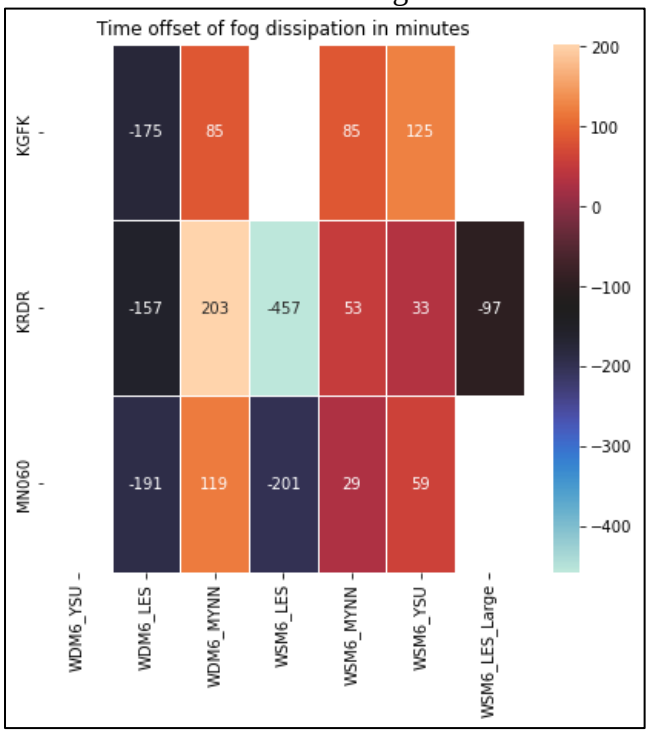

Figure 40: This represents the difference in minutes between the observed fog formation time and the time fog first formed in the model at the closest grid cell to the location. White cells indicate that fog did not form for that model run, or that fog did not dissipate by the end of the model run.

Chapter 5: Discussion

The differences in fog formation and dissipation times in the Minneapolis events between the parent mesoscale domain and the sub-kilometer domain show the strong influences of nesting, turbulence parameterization, and microphysical parameterization upon fog simulation. Differences in fog formation between the mesoscale runs are influenced by the precipitation that occurred during the 13-hour long model-spin up period. As many of the mesoscale runs did not properly forecast precipitation accumulation, the model took longer to cool to saturation at stations on the southern side of the domain. The modeled fogs with late formation times often have early dissipation times, compared to observations. The warm bias associated with this event is also prevalent in the HRRR forecast fields at multiple spin-up times. Despite a moist bias in dew point being present in the WRF fields at many stations, the warm bias offsets this, leading to an overall dry bias in relative humidity.

It cannot be conclusively stated that the sub-kilometer simulations offered an improvement over the parent mesoscale simulations. The YSU_WDM6 and LES_WDM6 model runs are a key example. The LES_WMD6 was able to forecast fog at KMSP where none had occurred in the parent domain. While still having large biases in formation/dissipation times, formation times are improved across all stations except for KFCM where fog suffered a significant delay in formation. While dissipation times were also improved at some stations, overly persistent fog formed at others where it failed to dissipate by the end of the model simulation at 17 UTC. Despite this disadvantage, the LES domains had lower biases and MAE in the prediction of T2, which was the most likely factor behind the improved fog simulation. The domain wide POD, TS, and HSS are improved with the inclusion of the LES domain, despite some differences in the final formation and dissipation times. One drawback is the increased number of false alarms. The WDM6 model runs have a higher FAR compared to the WSM6 model runs in both nested and parent domains.

In LES_WDM6, FAR increases compared to the parent domain. As discussed previously, the predicted LWC is large and the droplet number concentration is erroneously high. The RRTMG radiation scheme directly takes these variables into account (Bae et al. 2016). The high droplet number concentration decreases the effective radius, increasing the optical depth. This lowers the amount of solar radiation received at the surface and thus the heat flux into the base of the fog. While not the sole factor behind the persistence of fog in LES_WDM6, this situation demonstrates the complex interplay between turbulence, radiation, and land atmosphere interactions in fog modeling.

At most stations, the dry bias in relative humidity was due to a warm bias, rather than a lack of moisture. This warm bias occurred across all stations in the innermost domain. This finding aligns with that of Kutty et al. (2021) who reported a similar warm bias with a fog event over Delhi, where they attributed the bias to a lack of inclusion of land surface processes. Furthermore, Ryerson and Hacker (2014) determined that part of WRF's failure in predicting low visibility was due to a dry bias in relative humidity due to a warm bias in temperature.

The land surface scheme used is the Noah-LSM along with the MODIS IGBP for land use classification. Under this system, the Minneapolis domain is largely described as a single land use category--'Urban and Build-Up' (category 13). Within the Minneapolis area are a variety of sub-classifications of urbanized space including suburbs, a dense city center with large buildings, and parks. As the different processes and characteristics in a grid cell cannot be fully represented by a single land use category (Arya 2001), this may have led to the large warm bias seen across the simulations. The land surface fluxes of heat and moisture vary for these types of surfaces. The default version of the Noah LSM used in this investigation only considers the dominant land category of each grid cell (sf_surface_mosaic = 0) and the grid spacing of the model is very close

to that of the land use dataset. The inclusion of an Urban Canopy Model, which accounts for the differences among urban land use classes, may improve fog forecasting. Additional benefits may also be realized with use of higher-resolution land-use datasets and higher-resolution topography datasets such as from the Shuttle Radar Topography Mission, which has resolution on the order of 100 m (Farr et al. 2007). The spatial effect of this warm bias is apparent in the evolution of the fog across the domain (Figure 20, 21). In each simulation member fog forms along the periphery of Minneapolis but fails to penetrate inward until well after it had formed (from observations). This difference in land use classes likely led to failure to properly propagate into the urban area, delaying formation time.

The LES_WDM6 run is of particular interest since it also had late dissipation times, rather than early dissipation times. While no observations of cloud drop number concentration or liquid water content are available, the values produced by the model are quite large compared to that typically reported in the literature, with mixing ratios exceeding 1 g kg^{-1} at times. As the RRTMG radiation scheme parameterizes cloud albedo using these variables, the albedo may be unrealistically high, leading to a too long-lived fog Boutle et al. (2018). Overly persistent fog lowered the amount of solar radiation received at the surface after sunrise on 10 September 2020, leading to a strong cold and moist bias in the early morning hours. This partially explains the low correlation coefficient values between modeled and observed T2 for the WDM6 model runs.

It is interesting to note that the HRRR model forecast fields performed better for initialization times closer to the start of the actual fog event. As observations are assimilated hourly in the HRRR, precipitation information from the rainfall event was incorporated. Thus, the low-level moisture in both the atmosphere and soil were better represented in the model, which allowed for more accurate onset and dissipation times of the fog. In the HRRR simulations, as with the

WRF simulations, there is a warm and dry bias in 2 m temperature and relative humidity, respectively. These improve with closer initialization times. For example, the T2-RMSE improves from 2.16 K to 1.2 K from the 18 UTC to the 22 UTC initialization.

The visibility schemes used relative humidity, cloud liquid water content, and cloud droplet number concentration. These algorithms can have difficulties distinguishing the magnitude of visibility decrease in fog, mist, and haze Long et al. (2021). The RUC algorithm, used when explicit liquid water content is not present, has a lower limit of approximately 4.21 km. The SW1999 and G2006 parameterizations can predict visibilities below 1 km in this study, but there is a lack of intermediate range visibilities between 1 km and 4.21 km. While other visibility parameterizations are available, each parameterization still has advantages and weaknesses that must be considered when forecasting visibility. For example, the type and size distribution of aerosols are not accounted for in the visibility parameterizations and the shape of the distributions in the microphysical schemes may not appropriately describe the observed fog (Lin et al. 2017; Long et al. 2021). While WDM6 does prognostically predict the number concentration of cloud condensation nuclei, this number is a depends upon a default value provided by the user upon initialization. The Gultepe (2006) visibility parameterization, while accounting for number concentration, requires the use of the double moment scheme, which increases the computational burden of the simulations.

The results are evaluated further with a different parameterization scheme for visibility. This parameterization utilizes both the cloud droplet number concentration N_c (# cm^{-3}) and the cloud water mixing ratio (g m^{-3}). Difficulties were encountered with using this parameterization. While no observations of LWC or N_c were available during the events, the reported results were unrealistic. N_c is only reported from model runs with the WDM6 scheme, as WSM6 is single

moment across all hydrometeor classes (N_c within the WSM6 scheme is a prescribed constant of 300 cm^{-3}). The WDM6 N_c at the lowest model level across many models runs exceeded 50,000 cm^{-3}, or 10^{10} m^{-3}, an unrealistic value for fog Gultepe et al. (2006). A suspected cause is the condensation and activation of N_c by the WDM6 scheme, and erroneously large supersaturations (within a supersaturated grid cell activation of cloud droplets is the first source of N_c, with each cloud droplet having a radius of 1.5 μm). To investigate whether this drastic overestimation of N_c is due to an error within the WDM6 microphysics scheme, the Milbrandt-Yau microphysics scheme (mp_physics = 9) was utilized within the 1 km domain. As with WDM6, this scheme is also a double moment scheme with respect to cloud liquid water, predicting both mass mixing ratio and number concentration. For this scheme the range of N_c values is much more realistic, albeit high, with results on the order of 100 - 500 cm^{-3}.

One surprising result was that, contrary to the findings of other research (Lin et al. 2017; Román-Cascón et al. 2016), the HRRR performed better with smaller spin-up times rather than longer spin-up times. It should be noted that a 72 hr forecast used in the aforementioned articles was not possible using HRRR forecasts. When different initialization times for the HRRR were compared for the Minneapolis event, the biases and errors in the surface meteorological variables were smaller for those model runs with initialization times closer to the fog event. The spin-up time used for the WRF model runs was 13 hrs. While sensitivity to spin-up time was not studied, it is suspected that if the spin-up time were to be shortened to 6 hrs a substantial reduction in computational cost would result along with an improved forecast. As each fog case is different, it is not possible to say if this would be a globally optimal spin-up time.

In a sensitivity study of the droplet settling scheme for fog, inclusion of droplet settling produced a poorer forecast. As stated in the introduction, the lifecycle of fog depends upon

interactions between radiation, turbulence, droplet settling, and surface fluxes. While thinner fogs are expected to have lower sedimentation rates compared to thick fogs (due to smaller droplet sizes) thus enabling fog formation/persistence, radiative cooling and sensible heat flux divergence in the model was not strong enough to allow the fog to persist. WRF and other operational models produce liquid water content that is too high if droplet settling is not included (Taylor et al. 2021). While valuable for providing for more realistic LWC values in deeper, optically thick fogs, a future modelling investigation could further evaluate the effect of droplet settling on thin fogs.

The inaccurate droplet number concentration predictions may be due to the fact that the schemes used in this study are saturation adjustment schemes and have cloud droplet activation functions designed for convective clouds, rather than fog (Schwenkel and Maronga 2019). Some microphysics schemes, including the Milbrandt-Yau scheme (Milbrandt and Yau 2005a,b), parameterize droplet activation as a function of vertical velocity. The Milbrandt-Yau scheme requires a minimum vertical motion of 0.001 m s^{-1} (1 mm s^{-1}) in its function for nucleation of cloud droplets. In the case of negligible or downward vertical motion, the cloud drop number concentration is the maximum of the following two values: (1) the current number concentration or (2) a number concentration based on the background value of the assumed CCN environment. Poku et al. (2021) discuss how aerosol activation formulas and microphysics schemes designed for convective clouds may not function well for fog, which results in erroneous approximations of the supersaturation. As the background value of CCN in the Milbrandt-Yau scheme easily exceeds the number concentrations found for fogs in the literature, the effective radius of the droplets may become too small. This makes fog a more effective in scattering shortwave radiation, which causes possible delays in fog dissipation.

While not used in this study, in WRF the aerosol-aware Thompson scheme presents a more realistic view of aerosol activation, but as reviewed by Weston et al. (2022), the scheme still has minimum vertical velocity thresholds for activation. Weston et al. (2022) and the source code of the Thompson aerosol aware scheme mention that the local cooling rate of the air (due to longwave radiation) could be used to diagnose a proxy updraft velocity, but this capability is not yet implemented into the WRF code. Yet, as stated by Boutle et al. (2018), this still may not be fruitful. When Boutle et al. (2018) derived the equivalent vertical velocity for the non-adiabatic cooling in fog, it was still below the minimum updraft velocity for activation within the scheme; they concluded that specialized parameterizations will be needed for fog microphysics. A further complication is that Schwenkel and Maronga (2019) determined that one moment microphysics performed better than two moment microphysics; they isolated the error in saturation adjustment schemes to the activation parameterization of droplets present within the two moment scheme they used. Similar to this, Poku et al. (2021) modified the Shipway aerosol scheme, wherein they altered the activation scheme to account for activation due to non-adiabatic cooling, which did improve simulations.

The Grand Forks case differs from the Minneapolis case in a few key ways. Overall, the two sub-kilometer nests did not improve the fog simulation compared to the mesoscale domains. The WSM6-LES run had an HSS of near zero. Interestingly, there was a large impact of the sub-kilometer domain size. With the same microphysics scheme and spin-up time, the WSM6-LES-Large-Domain had a substantially higher HSS (0.43) and a lower FAR (0.28), showing the strong boundary effects of nesting upon the simulation. Rather than a warm bias, there is a substantial cold bias in the innermost domain. This event occurred over snow-cover, and the bias was common among all model runs. Snow depth being too deep and snow albedo being too high are common

causes of cold biases in T2 with the Noah LSM and WRF Varga and Breuer (2020). While the nearest grid point in the model runs have snow depths comparable with observations (2 in) at the Grand Forks measurement station, observations in the area are limited, so errors in the land surface parameterization cannot be concluded to be the sole factor behind the failure to properly forecast T2 (NCEI 2022). The impact of snow-cover upon fog formation (albeit in complex terrain) has been examined before by Zhang and Pu (2019), who determined that underestimated snow albedo resulted in WRF's failure to predict fog. Additional sensitivity studies, including those for the land surface scheme and the radiation schemes, would be needed to make a conclusion on the exact mechanism of the cold bias. At KGFK a large cold bias is noted during the overnight hours, where models predict temperature biases > 3 K in magnitude. Thus, fog can be said to have formed for the wrong reason, as the cooling was much too strong for this event.

While observations of liquid water content and cloud drop number concentration were not available, a likely explanation behind part of the T2 bias and the late dissipation times of fog is due the fog being too optically thick. Similar to the Minneapolis case, the number concentration in runs with the WDM6 microphysics scheme are unrealistically high along with having higher liquid water content throughout the depth of the fog layer. This increased the albedo of the fog, preventing absorption of solar radiation and heating of the boundary layer and of the land/snow surface. In the WDM6_LES run and the WSM6_LES run, fog formed only in a shallow layer, with the lowest model grid cell being saturated. Performance improved drastically for a 333 m grid spacing domain with an increased number of grid points. The likely explanation for this performance improvement is stations are further from the boundary of the domain, showing the strong influences of boundary effects on limited area simulations.

Impacts on Small Unmanned Aircraft Systems

The findings of this study have key implications for Part 107 sUAS operations. One of the most important factors of this study for the sUAS industry is the prediction of visibility. As of 27 February 2022, 15 organizations sought a waiver for Part 107.51(c) (reduced visibility), and 8 waivers were sought for 107.51(d) [1] (FAA 2022). While the number of waivers to fly in low visibility scenarios is not high, the need is still present within the industry. Part 107.51(c) limits operations with visibility below 3 statute miles (≈ 4.82 km). Depending only on an LWC-only visibility parameterization using direct model output may result in many missed fog events, as demonstrated in this study. Further statistical post processing or rule-sets may improve the forecasting of fog. As it is only a simple diagnostic and thus not able to consider the types of aerosols present, the RUC formula often underestimates visibility. Another challenge is prediction of relative humidity. Periods of high relative humidity (> 90%) and high visibility (10 km) were present in the observations.

Each individual sUAS component is manufactured to withstand different environmental conditions (i.e., temperature and humidity). As flying a sUAS outside of its safety tolerances violates 107.23(a) and 107.15[2], the forecast of these surface meteorological parameters remains important, even in the absence of fog. The dry bias observed herein may limit the value of the forecast to sUAS pilots whose aircraft or payloads are sensitive to the value of relative humidity. Such an example would be a mission using MWIR (medium wave infrared) or LWIR (longwave infrared) sensors (Khare et al. 2018). In the WRF forecasts, fog/cloud height and depth varied

[1] Part 107.51(d) dictates that the distance of the sUAS below a cloud base be no less than 500 feet (152.4 m).
[2] 107.23(a) relates to the reckless or dangerous use of a UAS. 107.15 concerns conditions of safe operation of a UAS.

significantly. In the WDM6-YSU Minneapolis simulation, WRF forecasted fog at KMSP as a low stratus cloud rather than fog.

An additional fog formation mechanism is stratus lowering fog Wagh et al. (2021), where fog forms from pre-existing stratus clouds. Fog can also lift into stratus (dissipating from the ground upwards). As fog dissipates, the cloud base may still be below 500 feet, while visibility increases at the surface. Thus, restrictions remain in place even though visibility restrictions are no longer a factor. These factors show WRF's ability to differentiate fog and stratus still impacts Part 107 operations before and after visibility decreases below 3 statute miles at the surface.

A single model run provides limited probabilistic information and is often used to provide a deterministic/dichotomous forecast. Alternative visibility schemes, such as Gultepe and Milbrandt (2010), use a probabilistic approach to parameterize visibility based on relative humidity. While an ensemble forecast is computationally expensive, it could also be used to generate a probabilistic forecast. Probabilistic forecasts, rather than a deterministic forecast, would be of use to sUAS operators to allow them to judge their own risk thresholds for mission planning, rather than the yes/no forecasts provided by deterministic methods. This holds value, as some operators may be more risk adverse, while others may have an operational framework that is less sensitive to false alarms/missed fog forecasts. Future work could be to evaluate the performance of the sub-kilometer domain within a probabilistic forecasting context.

An additional complexity is that on 21 April 2021 new FAA rules regarding flights at night went into effect; both commercial and recreational flyers can fly during nighttime hours (FAA 2022). Since radiation fog usually forms overnight, this new provision increases the probability that fog may impact sUAS operations. As both the HRRR and the WRF runs did not properly forecast the onset and dissipation times, this would impact the amount of time sUAS pilots could

safely operate. Due to the dry bias in relative humidity, likely due to deficiencies within the land surface scheme, WRF struggled to form fog over the Minneapolis metropolitan area. This would impact the missions of sUAS operators in urban areas, such as infrastructure inspections and real estate photography.

Chapter 6: Conclusion

This study's analysis did not show a consistent benefit of using the WRF model with sub-kilometer grid spacing and LES closure for fog forecasting. This is evidenced through the offsets in formation and dissipation times for each model run. While using an LES domain may show improvement in fog onset/dissipation time at some stations for a particular model run as compared to a mesoscale simulation, it often showed a degradation in the fog onset/dissipation forecast at other stations. For the Minneapolis event, the LES simulations showed improvement in fog formation and dissipation times at many stations, producing fog where none had formed in mesoscale domains. Yet, the LES simulations also worsened fog formation times at other stations compared to other mesoscale simulations. In the Grand Forks event, the WSM6_LES domain produced a less accurate fog forecast, wherein most of the fog event was missed and fog was produced at the wrong time. Alternative configurations of sub-kilometer nests showed little domain-wide performance gain compared to using mesoscale simulations. While using a larger domain for WSM6_LES produced drastic improvement in dichotomous skill scores, the results are still comparable to the mesoscale simulations.

In the Minneapolis case, the SMS-3DKE grey scale closure was used in addition to the traditional 1.5 TKE closure. Like its traditional LES counterpart, this offered little to no improvement over mesoscale simulations. Using a 333 m grid spacing in numerical models has produced improvement in other studies, as outlined in the introduction. The failure of the WRF model to produce fog in this study can likely be traced to the spin-up time, domain size, and influences of the land surface parameterization. Large biases of the urban area influenced the 2 m temperature field, lowering the relative humidity and increased the time to achieve saturation. A potential way to alleviate these biases would be to use higher resolution land-use data and topography datasets. Furthermore, placement of precipitation during the rain event during the

model spin up period was incorrect, which influenced surface moisture fields. The microphysical schemes were a further influence upon the event. Despite accounting for more of the actual cloud physics, the WDM6 often produced a worse dissipation time, where the fog failed to dissipate by the end of the simulations due to a more optically thick fog.

In the Grand Forks event, the WSM6_LES and WDM6_LES domains were too small, suffering from boundary effects. Future work could further investigate the influence of sub-kilometer domain size upon fog formation. A large cold bias present in simulations at KGFK may be related to the representation of snow cover within the Noah-LSM, again highlighting the importance of surface fluxes upon fog formation. As with the Minneapolis event, the WDM6 scheme produced fog that became optically thick too quickly, which delayed dissipation time. This too, contributed to the cold bias. LES runs produced very shallow fog compared to their mesoscale counterparts, weakening the time the fog persisted compared to mesoscale runs.

The large offsets in fog formation and dissipation time as compared to observations represent a threat to the mission planning of sUAS operators. Within any single model simulation fog was often too persistent at some stations, while underpredicted at other stations. Furthermore, the choice of visibility/fog presence parameterization scheme led to differences in the modeled formation/dissipation time and fog intensity, demonstrating the limitations of these schemes to appropriately describe individual fog events. Depending on the location of operations, these factors would cause either unnecessary flight cancellations, lengthy delays, or interrupted operations. Error in fog forecasting create safety hazards if operators accidently fly into fog. As fog does not form and dissipate uniformly, the visibility at the command-and-control station may be above 3 miles, but fog may still be present nearby. This presents a threat to operational planning when using either ASOS observations or model forecasts.

A conclusive benefit to using nests with sub-kilometer grid spacing was not apparent for both cases (using WRF). This is due to the myriad of influences on the fog lifecycle. Biases in one physical parameterization have the possibility of overwhelming any benefit that might be gained from using a sub-kilometer LES nest, as in the case of fog that failed to dissipate with the WDM6 schemes. Using a sub-kilometer nest may improve the forecast for a portion of the domain but can degrade other areas of the domain, as compared to a mesoscale simulation. Due to the large number of meteorological factors and their nonlinear interactions involved in fog cases, more fog events would need to be analyzed to form firm conclusions regarding use of a 333.3 m domain for fog forecasting with the WRF model. As fog is impacted by the land surface attributes, this would involve fog events in various seasons, as snow cover and surface moisture impact the fog lifecycle. Fog events with different profiles of atmospheric temperature, relative humidity, cloud cover, and near surface wind speed should also be examined to fully understand how accurately these parameters are represented with a nest having sub-kilometer horizontal grid spacing.

Appendix

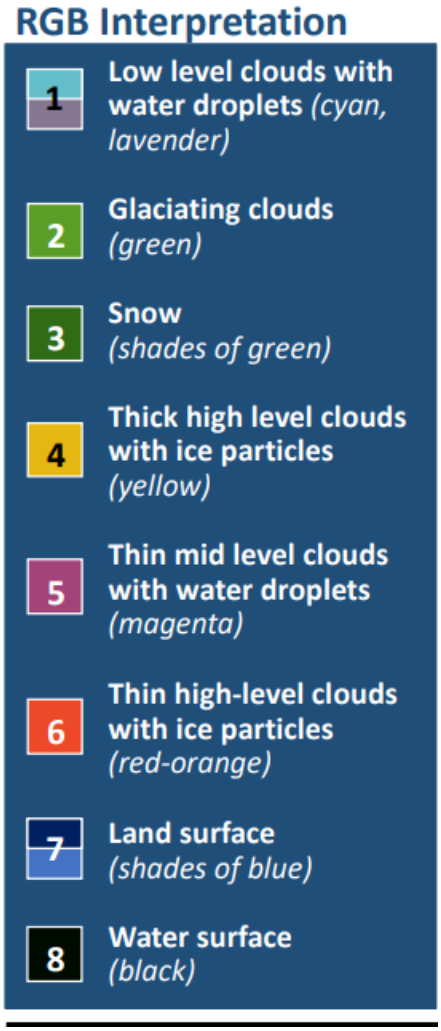

Figure 41: Day Cloud Phase Distinction RGB Interpretation (Cooperative Institute for Research in the Atmosphere 2022)

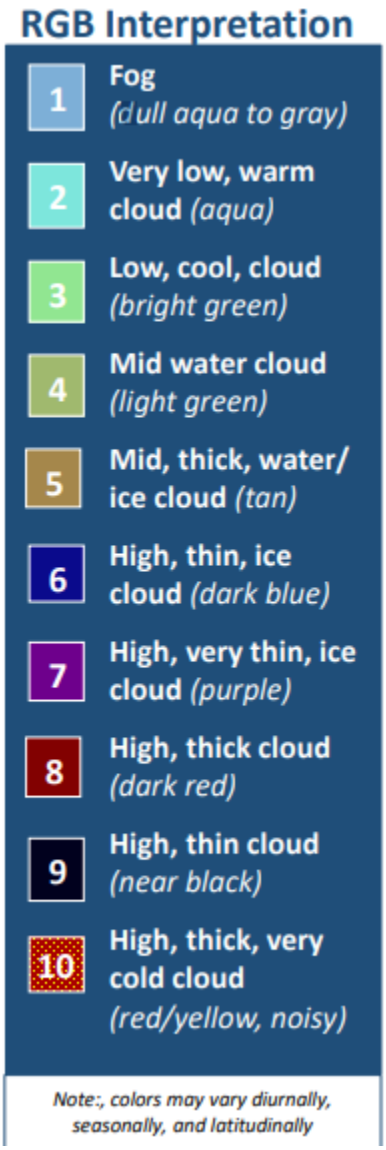

Figure 42: Nighttime Microphysics RGB interpretation (Cooperative Institute for Research in the Atmosphere 2022)

Figure 43: Day Snow Fog RGB interpretation (Cooperative Institute for Research in the Atmosphere 2022)

References

Anaconda, Inc., 2022: Miniconda.

Arya, S. P., 2001: Introduction to micrometeorology. 2nd ed. Academic Press, 420 pp.

Askelson, M., and Coauthors, 2017: Small UAS Detect and Avoid Requirements Necessary for Limited Beyond Visual Line of Sight (BVLOS) Operations. Aviation Faculty Publications,.

Bae, S. Y., S.-Y. Hong, and K.-S. S. Lim, 2016a: Coupling WRF Double-Moment 6-Class Microphysics Schemes to RRTMG Radiation Scheme in Weather Research Forecasting Model. Advances in Meteorology, 2016, e5070154, https://doi.org/10.1155/2016/5070154.

——, ——, and ——, 2016b: Coupling WRF Double-Moment 6-Class Microphysics Schemes to RRTMG Radiation Scheme in Weather Research Forecasting Model. Advances in Meteorology, 2016, e5070154, https://doi.org/10.1155/2016/5070154.

Baker, J., and T. Griffis, 2018: AmeriFlux AmeriFlux US-Ro4 Rosemount Prairie. https://doi.org/10.17190/AMF/1419507.

Bergot, T., 2013: Small-scale structure of radiation fog: a large-eddy simulation study. Quarterly Journal of the Royal Meteorological Society, 139, 1099–1112, https://doi.org/10.1002/qj.2051.

Blaylock, B. K., J. D. Horel, and S. T. Liston, 2017: Cloud archiving and data mining of High-Resolution Rapid Refresh forecast model output. Computers & Geosciences, 109, 43–50, https://doi.org/10.1016/j.cageo.2017.08.005.

Blaylock, Brian K., 2022: GOES-2-go: Download and display GOES-East and GOES-West data. https://doi.org/10.5281/ZENODO.4567558.

Boutle, I., J. Price, I. Kudzotsa, H. Kokkola, and S. Romakkaniemi, 2018: Aerosol–fog interaction and the transition to well-mixed radiation fog. Atmospheric Chemistry and Physics, 18, 7827–7840, https://doi.org/10.5194/acp-18-7827-2018.

——, and Coauthors, 2022: Demistify: a large-eddy simulation (LES) and single-column model (SCM) intercomparison of radiation fog. Atmospheric Chemistry and Physics, 22, 319–333, https://doi.org/10.5194/acp-22-319-2022.

Caswell, T. A., and Coauthors, 2021: matplotlib/matplotlib: REL: v3.4.3. https://doi.org/10.5281/ZENODO.5194481.

Cermak, J., and J. Bendix, 2008: A novel approach to fog/low stratus detection using Meteosat 8 data. Atmospheric Research, 87, 279–292, https://doi.org/10.1016/j.atmosres.2007.11.009.

Cohard, J.-M., and J.-P. Pinty, 2000: A comprehensive two-moment warm microphysical bulk scheme. I: Description and tests. Quarterly Journal of the Royal Meteorological Society, 126, 1815–1842, https://doi.org/10.1002/qj.49712656613.

Cohen, A. E., S. M. Cavallo, M. C. Coniglio, and H. E. Brooks, 2015: A Review of Planetary Boundary Layer Parameterization Schemes and Their Sensitivity in Simulating Southeastern U.S. Cold Season Severe Weather Environments. Weather and Forecasting, 30, 591–612, https://doi.org/10.1175/WAF-D-14-00105.1.

Cooperative Institute for Mesoscale Meteorological Studies, 2022: CIMSS Natural True Color.

Cooperative Institute for Research in the Atmosphere, 2022a: Nighttime Microphysics RGB.

——, 2022b: Day Cloud Phase Distinction RGB.

——, 2022c: Day Snow Fog RGB.

Cui, C., Y. Bao, C. Yuan, Z. Li, and C. Zong, 2019: Comparison of the performances between the WRF and WRF-LES models in radiation fog – A case study. Atmospheric Research, 226, 76–86, https://doi.org/10.1016/j.atmosres.2019.04.003.

Cuxart, J., 2015: When Can a High-Resolution Simulation Over Complex Terrain be Called LES? Front. Earth Sci., 3, https://doi.org/10.3389/feart.2015.00087.

Ding, Q., J. Sun, X. Huang, A. Ding, J. Zou, X. Yang, and C. Fu, 2019: Impacts of black carbon on the formation of advection–radiation fog during a haze pollution episode in eastern China. Atmospheric Chemistry and Physics, 19, 7759–7774, https://doi.org/10.5194/acp-19-7759-2019.

Dowell, D. C., and Coauthors, 2022: The High-Resolution Rapid Refresh (HRRR): An Hourly Updating Convection-Allowing Forecast Model. Part I: Motivation and System Description. Weather and Forecasting, 37, 1371–1395, https://doi.org/10.1175/WAF-D-21-0151.1.

Duthon, P., M. Colomb, and F. Bernardin, 2019: Light Transmission in Fog: The Influence of Wavelength on the Extinction Coefficient. Applied Sciences, 9, 2843, https://doi.org/10.3390/app9142843.

Duynkerke, P. G., 1991a: Radiation Fog: A Comparison of Model Simulation with Detailed Observations. Monthly Weather Review, 119, 324–341, https://doi.org/10.1175/1520-0493(1991)119<0324:RFACOM>2.0.CO;2.

——, 1991b: Radiation Fog: A Comparison of Model Simulation with Detailed Observations. Monthly Weather Review, 119, 324–341, https://doi.org/10.1175/1520-0493(1991)119<0324:RFACOM>2.0.CO;2.

eCFR, eCFR, 14 CFR Part 107 -- Small Unmanned Aircraft Systems. https://www.ecfr.gov/current/title-14/chapter-I/subchapter-F/part-107 (Accessed September 28, 2022).

Elson, P., and Coauthors, 2021: SciTools/cartopy: v0.20.0. https://doi.org/10.5281/ZENODO.1182735.

FAA, 2022: Part 107 Waivers Issued. FAA.gov,. https://www.faa.gov/uas/commercial_operators/part_107_waivers/waivers_issued/ (Accessed September 29, 2022).

Farr, T. G., and Coauthors, 2007: The Shuttle Radar Topography Mission. Reviews of Geophysics, 45, https://doi.org/10.1029/2005RG000183.

Gultepe, I., and J. A. Milbrandt, 2010: Probabilistic Parameterizations of Visibility Using Observations of Rain Precipitation Rate, Relative Humidity, and Visibility. Journal of Applied Meteorology and Climatology, 49, 36–46, https://doi.org/10.1175/2009JAMC1927.1.

——, M. D. Müller, and Z. Boybeyi, 2006: A New Visibility Parameterization for Warm-Fog Applications in Numerical Weather Prediction Models. Journal of Applied Meteorology and Climatology, 45, 1469–1480, https://doi.org/10.1175/JAM2423.1.

——, and Coauthors, 2007: Fog Research: A Review of Past Achievements and Future Perspectives. Pure appl. geophys., 164, 1121–1159, https://doi.org/10.1007/s00024-007-0211-x.

GUO, J., H. LEI, D. CHEN, and J. YANG, 2019: Evaluation of the WDM6 scheme in the simulation of number concentrations and drop size distributions of warm-rain hydrometeors:

comparisons with the observations and other schemes. Atmospheric and Oceanic Science Letters, 12, 458–466, https://doi.org/10.1080/16742834.2019.1670584.

Harris, C. R., and Coauthors, 2020: Array programming with NumPy. Nature, 585, 357–362, https://doi.org/10.1038/s41586-020-2649-2.

Heath, N. K., H. E. Fuelberg, S. Tanelli, F. J. Turk, R. P. Lawson, S. Woods, and S. Freeman, 2017: WRF nested large-eddy simulations of deep convection during SEAC 4 RS. JGR Atmospheres, 122, 3953–3974, https://doi.org/10.1002/2016JD025465.

Hoch, S. W., P. Calanca, R. Philipona, and A. Ohmura, 2007: Year-Round Observation of Longwave Radiative Flux Divergence in Greenland. Journal of Applied Meteorology and Climatology, 46, 1469–1479, https://doi.org/10.1175/JAM2542.1.

Hong, S. Y., and J.-O. J. Lim, 2006: The WRF Single-Moment 6-Class Microphysics Scheme (WSM6). Asia-Pacific Journal of Atmospheric Sciences, 42, 129–151.

Hong, S.-Y., 2010: A new stable boundary-layer mixing scheme and its impact on the simulated East Asian summer monsoon. Quarterly Journal of the Royal Meteorological Society, 136, 1481–1496, https://doi.org/10.1002/qj.665.

——, Y. Noh, and J. Dudhia, 2006: A New Vertical Diffusion Package with an Explicit Treatment of Entrainment Processes. Monthly Weather Review, 134, 2318–2341, https://doi.org/10.1175/MWR3199.1.

Horel, J., and Coauthors, 2002: MESOWEST: COOPERATIVE MESONETS IN THE WESTERN UNITED STATES. Bulletin of the American Meteorological Society, 83, 211–226, https://doi.org/10.1175/1520-0477(2002)083<0211:MCMITW>2.3.CO;2.

Hoyer, S., and J. J. Hamman, 2017: xarray: N-D labeled Arrays and Datasets in Python. Journal of Open Research Software, 5, 10, https://doi.org/10.5334/jors.148.

Izett, J. G., and B. J. H. van de Wiel, 2020: Why Does Fog Deepen? An Analytical Perspective. Atmosphere, 11, 865, https://doi.org/10.3390/atmos11080865.

Jayakumar, A., E. N. Rajagopal, I. A. Boutle, J. P. George, S. Mohandas, S. Webster, and S. Aditi, 2018: An operational fog prediction system for Delhi using the 330 m Unified Model. Atmos. Sci. Lett, 19, e796, https://doi.org/10.1002/asl.796.

——, H. Gordon, T. Francis, A. A. Hill, S. Mohandas, B. S. Sandeepan, A. K. Mitra, and G. Beig, 2021: Delhi Model with Chemistry and aerosol framework (DM-Chem) for high-resolution fog forecasting. Quarterly Journal of the Royal Meteorological Society, 147, 3957–3978, https://doi.org/10.1002/qj.4163.

Jiménez, P. A., J. Dudhia, J. F. González-Rouco, J. Navarro, J. P. Montávez, and E. García-Bustamante, 2012: A Revised Scheme for the WRF Surface Layer Formulation. Monthly Weather Review, 140, 898–918, https://doi.org/10.1175/MWR-D-11-00056.1.

Ju, T., B. Wu, H. Zhang, and J. Liu, 2021: Characteristics of turbulence and dissipation mechanism in a polluted radiation–advection fog life cycle in Tianjin. Meteorol Atmos Phys, 133, 515–531, https://doi.org/10.1007/s00703-020-00764-z.

Katata, G., 2014: Fogwater deposition modeling for terrestrial ecosystems: A review of developments and measurements: REVIEW OF FOGWATER DEPOSITION MODELING. J. Geophys. Res. Atmos., 119, 8137–8159, https://doi.org/10.1002/2014JD021669.

——, M. Kajino, T. Hiraki, M. Aikawa, T. Kobayashi, and H. Nagai, 2011: A method for simple and accurate estimation of fog deposition in a mountain forest using a meteorological model. Journal of Geophysical Research: Atmospheres, 116, https://doi.org/10.1029/2010JD015552.

Khare, S., M. Singh, and B. K. Kaushik, 2018: Range Performance Modelling of Thermal Imaging System based on Single Parameter Characterised by Ambient Temperature and Relative Humidity. Def. Sc. Jl., 68, 480–486, https://doi.org/10.14429/dsj.68.12078.

Kirkil, G., J. Mirocha, E. Bou-Zeid, F. K. Chow, and B. Kosović, 2012: Implementation and Evaluation of Dynamic Subfilter-Scale Stress Models for Large-Eddy Simulation Using WRF*. Monthly Weather Review, 140, 266–284, https://doi.org/10.1175/MWR-D-11-00037.1.

Kutty, S. G., A. P. Dimri, and I. Gultepe, 2021a: Physical Processes Affecting Radiation Fog Based on WRF Simulations and Validation. Pure Appl. Geophys., https://doi.org/10.1007/s00024-021-02811-1.

——, ——, and ——, 2021b: Physical Processes Affecting Radiation Fog Based on WRF Simulations and Validation. Pure Appl. Geophys., https://doi.org/10.1007/s00024-021-02811-1.

Ladwig, B., 2017: wrf-python. 5 MB, https://doi.org/10.5065/D6W094P1.

Li, X., and Z. Pu, 2022: Turbulence Effects on the Formation of Cold Fog Over Complex Terrain With Large-Eddy Simulation. Geophysical Research Letters, 49, e2022GL098792, https://doi.org/10.1029/2022GL098792.

Lilly, D., 1966: On the application of the eddy viscosity concept in the Inertial sub-range of turbulence. UCAR/NCAR,.

Lim, K.-S. S., and S.-Y. Hong, 2010: Development of an Effective Double-Moment Cloud Microphysics Scheme with Prognostic Cloud Condensation Nuclei (CCN) for Weather and Climate Models. Monthly Weather Review, 138, 1587–1612, https://doi.org/10.1175/2009MWR2968.1.

Lin, C., Z. Zhang, Z. Pu, and F. Wang, 2017a: Numerical simulations of an advection fog event over Shanghai Pudong International Airport with the WRF model. J Meteorol Res, 31, 874–889, https://doi.org/10.1007/s13351-017-6187-2.

——, ——, ——, and ——, 2017b: Numerical simulations of an advection fog event over Shanghai Pudong International Airport with the WRF model. J Meteorol Res, 31, 874–889, https://doi.org/10.1007/s13351-017-6187-2.

Long, Q., B. Wu, X. Mi, S. Liu, X. Fei, and T. Ju, 2021: Review on Parameterization Schemes of Visibility in Fog and Brief Discussion of Applications Performance. Atmosphere, 12, 1666, https://doi.org/10.3390/atmos12121666.

Maalick, Z., T. Kühn, H. Korhonen, H. Kokkola, A. Laaksonen, and S. Romakkaniemi, 2016: Effect of aerosol concentration and absorbing aerosol on the radiation fog life cycle. Atmospheric Environment, 133, 26–33, https://doi.org/10.1016/j.atmosenv.2016.03.018.

Maronga, B., and F. C. Bosveld, 2017: Key parameters for the life cycle of nocturnal radiation fog: a comprehensive large-eddy simulation study. Quarterly Journal of the Royal Meteorological Society, 143, 2463–2480, https://doi.org/10.1002/qj.3100.

Mazoyer, M., C. Lac, O. Thouron, T. Bergot, V. Masson, and L. Musson-Genon, 2017: Large eddy simulation of radiation fog: impact of dynamics on the fog life cycle. Atmospheric Chemistry and Physics, 17, 13017–13035, https://doi.org/10.5194/acp-17-13017-2017.

Menut, L., S. Mailler, J.-C. Dupont, M. Haeffelin, and T. Elias, 2014: Predictability of the Meteorological Conditions Favourable to Radiative Fog Formation During the 2011 ParisFog Campaign. Boundary-Layer Meteorol, 150, 277–297, https://doi.org/10.1007/s10546-013-9875-1.

Milbrandt, J. A., and M. K. Yau, 2005a: A Multimoment Bulk Microphysics Parameterization. Part I: Analysis of the Role of the Spectral Shape Parameter. Journal of the Atmospheric Sciences, 62, 3051–3064, https://doi.org/10.1175/JAS3534.1.

——, and ——, 2005b: A Multimoment Bulk Microphysics Parameterization. Part II: A Proposed Three-Moment Closure and Scheme Description. Journal of the Atmospheric Sciences, 62, 3065–3081, https://doi.org/10.1175/JAS3535.1.

——, and ——, 2005c: A Multimoment Bulk Microphysics Parameterization. Part I: Analysis of the Role of the Spectral Shape Parameter. Journal of the Atmospheric Sciences, 62, 3051–3064, https://doi.org/10.1175/JAS3534.1.

——, and ——, 2005d: A Multimoment Bulk Microphysics Parameterization. Part II: A Proposed Three-Moment Closure and Scheme Description. Journal of the Atmospheric Sciences, 62, 3065–3081, https://doi.org/10.1175/JAS3535.1.

Mirocha, J., B. Kosović, and G. Kirkil, 2014: Resolved Turbulence Characteristics in Large-Eddy Simulations Nested within Mesoscale Simulations Using the Weather Research and Forecasting Model. Monthly Weather Review, 142, 806–831, https://doi.org/10.1175/MWR-D-13-00064.1.

Mirocha, J. D., J. K. Lundquist, and B. Kosović, 2010: Implementation of a Nonlinear Subfilter Turbulence Stress Model for Large-Eddy Simulation in the Advanced Research WRF Model. Monthly Weather Review, 138, 4212–4228, https://doi.org/10.1175/2010MWR3286.1.

MODIS Science Team, 2017a: MYD021KM MODIS/Aqua Calibrated Radiances 5-Min L1B Swath 1km. https://doi.org/10.5067/MODIS/MYD021KM.061.

——, 2017b: MOD021KM MODIS/Terra Calibrated Radiances 5-Min L1B Swath 1km. https://doi.org/10.5067/MODIS/MOD021KM.061.

Nakanishi, M., and H. Niino, 2006: An Improved Mellor–Yamada Level-3 Model: Its Numerical Stability and Application to a Regional Prediction of Advection Fog. Boundary-Layer Meteorol, 119, 397–407, https://doi.org/10.1007/s10546-005-9030-8.

——, and ——, 2009: Development of an Improved Turbulence Closure Model for the Atmospheric Boundary Layer. Journal of the Meteorological Society of Japan, 87, 895–912, https://doi.org/10.2151/jmsj.87.895.

NCEI, 2022: Daily U.S. Snowfall and Snow Depth | National Centers for Environmental Information (NCEI). https://www.ncei.noaa.gov/access/monitoring/daily-snow/ (Accessed September 29, 2022).

Olson, J., J. S. Kenyon, W. M. Angevine, J. M. Brown, M. Pagowski, and K. Sušelj, 2019: A Description of the MYNN-EDMF Scheme and the Coupling to Other Components in WRF–ARW. https://doi.org/10.25923/N9WM-BE49.

Pinto, J. O., A. A. Jensen, P. A. Jiménez, T. Hertneky, D. Muñoz-Esparza, A. Dumont, and M. Steiner, 2021: Real-time WRF large-eddy simulations to support uncrewed aircraft system (UAS) flight planning and operations during 2018 LAPSE-RATE. Earth System Science Data, 13, 697–711, https://doi.org/10.5194/essd-13-697-2021.

Pithani, P., and Coauthors, 2019: WRF Model Prediction of a Dense Fog Event Occurred During the Winter Fog Experiment (WIFEX). Pure Appl. Geophys., 176, 1827–1846, https://doi.org/10.1007/s00024-018-2053-0.

Poku, C., A. N. Ross, A. A. Hill, A. M. Blyth, and B. Shipway, 2021: Is a more physical representation of aerosol activation needed for simulations of fog? Atmospheric Chemistry and Physics, 21, 7271–7292, https://doi.org/10.5194/acp-21-7271-2021.

Price, J., 2011a: Radiation Fog. Part I: Observations of Stability and Drop Size Distributions. Boundary-Layer Meteorol, 139, 167–191, https://doi.org/10.1007/s10546-010-9580-2.

——, 2011b: Radiation Fog. Part I: Observations of Stability and Drop Size Distributions. Boundary-Layer Meteorol, 139, 167–191, https://doi.org/10.1007/s10546-010-9580-2.

——, and K. Stokkereit, 2020: The Use of Thermal Infra-Red Imagery to Elucidate the Dynamics and Processes Occurring in Fog. Atmosphere, 11, 240, https://doi.org/10.3390/atmos11030240.

Reback, J., and Coauthors, 2021: pandas-dev/pandas: Pandas 1.3.3. https://doi.org/10.5281/ZENODO.3509134.

Román-Cascón, C., G. J. Steeneveld, C. Yagüe, M. Sastre, J. A. Arrillaga, and G. Maqueda, 2016: Forecasting radiation fog at climatologically contrasting sites: evaluation of statistical methods and WRF. Quarterly Journal of the Royal Meteorological Society, 142, 1048–1063, https://doi.org/10.1002/qj.2708.

Román-Cascón, C., C. Yagüe, G.-J. Steeneveld, G. Morales, J. A. Arrillaga, M. Sastre, and G. Maqueda, 2019: Radiation and cloud-base lowering fog events: Observational analysis and evaluation of WRF and HARMONIE. Atmospheric Research, 229, 190–207, https://doi.org/10.1016/j.atmosres.2019.06.018.

Ryerson, W. R., and J. P. Hacker, 2014: The Potential for Mesoscale Visibility Predictions with a Multimodel Ensemble. Weather and Forecasting, 29, 543–562, https://doi.org/10.1175/WAF-D-13-00067.1.

Schwenkel, J., and B. Maronga, 2019: Large-eddy simulation of radiation fog with comprehensive two-moment bulk microphysics: impact of different aerosol activation and

condensation parameterizations. Atmospheric Chemistry and Physics, 19, 7165–7181, https://doi.org/10.5194/acp-19-7165-2019.

Simon, J. S., B. Zhou, J. D. Mirocha, and F. K. Chow, 2019: Explicit Filtering and Reconstruction to Reduce Grid Dependence in Convective Boundary Layer Simulations Using WRF-LES. Monthly Weather Review, 147, 1805–1821, https://doi.org/10.1175/MWR-D-18-0205.1.

Skamarock, W. C., and Coauthors, 2019a: A Description of the Advanced Research WRF Model Version 4. UCAR/NCAR,.

——, and Coauthors, 2019b: A Description of the Advanced Research WRF Model Version 4. UCAR/NCAR,.

Smith, D. K. E., I. A. Renfrew, J. D. Price, and S. R. Dorling, 2018: Numerical modelling of the evolution of the boundary layer during a radiation fog event. *Weather*, **73**, 310–316, https://doi.org/10.1002/wea.3305.

Smith, D. K. E., I. A. Renfrew, S. R. Dorling, J. D. Price, and I. A. Boutle, 2021: Sub-km scale numerical weather prediction model simulations of radiation fog. Q J R Meteorol Soc, 147, 746–763, https://doi.org/10.1002/qj.3943.

Steeneveld, G. J., R. J. Ronda, and A. A. M. Holtslag, 2015: The Challenge of Forecasting the Onset and Development of Radiation Fog Using Mesoscale Atmospheric Models. Boundary-Layer Meteorol, 154, 265–289, https://doi.org/10.1007/s10546-014-9973-8.

Steeneveld, G.-J., and M. de Bode, 2018: Unravelling the relative roles of physical processes in modelling the life cycle of a warm radiation fog. Quarterly Journal of the Royal Meteorological Society, 144, 1539–1554, https://doi.org/10.1002/qj.3300.

Stoelinga, M. T., and T. T. Warner, 1999a: Nonhydrostatic, Mesobeta-Scale Model Simulations of Cloud Ceiling and Visibility for an East Coast Winter Precipitation Event. Journal of Applied Meteorology and Climatology, 38, 385–404, https://doi.org/10.1175/1520-0450(1999)038<0385:NMSMSO>2.0.CO;2.

——, and ——, 1999b: Nonhydrostatic, Mesobeta-Scale Model Simulations of Cloud Ceiling and Visibility for an East Coast Winter Precipitation Event. Journal of Applied Meteorology and Climatology, 38, 385–404, https://doi.org/10.1175/1520-0450(1999)038<0385:NMSMSO>2.0.CO;2.

Stull, R. B., 2009: An introduction to boundary layer meteorology. Springer, 670 pp.

Taylor, P. A., Z. Chen, L. Cheng, S. Afsharian, W. Weng, G. A. Isaac, T. W. Bullock, and Y. Chen, 2021a: Surface deposition of marine fog and its treatment in the Weather Research and Forecasting (WRF) model. Atmospheric Chemistry and Physics, 21, 14687–14702, https://doi.org/10.5194/acp-21-14687-2021.

——, ——, ——, ——, ——, ——, ——, and ——, 2021b: Surface deposition of marine fog and its treatment in the Weather Research and Forecasting (WRF) model. Atmospheric Chemistry and Physics, 21, 14687–14702, https://doi.org/10.5194/acp-21-14687-2021.

Tewari, M., and Coauthors, 2004: Implementation and verification of the unified NOAH land surface model in the WRF model. 20th conference on weather analysis and forecasting/16th conference on numerical weather prediction, 11–15.

Varga, Á. J., and H. Breuer, 2020: Sensitivity of simulated temperature, precipitation, and global radiation to different WRF configurations over the Carpathian Basin for regional climate applications. Clim Dyn, 55, 2849–2866, https://doi.org/10.1007/s00382-020-05416-x.

Velde, I. R. van der, G. J. Steeneveld, B. G. J. W. Schreur, and A. a. M. Holtslag, 2010: Modeling and Forecasting the Onset and Duration of Severe Radiation Fog under Frost Conditions. Monthly Weather Review, 138, 4237–4253, https://doi.org/10.1175/2010MWR3427.1.

Wærsted, E. G., M. Haeffelin, J.-C. Dupont, J. Delanoë, and P. Dubuisson, 2017: Radiation in fog: quantification of the impact on fog liquid water based on ground-based remote sensing. Atmospheric Chemistry and Physics, 17, 10811–10835, https://doi.org/10.5194/acp-17-10811-2017.

——, ——, G.-J. Steeneveld, and J.-C. Dupont, 2019: Understanding the dissipation of continental fog by analysing the LWP budget using idealized LES and in situ observations. Quarterly Journal of the Royal Meteorological Society, 145, 784–804, https://doi.org/10.1002/qj.3465.

Wagh, S., R. Krishnamurthy, C. Wainwright, S. Wang, C. E. Dorman, H. J. S. Fernando, and I. Gultepe, 2021: Study of Stratus-Lowering Marine-Fog Events Observed During C-FOG. Boundary-Layer Meteorol, 181, 317–344, https://doi.org/10.1007/s10546-021-00670-w.

Warner, T. T., 2010: Numerical Weather and Climate Prediction. 1st ed. Cambridge University Press,.

Weston, M., S. Piketh, F. Burnet, S. Broccardo, C. Denjean, T. Bourrianne, and P. Formenti, 2022: Sensitivity analysis of an aerosol aware microphysics scheme in WRF during case studies of fog in Namibia. Atmospheric Chemistry and Physics Discussions, 1–29, https://doi.org/10.5194/acp-2022-152.

Wilks, D. S., 2011: Statistical methods in the atmospheric sciences. 3rd ed. Elsevier/Academic Press, 676 pp.

Wilson, T. H., and R. G. Fovell, 2018: Modeling the Evolution and Life Cycle of Radiative Cold Pools and Fog. Weather and Forecasting, 33, 203–220, https://doi.org/10.1175/WAF-D-17-0109.1.

Wyngaard, J. C., 2004: Toward Numerical Modeling in the "Terra Incognita." Journal of the Atmospheric Sciences, 61, 1816–1826, https://doi.org/10.1175/1520-0469(2004)061<1816:TNMITT>2.0.CO;2.

——, 2010: Turbulence in the atmosphere. Cambridge Univ. Press, 393 pp.

Yang, L., J.-W. Liu, S.-P. Xie, and S. S. P. Shen, 2021: Transition from Fog to Stratus over the Northwest Pacific Ocean: Large-Eddy Simulation. Monthly Weather Review, 149, 2913–2925, https://doi.org/10.1175/MWR-D-20-0420.1.

Yang, Y., and S. Gao, 2020: The Impact of Turbulent Diffusion Driven by Fog-Top Cooling on Sea Fog Development. Journal of Geophysical Research: Atmospheres, 125, e2019JD031562, https://doi.org/10.1029/2019JD031562.

Zhang, F., and Z. Pu, 2019: Sensitivity of Numerical Simulations of Near-Surface Atmospheric Conditions to Snow Depth and Surface Albedo during an Ice Fog Event over Heber Valley. Journal of Applied Meteorology and Climatology, 58, 797–811, https://doi.org/10.1175/JAMC-D-18-0064.1.

Zhang, X., J.-W. Bao, B. Chen, and E. D. Grell, 2018: A Three-Dimensional Scale-Adaptive Turbulent Kinetic Energy Scheme in the WRF-ARW Model. Monthly Weather Review, 146, 2023–2045, https://doi.org/10.1175/MWR-D-17-0356.1.

Zhang, X., and Coauthors, 2019: Improving Lake-Breeze Simulation with WRF Nested LES and Lake Model over a Large Shallow Lake. Journal of Applied Meteorology and Climatology, 58, 1689–1708, https://doi.org/10.1175/JAMC-D-18-0282.1.

Zhou, B., and B. S. Ferrier, 2008: Asymptotic Analysis of Equilibrium in Radiation Fog. Journal of Applied Meteorology and Climatology, 47, 1704–1722, https://doi.org/10.1175/2007JAMC1685.1.

——, and J. Du, 2010: Fog Prediction from a Multimodel Mesoscale Ensemble Prediction System. Weather and Forecasting, 25, 303–322, https://doi.org/10.1175/2009WAF2222289.1.